

# Ultra-peripheral $J/\psi$ production in PbPb collisions at $\sqrt{s_{NN}}=2.76$ TeV with CMS

By

R. Patrick Kenny III

Submitted to the Department of People who read Abstracts and the  
Graduate Faculty of the University of Kansas  
in partial fulfillment of the requirements for the degree of  
Doctor of Philosophy

Committee members

---

MEMBER 1, Chairperson

---

MEMBER 2

---

MEMBER 3

---

MEMBER 4

Date defended: October 02, 2012

The Dissertation Committee for R. Patrick Kenny III certifies  
that this is the approved version of the following dissertation :

Ultra-peripheral  $J/\psi$  production in PbPb collisions at  $\sqrt{s_{NN}}=2.76$  TeV with CMS

---

MEMBER 1, Chairperson

Date approved: October 03, 2012

# Abstract

The first is some L<sup>A</sup>T<sub>E</sub>X code, don't change it.

## **Acknowledgements**

I would like to thank all of the little people who made this thesis possible.

# Contents

<b>1</b>	<b>Introduction</b>	<b>1</b>
1.1	Overview . . . . .	1
1.2	Confirmation and characterization of the QGP from HI measurements . . . . .	3
1.3	Recent results from HI control measurements . . . . .	8
1.3.1	The HI collision . . . . .	8
<b>2</b>	<b>Theory</b>	<b>9</b>
2.1	QCD/QGP . . . . .	10
2.2	CGC/initial state . . . . .	10
2.3	Weizsäcker-Williams Approximation . . . . .	11
2.4	Vector Meson Dominance . . . . .	16
2.5	Leading Twist Approach Derivation . . . . .	21
2.6	Perturbative Quantum Chromo-dynamics . . . . .	24
2.7	Incoherent Photoproduction . . . . .	26
2.8	Photon Induced Nuclear Break-up . . . . .	26
2.9	Theoretical Results . . . . .	31
2.10	Experimental Results . . . . .	33
<b>3</b>	<b>The CMS Detector</b>	<b>38</b>
3.1	Tracker . . . . .	39
3.2	ECAL . . . . .	40

3.3	HCAL . . . . .	41
3.4	ZDC . . . . .	43
3.5	Muons . . . . .	44
3.6	Trigger . . . . .	48
<b>4</b>	<b>Analysis</b>	<b>50</b>
4.1	MC simulation . . . . .	50
4.2	Trigger development . . . . .	53
4.2.1	L1 trigger . . . . .	54
4.2.2	HLT trigger . . . . .	55
4.3	Event selection . . . . .	56
4.3.1	Data sets . . . . .	57
4.3.2	Event selection cuts . . . . .	58
4.4	Break up determination . . . . .	61
4.4.1	ZDC signal reconstruction . . . . .	61
4.4.2	Determination of the one neutron thresholds . . . . .	63
4.5	Signal extraction . . . . .	65
4.6	Efficiency determination . . . . .	70
4.6.1	Muon efficiencies . . . . .	70
4.6.2	ZDC trigger efficiency . . . . .	75
4.7	Systematic checks . . . . .	76
4.7.1	HF noise threshold . . . . .	77
4.7.2	Template fit normalization . . . . .	78
4.7.3	Mass fit . . . . .	81
4.7.4	MC acceptance . . . . .	81
4.7.5	ZDC reconstruction . . . . .	83
4.7.6	ZDC trigger efficiency . . . . .	85
4.7.7	ZDC reconstruction method comparison . . . . .	85

4.7.8	Tag and probe . . . . .	88
4.7.9	MC vs Data compairson . . . . .	90
<b>5</b>	<b>Results</b>	<b>93</b>
5.1	Coherent cross section . . . . .	93
5.2	Incoherent cross section . . . . .	95
5.3	Break up ratios . . . . .	95
5.4	diMuon-neutron correlations . . . . .	97
<b>6</b>	<b>Summary</b>	<b>105</b>
<b>7</b>	<b>Future Works</b>	<b>108</b>
7.1	Studies of 2011 PbPb data . . . . .	108
7.1.1	High mass $\gamma - \gamma \rightarrow e^+ e^-$ in PbPb 2011 . . . . .	108
7.1.2	UPC Hadronic Overlap and PbPb 2011 . . . . .	109
7.1.3	UPC with muons in HF . . . . .	111
7.2	Studies of 2013 pPb data and 2015 PbPb data . . . . .	111
7.2.1	pPb $J/\psi$ . . . . .	112
7.2.2	UPC $J/\psi$ and $\Upsilon$ in 2015 . . . . .	113
7.2.3	UPC jets . . . . .	113
<b>A</b>	<b>My Appendix, Next to my Spleen</b>	<b>121</b>

# List of Figures

1.1	Comparison of $\frac{dE_T}{d\eta}$ as a function of collision energy, $\sqrt{s_{NN}}$ , normalized by the number participating nucleons, $N_p$ , to account for the difference in the ion species collided at the various different experiments. . . . .	5
1.2	Direct photon invariant yield as a function of $p_T$ from PHENIX [1] (left) and ALICE [2] (right) . . . . .	6
1.3	$v^2$ elliptical flow measurements from SPC to the LHC. . . . .	7
1.4	Elliptical flow schematic diagram. . . . .	7
2.1	A representation of HERA deep inelastic scattering data, which shows the accumulation of low-x partons from Reference [3]. . . . .	11
2.2	The electromagnetic field boosted and at rest. . . . .	11
2.3	The zero and first order modified Bessel functions. . . . .	15
2.4	AB is the pQCD method, RSZ-LTA is the LTA method, and STARlight is the VMD model. . . . .	32
2.5	Nuclear suppression factor, $S$ , in the pQCD and LTA methods. . . . .	33
2.6	Nuclear suppression factor, $S$ , in VMD method. . . . .	34
2.7	from [4] . . . . .	34
2.8	from [4] . . . . .	34
2.9	from [4] . . . . .	35
2.10	from [5] . . . . .	35
2.11	from [5] . . . . .	36



2.12	from [6] . . . . .	36
2.13	from [7] . . . . .	36
2.14	from [7] . . . . .	37
3.1	The Compact Muon Solenoid from Reference [8]. . . . .	39
3.2	Layout of the silicon tracker with the pixels closest to the interaction point marked with a black dot and the strips segments beyond making up the remainder. . . . .	40
3.3	Material in the tracker broken down by sub-detector(left) and category (right). . . .	41
3.4	The energy resolution of ECAL as a function of energy from Reference [8]. . . . .	41
3.5	The $E_T$ resolution of HCAL as a function of $ \eta $ and $E_T$ from Reference [8]. . . . .	42
3.6	The CMS muon system showing the four DT stations in the barrel (MB1-MB4), the four CSC stations in the endcap (ME1-ME4), and the RPC stations. . . . .	45
3.7	Schematic of the DT chambers and an individual DT cell. . . . .	45
3.8	Schematic of a RPC cell. . . . .	46
3.9	Schematic of the CSC chambers and an individual CSC cell. . . . .	46
3.10	The momentum resolution of the muon system using only the tracker and the whole muon system in the barrel (left) and end cap (right). . . . .	47
3.11	The amount of material in CMS as a function of $\eta$ in number of interaction lengths. . . .	48
4.1	Generator level rapidity (left) and $p_T$ (right) distributions for the coherent (black), incoherent (red), and photon-photon process (green). . . . .	53
4.2	The $J/\psi$ polarization of the particle gun (red), coherent (blue), and incoherent sam- ples are plotted as the cosine of the helicity angle. . . . .	54
4.3	Comparison of HF noise distributions in zero bias data, physics triggered data, and MC. . . . .	60
4.4	Average ZDC pluse shape is plotted as the charge as a function of time slice for the first hadronic from $ZDC^-$ (left) and $ZDC^+$ (right). . . . .	62

4.5	The fraction of signal in time slice 5 over time slice 4 as a function of the signal in time slice 5 in $ZDC^-$ (left) and $ZDC^+$ (right).	63
4.6	Fit to the signal spectra for $ZDC^-$ (left) and $ZDC^+$ (right)	64
4.7	ZDC noise spectra from $ZDC^-$ EM section (upper left), $ZDC^+$ EM section (upper right), $ZDC^-$ HAD section (lower left), and $ZDC^+$ HAD section (lower right) from out of time time slices.	65
4.8	Mass fit to $J/\psi$ using Gaussian for the signal and a first order polynomial for the photon-photon continuum	66
4.9	Fit to MC $p_T$ templates.	67
4.10	68%, 95%, and 99% confidence contours from the $p_T$ template fit.	68
4.11	Simultaneous fit to the mass and $p_T$ spectra.	69
4.12	68%, 95%, and 99% confidence contours from the simultaneous fit.	69
4.13	Muon daughter detectability from coherent $J/\psi$	71
4.14	Dimuon acceptance from coherent $J/\psi$ (top left), incoherent $J/\psi$ (top right), and photon-photon interactions (lower).	72
4.15	Fits to tag and probe pairs in the $J/\psi$ mass region for pairs with a probe $2 <  \eta  < 2.2$ and $1.55 < p_T < 1.8$ GeV.	73
4.16	Muon trigger efficiencies in $p_T$ and $\eta$ bins from the tag and probe method.	73
4.17	The trigger efficiency from tag and probe averaged over candidates in each $(p_T,  y )$ bin.	74
4.18	The acceptance times averaged trigger efficiency from tag and probe.	75
4.19	Coherent, incoherent, and photon-photon process $p_T$ template fit to data.	79
4.20	Various mass distribution fits and the corresponding $p_T$ template fit.	80
4.21	Mass fit to $J/\psi$ using Gaussian (Left) and Crystal Ball (Right) for the signal and a polynomial for the background	81
4.22	Simultaneous fit to the mass and $p_T$ using mass templates for the mass fit.	82
4.23	Yields corrected by the MC incoherent acceptance map.	82

4.24	Yields corrected by an unpolarized $J/\psi$ sample. . . . .	83
4.25	Fit to charge spectrum from $ZDC^-$ (left) and $ZDC^+$ (right) using the standard reconstruction method . . . . .	84
4.26	Comparison of the <b>new</b> ZDC reconstruction method and the <b>standard</b> method for $ZDC^-$ (left) and $ZDC^+$ (right). . . . .	87
4.27	Effects of requiring in-time signal in successively more ZDC hadronic channels, no timing, at least <b>one</b> , at least <b>two</b> , at least <b>three</b> , and all <b>four</b> HAD channels have a maximum signal in the fourth time slice. . . . .	88
4.28	Effect of ZDC signal timing requirements after noise subtraction. . . . .	89
4.29	Tag and probe trigger efficiencies from counting (left) compared to fitting (right) .	90
4.30	Comparison of the of the dimuon rapidity distributions between coherent MC sample and Data. . . . .	91
4.31	Comparison of the of the dimuon $\phi$ distributions between coherent MC sample and Data. . . . .	91
4.32	Comparison of the of the dimuon $p_T$ distributions between coherent MC sample and Data. . . . .	92
5.1	Raw yield for the Coherent cross section measurement. . . . .	94
5.2	Corrected yields for the coherent $p_T$ region. . . . .	94
5.3	Ratio between $J/\psi$ yeilds $XnXn$ and $1n0n$ break-up modes compared the $Xn0n$ break-up mode for $J/\psi$ with $p_T$ below 150 MeV. . . . .	96
5.4	Ratio between $J/\psi$ yeilds $XnXn$ and $1n0n$ break-up modes compared the $Xn0n$ break-up mode for $J/\psi$ with $0.2 < p_T < 1.5$ GeV. . . . .	97
5.5	Transverse momentum distribution of the $J/\psi$ when $J/\psi$ and neutron have the opposite rapidity direction and the transverse momentum distribution of the $J/\psi$ when $J/\psi$ and neutron have the same rapidity direction for low- $p_T$ (top left) and high- $p_T$ (top right) $J/\psi$ . Bottom: Ratios $R_{opp/same}$ for low- $p_T$ ( left) and high- $p_T$ ( right) $J/\psi$ . . . . .	99

5.6	Ratio between the transverse momentum distribution of the $J/\psi$ when $J/\psi$ and neutron have the opposite direction and the transverse momentum distribution of the $J/\psi$ when $J/\psi$ and neutron have the same direction. . . . .	100
5.7	Rapidity distribution of the $J/\psi$ when $J/\psi$ and neutron have the opposite rapidity direction and the rapidity distribution of the $J/\psi$ when $J/\psi$ and neutron have the same rapidity direction for low- $p_T$ (top left) and high- $p_T$ (top right) $J/\psi$ . Bottom: Ratios $R_{opp/same}$ for low- $p_T$ ( left) and high- $p_T$ ( right) $J/\psi$ . . . . .	101
5.8	Rapidity ratios $R_{opp/same}$ for low- $p_T$ ( left) and high- $p_T$ ( right) $J/\psi$ . . . . .	101
5.9	Rapidity distribution of $J/\psi$ in the case of the events having the neutron in negative and positive rapidity for the low- $p_T J/\psi$ (top), high- $p_T J/\psi$ (middle) and dimuons from $\gamma\gamma$ sample (bottom). . . . .	103
5.10	$R_{(\mu\mu)^-}^{\varepsilon_{ZDC}(n^-/n^+)}$ and $R_{(\mu\mu)^+}^{\varepsilon_{ZDC}(n^-/n^+)}$ integrated over one side in rapidity for low- and high- $p_T J/\psi$ and also for dimuons from $\gamma\gamma$ sample. . . . .	104
7.1	Coherent excess in inclusive $J/\psi$ $p_T$ spectrum. . . . .	110
7.2	$v$ efficiency times acceptance in CMS from STARlight for $\sqrt{s_{NN}} = 5.1$ TeV as function of $y$ . . . . .	114
7.3	Comparison of $v$ and $J/\psi$ efficiency times acceptance in CMS from STARlight for $\sqrt{s_{NN}} = 5.1$ TeV as function of $p_T$ . . . . .	115

# List of Tables

2.1	$\sigma_{AA \rightarrow AAJ/\psi}(mb)$ the LTA, VMD, pQCD methods. Four different gluon density models are used in the pQCD method. STARlight is a simulation software package that utilizes the VMD model. . . . .	31
4.1	List of 2011 L1 seeds. . . . .	55
4.2	List of 2011 HLT trigger. . . . .	56
4.3	Integrated luminosities and number of events for the three samples used in this analysis. . . . .	58
4.4	Effects of event selection cuts. . . . .	59
4.5	ZDC trigger efficiencies for ZDC reconstruction method 1 and 2 . . . . .	76
4.6	Summary of systematic uncertainties . . . . .	77
4.7	HF noise thresholds for various noise measurement methods. . . . .	78
4.8	Candidate yields below 1.05 GeV $p_T$ for various HF noise cuts. . . . .	78
4.9	Values of the energy cuts for the HF calorimeter for RecHit and CaloTower in GeV. . . . .	78
4.10	Number of dimuon candidates with $p_T < 1.05$ when changing HF calorimeter cuts for RecHit and CaloTower. . . . .	78
4.11	ZDC trigger efficiencies for ZDC reconstruction method 1 and 2 for different trigger samples . . . . .	86
5.1	Number of coherent $J/\psi$ integrated over $p_T$ and $y$ with statistical uncertainty. . . . .	96
5.2	Number of coherent $J/\psi$ integrated over $p_T$ and $y$ with statistical uncertainty. . . . .	97

5.3	Number of $J/\psi$ integrated over $p_T$ and $y$ with statistical uncertainty. . . . .	98
5.4	Number of dimuon pairs for different directions of the neutron rapidity direction together with $R_{(\mu\mu)^-}^{n^-/n^+}$ and $R_{(\mu\mu)^+}^{n^-/n^+}$ . . . . .	102
5.5	Ratios $R_{(\mu\mu)^-}^{\varepsilon_{ZDC}(n^-/n^+)}$ and $R_{(\mu\mu)^+}^{\varepsilon_{ZDC}(n^-/n^+)}$ i.e. $R_{(\mu\mu)^-}^{n^-/n^+}$ and $R_{(\mu\mu)^+}^{n^-/n^+}$ corrected by the $ZDC^+$ and $ZDC^-$ efficiencies. . . . .	102

# Chapter 1

## Introduction

### 1.1 Overview

Microseconds after the Big Bang, the Universe existed in a state known as the Quark Gluon Plasma (QGP). In the QGP, quarks and gluons are not in hadronic bondage, forced to the confines of bound states such as protons and neutrons. The Large Hadron Collider (LHC) produces QGP in the lab in lead-lead (PbPb) collisions. The high energies and rates of the collisions at the LHC make it possible to do detailed studies of the QGP. The LHC is producing rare experimental probes such as suppressed jets and heavy quarkonia at an unprecedented rate in heavy ion collisions. As a result of recent LHC studies, physicists now have better constraints on the properties like temperature, viscosity, and energy density of the QGP.

The detailed studies of PbPb collisions coming out of the LHC experiments require an understanding of the initial state of the ions before they collide. Without more knowledge of the initial state, physicists cannot determine which experimental effects are due to the QGP and which effects are inherent to the nuclei themselves. For example, suppression of heavy quarkonia is a signature of the QGP but also appears to occur in deuterium-gold collisions where the QGP is not expected to arise [9]. Another important example is measurement of the viscosity, which depends on the relationship between the observed azimuthal anisotropy and the initial eccentricity of the

overlap of the two colliding nuclei. A clean probe of the initial state is needed by physicists to comprehensively understand the QGP. Ultra-Peripheral Collisions (UPC) at the LHC provide such a probe.

The current understanding of heavy ion collisions evolved over the last 30 years. Relativistic heavy ion collisions were first studied using the Alternating Gradient Synchrotron (AGS) at Brookhaven National Lab (BNL) in Upton, NY, followed by the Super Proton Synchrotron (SPS) at CERN near Geneva, Switzerland. From the numerous AGS and SPS experiments two main observables emerged, namely,  $J/\psi$  suppression and strangeness enhancement [?]. These results pioneered the search for the QGP.

The AGS and SPS experiments were fixed target experiments. At AGS the ion isotopes  $^{16}\text{O}$ ,  $^{28}\text{Si}$ , and  $^{197}\text{Au}$  beams were collided with fix targets. At SPS the same fix target configuration was used, but the ion isotopes were  $^{16}\text{O}$ ,  $^{32}\text{S}$ , and  $^{208}\text{Pb}$ . The center of mass energies per nucleon pair for these experiments ranged from just below 5 GeV to 20 GeV. The threshold for creating the QGP requires an energy density of  $0.15 \sim \text{GeV}/\text{fm}^3$  and a temperature near 170 MeV [?]. AGS and SPS just barely reached this threshold. Though the strangeness enhancement and  $J/\psi$  suppression signals indicated that there was likely a deconfined state of quarks and gluons created, at the energies of the AGS and SPS this state perished to quickly to study any of its properties.

Plans for a colliding beam machine dedicated to heavy ions was first proposed 1983. The proposed machine was designed to reach energies of 200 GeV per nucleon. At these energies, the QGP would persist long enough, and a that signs of a gas of hot quarks and gluons would emerge. In the summer of 2000 RHIC began collisions and the four experiments, STAR, PHENIX, BRAHMS, and PHOBOS started taking data. With collision energies of 200 GeV per colliding nucleon, the energies at RHIC were a factor of 10 higher than was previously achieved. RHIC experiments confirmed for the first time the presence of a thermalized state of quarks and gluons. Contrary to expectations, the state found at RHIC was found to be strongly coupled fluid with nearly no viscosity [].

The LHC heavy ion program began collisions in 2010, colliding PbPb at a center of mass



energy of 2.76 TeV per nucleon pair. This corresponds to an increase in the colliding energy by an order of magnitude with respect to RHIC. The LHC experiments, ALICE, ATLAS, and CMS have studying the heavy ion collisions since then. In 2013 LHCb joined the LHC heavy ion program. Thanks to the LHC and RHIC physics programs, a new era of precision heavy ion measurements is underway.

The latest results from the LHC have come from the 2013 proton-lead (pPb) run. This period of data taking was originally designed to be a control measurement. For example, the initial suppression signals observed in dAu collisions at RHIC were believed to be due to non-QGP effects [?]. The azimuthal anisotropy of particles present in PbPb and AuAu at the LHC and RHIC respectively were believed to be signals of flow from the QGP and would not appear in the lower density pp and pPb collisions. However, CMS showed evidence of a flow signal in high multiplicity pp events in early 2011 [?]. More recently ALICE has shown a structure in two particle correlation measurements, referred to as the double ridge [?], and CMS and ALICE have both shown an elliptical flow signal present in the pPb data [?].

The latest data from the pPb and dAu measurements confirm the need to understand the nature of the initial state. UPC events fulfill this need by probing the nucleus through photon interactions. By measuring UPC  $J/\psi$  events, theoretical models of the initial state can be constrained. In this thesis, the CMS capability for measuring this process, the description of the analysis, and the comparison between the measured coherent  $J/\psi$  cross section to theoretical models are given.

## **1.2 Confirmation and characterization of the QGP from HI measurements**

Creation of the QGP can be confirmed by comparing the measured energy densities with predicted critical temperature and energy densities from lattice QCD measurements. The critical energy density,  $\epsilon_{crit}$ , and critical temperature,  $T_{crit}$ , are calculated to be 1.5 GeV and 170 MeV from lattice QCD estimates [?]. The measurement of the  $\frac{dE_T}{d\eta}$  provides a means of estimating the energy

density of the hot state created in heavy ion collisions. The temperature can be estimated from the transverse momentum,  $p_T$ , spectrum of the direct photons, photons that come directly from the QGP. At both RHIC and the LHC the energy density and temperature were found to be well above the critical values. The measurements from CMS and ALICE at the LHC and STAR and PHENIX at RHIC confirm that the critical values for energy density and temperature are exceeded.

The value of  $\frac{dE}{d\eta}$  measured by CMS [10] and PHENIX [11] was done using the experiments' calorimeter systems. The value of  $E_T$  for this measurement is defined as  $E_T = \sum_i E_i \sin \theta_i$ , where  $E_i$  is the energy measured by the  $i$ th calorimeter element and  $\theta$  is the angle between the center of the detector element and the interaction point. The calculated  $\frac{dE_T}{d\eta} \neq 0$ , the interval  $0.35 < |\eta|$  was used by both experiments and corresponds to the full coverage of the PHENIX calorimeters. From the  $\frac{dE_T}{d\eta} \neq 0$  measurements, the energy density of the created medium at the LHC and RHIC were estimated from the Bjorken energy density formula,  $\epsilon_{Bj} = \frac{1}{A\tau} \frac{dE_T}{dy}$ , where  $A$  is the region of overlap between the two colliding nuclei and  $\tau$  is the formation time of the medium [12]. The energy density,  $\epsilon_{Bj}\tau$ , from PHENIX was measured at RHIC to be  $5.4 \pm 0.6 \text{ GeV fm}^{-2} \text{c}^{-1}$  for the 5% most energetic collisions compared to the  $14 \text{ GeV fm}^{-2} \text{c}^{-1}$  at the LHC as measured by CMS. Both values are well above  $\sim 1.5 \text{ GeV fm}^3$  critical energy density calculated from lattice QCD when assuming a medium formation time  $\tau = 1 \text{ fm/c}$ .

Direct photons, thermal photon created in the QGP, have been measured at RHIC by PHENIX [1] and at the LHC by ALICE [2] through the measurements of electron-positron pairs. Each experiment measured the inclusive  $p_T$  spectrum from electron-positron pairs, all pairs from the sample are taken without regard to the creation mechanism. The PHENIX measurement was taken from pp collisions and top 20% most energetic AuAu collisions, collisions with a centrality of 0-20%. The ALICE measurement analyzed the 0-40% centrality, 40%-80% centrality PbPb collisions, and pp collisions. In both measurements, the contribution to the inclusive spectrum was sorted into a direct component and a component from background, primary decays from hadrons such as pions and eta. In the PHENIX measurement this was done by performing a fit to the mass distribution of the electron-positron pair for each  $p_T$ . For the ALICE measurement, the double ratio between

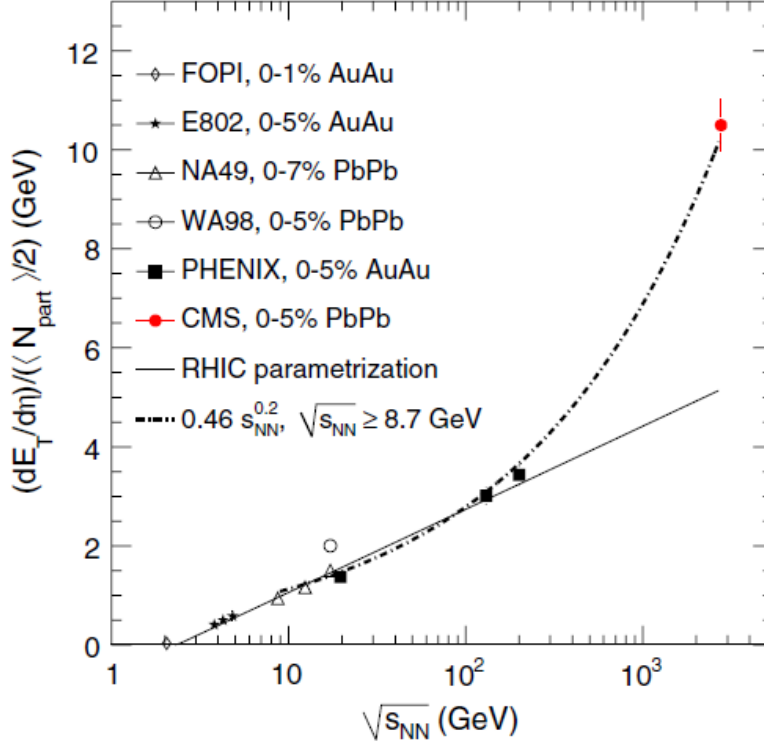


Figure 1.1: Comparison of  $\frac{dE_T}{d\eta}$  as a function of collision energy,  $\sqrt{s_{NN}}$ , normalized by the number participating nucleons,  $N_p$ , to account for the difference in the ion species collided at the various different experiments.

the inclusive photons to pions over the ratio between photons from hadron decays and pions was measured to estimate the direct contribution. The inclusive photon  $p_T$  were then rescaled by the direct photon fractions to produce a direct photon spectrum. The slope of an exponential fit to the low  $p_T$  portion the direct photon spectrum is used to measure the temperature.

The direct photon through measurement of the temperature offers a clear way of establishing whether the critical temperature for deconfinement was achieved. The direct photon  $p_T$  spectra in Fig. 1.2 show a clear enhancement at low  $p_T$  compared to the rescaling to the pp spectra that fits the high  $p_T$  part of the spectrum, indicating a clear deviation for pp collisions. The low  $p_T$  photons therefore primarily come directly from the thermal activity of the QGP. The thermal spectrum of the QGP is therefor imprinted on this part of the spectrum. The exponential fits to the spectra provide this temperature. The temperature from PHENIX was measured to be  $221 \pm 21$  MeV and  $304 \pm 51$  MeV from ALICE, both well above the critical temperture estimated from lattice QCD

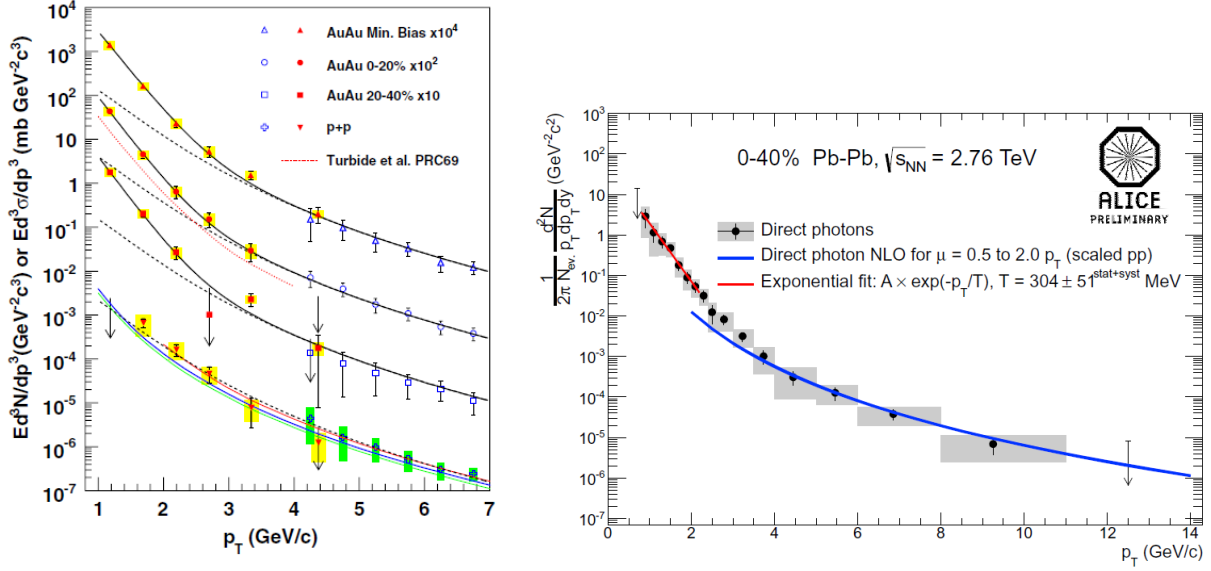


Figure 1.2: Direct photon invariant yield as a function of  $p_T$  from PHENIX [1] (left) and ALICE [2] (right)

of  $\sim 170$  MeV.

The combination of the energy density and temperature measurements are RHIC create a consistent picture, both RHIC and the LHC have created a deconfined state, and due the higher collision energies at the LHC the the medium gets hotter.

Prior to the RHIC, the QGP was thought to be a gas of quarks and gluons. At RHIC the measurements at STAR showed that the medium appeared to obey hydrodynamic equations and flows like a fluid. This same signal was also measured by CMS at the LHC.

This is how you measure elliptic flow is measured.

These are the results.

The signal indicates that there is very little viscosity. However, this depends on the eccentricity of initial overlap region, which depends on the description of the initial state of the colliding nuclei.

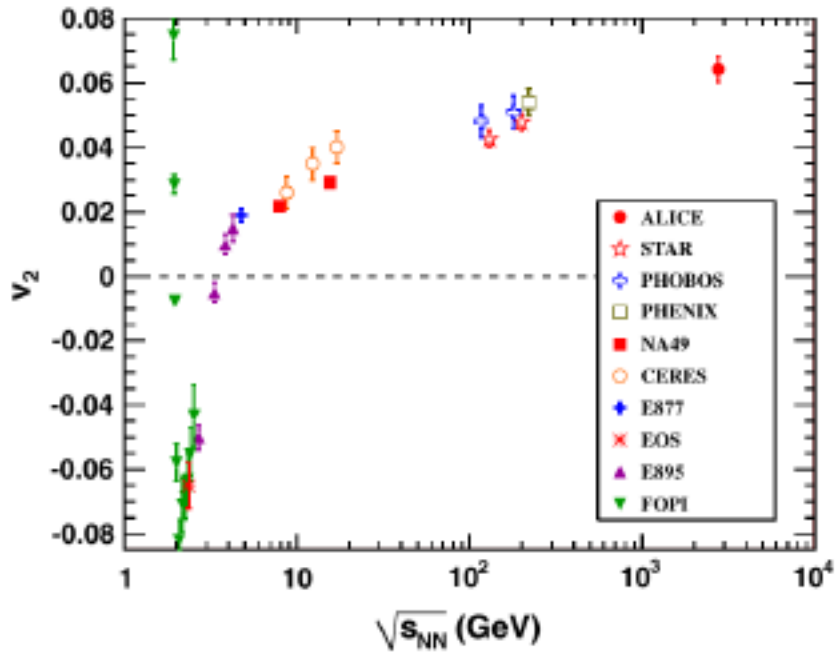


Figure 1.3:  $v^2$  elliptical flow measurements from SPC to the LHC.

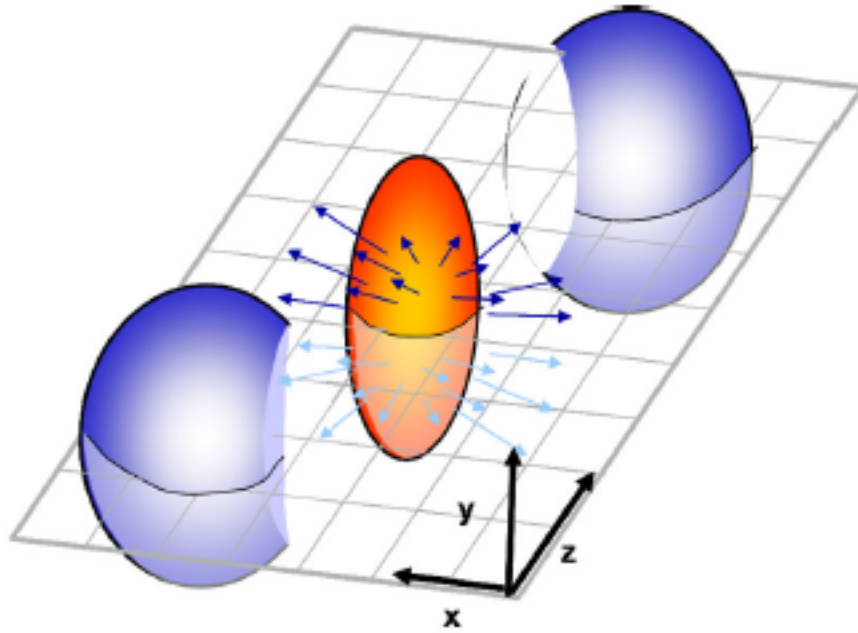


Figure 1.4: Elliptical flow schematic diagram.

## **1.3 Recent results from HI control measurements**

### **1.3.1 The HI collision**

The AGS and SPS created the first signs of a deconfined state, but the nature of the state was uncertain. At RHIC the existence of the QGP was confirmed and its nature found to be hydrodynamic. The LHC and RHIC experiments are now looking deeper in the characteristics of QGP. More precise and sophisticated measurement techniques now require a better understanding of the ions before they collide in order to produce the proper theoretical modeling.

Over the course of the experimental evolution the following picture of a heavy ion collision emerged. First, highly contracted ions travel toward each other. Second, QGP forms and reaches thermal equilibrium. Third, this hot dense state expands hydrodynamically. Fifth, Fifth as the collection of quarks and gluons cool, a gas of hot hadrons forms and expands. Finally, all interactions freeze out and the produced particles stream to the detector.

# Chapter 2

## Theory

The colliding nuclei interact electromagnetically in an UPC event, avoiding the complicated mixing of final state and initial state effects found in nuclear collisions. In UPC events, no QGP state emerges, and the effects arising from the QGP no longer obscure the initial state effects. Other initial state probes such as peripheral nuclear collisions and proton-nucleus collisions have the potential to create the QGP obscuring which effects come from the initial state. It is impossible to create the QGP in UPC events because the nucleons within the nucleus do not collide. UPC events provide clarity by enhancing physicists' understanding of the initial state.

The interactions between the field of photons surrounding the colliding nuclei and the gluons of nuclei can produce a  $J/\psi$  probing the gluon density. The UPC  $J/\psi$  photoproduction cross section is therefore a probe of the initial state of the nucleus. The Weizsäcker-Williams approximation provides a way to calculate the density of probing photons that surrounds the nucleus. The electron-proton scattering data gives a value for the proton photoproduction cross section at lower energies. The perturbative Quantum Chromo-dynamics (pQCD), Vector Meson Dominance (VMD), and Leading Twist (LTA) methods all combined the nuclear photon flux with the proton scattering data to calculate the nuclear photoproduction cross section. Each of these methods handle the gluon density of the nucleus differently producing a measurable difference in the value of the  $J/\psi$  photoproduction cross section.

## 2.1 QCD/QGP

## 2.2 CGC/initial state

The color glass condensate (CGC) is an effective theory of parton saturation and coupling that aims to explain the initial state of hadronic matter in high energy heavy ions collisions [13]. CGC was developed to calculate the distribution of partons within a nucleus. The theory's name is instructive of how this is achieved [3]. The first term color stems simply from the fact that the partons carry a color charge. The second term refers to a coupling within the theory of the low momentum partons to the high momentum partons. In CGC the low momentum partons take on the time scales of the higher momentum partons, which can be described perturbatively. This behavior is analogous to glass, which behaves like a solid on short time scales and a liquid on long time scales. The last term condensate refers to saturation. The CGC predicts that as the hadronic matter is boosted to higher and higher energies, low momentum states are filled and become increasingly less favorable to higher momentum states. In the theory the higher momentum states are treated as the source of the lower momentum states in the same manner that an electron is the source of an electric and magnetic field. This couples the low momentum partons to the weakly coupled high momentum partons.

The CGC was inspired by and gives a natural explanation of deep inelastic scattering data. Figure 2.1 gives a representation of the data collected by the HERA experiment. The HERA data shows that as the constituents of a heavy ion are explored the number of constituents at lower momentum grows. Following from right to left in Figure 2.1 the gluon density increases as  $x$  decreases, where  $x$  is the fraction of the total momentum the constituent holds. The number of low momentum constituents can not however grow without bound, a plateau must emerge. A plateau is required in order to assure unitarity, which requires that the probability of scattering off the nucleus does not exceed one. Emergence of a plateau would indicate evidence of saturation, the point where it becomes less favorable to produce more low momentum constituents. As seen in Figure 2.1, the saturation scale increases as the momentum transferred to the probe  $Q^2$  increases.



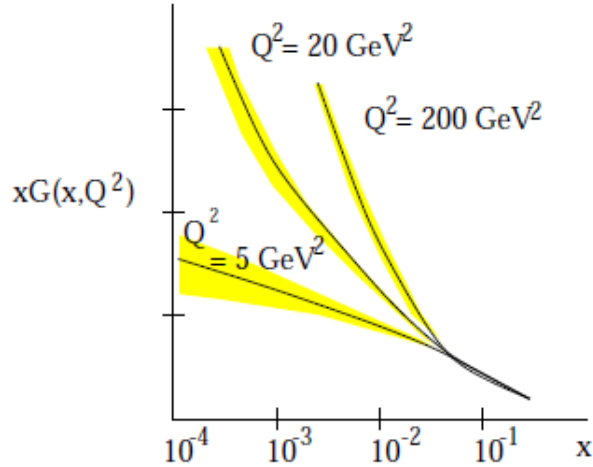


Figure 2.1: A representation of HERA deep inelastic scattering data, which shows the accumulation of low- $x$  partons from Reference [3].

This effect suggests that the saturation scale can be used to measure the running of the strong coupling constant predicted by standard perturbative QCD.

## 2.3 Weizsäcker-Williams Approximation

The Weizsäcker-Williams approximation relates the electric field of a stationary point charge to the photon field that arises at ultra relativistic velocities. The approximation is semi-classical and combines both classical and quantum elements. A Fourier transform of Maxwell's equations combine with Einstein's equation for the energy of a photon in the Weizsäcker-Williams approximation.

The frequency modes

of the electrostatic field

are treated as pho-

tons. The conver-

sion of the electric

field to a flux of pho-

tons simplifies the cal-

culation of interaction

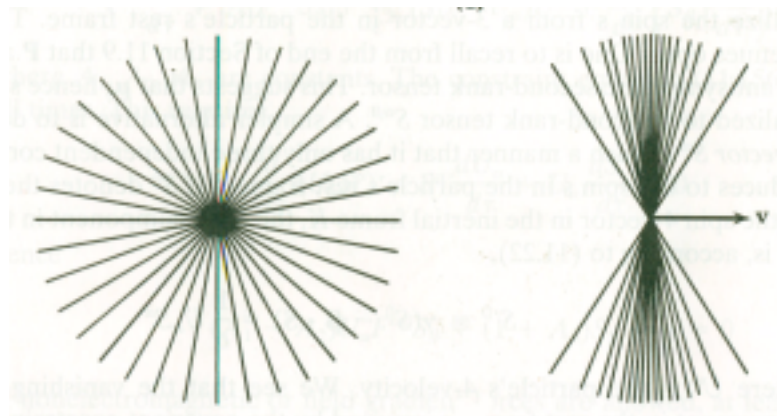


Figure 2.2: The electromagnetic field boosted and at rest.

cross sections. The

Weizsäcker-Williams ap-

proximation makes the

calculation of electromagnetic interactions with the nucleus tractable.

The Wiezacker-Williams approximation begins with the equation for the electric field of the projectile nucleus at rest. The electromagnetic field only needs to be considered at the position of the target nucleus. From the projectile's point of view, the target is moving and contributes  $-vt$  to Eq. 2.1, the equation for the electric field of the projectile nucleus at rest.

$$x' = -vt' \quad y' = b \quad z' = 0 \quad \vec{E}' = \left( \frac{eZ}{4\pi\epsilon_0 \left( (-vt')^2 + b^2 \right)^{3/2}} \right) \left( -vt' \hat{\mathbf{x}}' + b \hat{\mathbf{y}}' \right) \quad (2.1)$$

In Eq. 2.1,  $b$  is the impact parameter, the distance of separation at closest approach,  $v$  is the velocity of the projectile nucleus,  $Z$  is the number of protons in the nucleus, and  $e$  is the charge of the electron. Two simplifications occur due to the coordinates of Eq. 2.1. The magnetic field is equal to zero, because the projectile is at rest, and the  $z$  coordinate can be ignored, reducing the equation to two dimensions.

The Lorentz transformation converts the field equations in the projectile's frame to equations in the target's frame. The result is a set of equations that relate the electric and magnetic field components in one frame to the components of the electric and magnetic field in another frame moving at a different constant velocity. Eq. 2.2 gives the result of the transformation from the projectile's primed frame to the target's rest frame for the field components [14]:

$$\begin{aligned} E'_x &= E_x & \gamma(E'_y/c + \beta B'_z) &= E_y/c & \gamma(E'_z/c + \beta B'_y) &= E_z/c \\ B'_x &= B_x & \gamma(B'_y - \beta E'_z/c) &= B_y & \gamma(B'_z + \beta E'_y/c) &= B_z \end{aligned} \quad (2.2)$$

The transformation equations for the fields, Eq. 2.2, and the transformation of the coordinates

reduce to Eq. 2.3 [14]:

$$\begin{aligned} E'_x &= E_x & \gamma E'_y &= E_y & \gamma \beta E'_y / c &= B_z \\ ct' &= \gamma ct & x' &= -\gamma \beta ct \end{aligned} \quad (2.3)$$

The simplicity of Eq. 2.1 creates the simplicity of Eq. 2.2. The Lorentz transformation reduces the six components of the electromagnetic field in the target's frame to the three equations in Eq. 2.2 by relating them to the fields of the projectile's frame.

The combination of Eq. 2.1 and Eq. 2.2 produce equations for the electric and magnetic fields in the target's rest frame. Eq. 2.1 gives the expression for the field components as seen in the projectile frame.

$$\begin{aligned} \vec{E} &= \left( \frac{\gamma e Z}{4\pi\epsilon_0 \left( (\gamma vt)^2 + b^2 \right)^{3/2}} \right) (vt\hat{\mathbf{x}} + b\hat{\mathbf{y}}) \\ \vec{B} &= \frac{\gamma \beta e Z b}{4\pi c \epsilon_0 \left( (\gamma vt)^2 + b^2 \right)^{3/2}} \hat{\mathbf{z}} = \frac{\gamma \mu_0 v e Z b}{4\pi \left( (\gamma vt)^2 + b^2 \right)^{3/2}} \hat{\mathbf{z}} \end{aligned} \quad (2.4)$$

If the impact parameter  $b$  goes to zero, the target sits in the line of the projectile particle's motion, and the denominator carries a factor of  $\gamma$  squared. If  $vt$  goes to zero, the projectile particle is directly above or below in the  $y$  direction, and the numerator carries a factor of  $\gamma$ . This results in fields that are a factor of  $\gamma^3$  higher in the  $y$  direction than in the  $x$  direction (see Fig. 2.2). The boost compresses the electric field of the charge in the direction of the boost and produces a magnetic field resulting in a form similar to radiation. The point charge at ultra relativistic velocities produces a strong electric field in the plane transverse to its motion resembling a plane wave.

Separating the even and odd functions of the electromagnetic field simplify the decomposition of the field equations into Fourier modes. The even functions decompose into cosine functions, odd functions into sine functions. The  $y$ -component of the electric field and the  $z$ -component of

the magnetic field are even functions in time, and the x-component of the electric field is an odd function in time. Eq. 2.5 gives the Fourier transformation integrals.

$$E_x(\omega) = \sqrt{\frac{2}{\pi}} \frac{eZ}{4\pi\epsilon_0 b^2} \int_0^\infty \frac{(\gamma vt/b) \sin(\omega t)}{\left((\gamma vt/b)^2 + 1\right)^{3/2}} dt \quad E_y(\omega) = \sqrt{\frac{2}{\pi}} \frac{\gamma eZ}{4\pi\epsilon_0 b^2} \int_0^\infty \frac{\cos(\omega t)}{\left((\gamma vt/b)^2 + 1\right)^{3/2}} dt$$

$$B_z(\omega) = \frac{\beta E_y(\omega)}{c} \quad (2.5)$$

With the appropriate substitutions, tables provide solutions to the integrals of Eq. 2.5 as seen in Ref. [15].

$$u = \frac{\gamma vt}{b} \quad du \left( \frac{b}{\gamma v} \right) = dt \quad \omega' = \frac{\omega b}{\gamma v}$$

$$\int_0^\infty \frac{u \sin(\omega' u)}{(u^2 + 1)^{3/2}} du = \omega' K_0(\omega') \quad \int_0^\infty \frac{\cos(\omega' u)}{(u^2 + 1)^{3/2}} du = \omega' K_1(\omega') \quad (2.6)$$

The Fourier transformation replaces the time variable with a frequency variable in the field equations. The frequency relates to photon energy by the Einstein's photon energy equation,  $E = \hbar\omega$ . The substitution of time with frequency allows for a flux of photons to replace the classical electromagnetic field.

The  $\gamma$  dependence of the field components is different because of the different  $t$  dependence of Eq. 2.6. The integrals in Eq. 2.6 shift the  $\gamma$  dependence of the field component equations. Eq. 2.7 gives the result of the integrals:

$$E_x(\omega) = \sqrt{\frac{2}{\pi}} \frac{eZ}{4\pi\epsilon_0 b^2} \frac{b}{\gamma v} \frac{\omega b}{\gamma v} K_0\left(\frac{\omega b}{\gamma v}\right) \quad E_y(\omega) = \sqrt{\frac{2}{\pi}} \frac{\gamma eZ}{4\pi\epsilon_0 b^2} \frac{b}{\gamma v} \frac{\omega b}{\gamma v} K_1\left(\frac{\omega b}{\gamma v}\right) \quad (2.7)$$

$\gamma$  is subsumed into the substitution from  $t$  to  $\omega$  in the numerator of the x-component and becomes a part of the zeroth-order modified Bessel function upon integration. The y-component does not have a factor of  $t$  in the numerator, therefore the factor of  $\gamma$  remains outside of the integral, and it does not get subsumed into the first-order modified Bessel function.

In Eq. 2.7,  $E_y$  carries an additional factor of  $\gamma$  in the numerator relative to the  $E_x$ .  $E_y$  is  $\gamma$  times larger than  $E_x$ .

In the ultra-relativistic limit, the electric and magnetic fields have the same configuration as electromagnetic plane wave radiation.

The electric and magnetic fields are perpendicular and related by a factor of  $c$  in the ultra relativistic limit. When  $v$  approaches  $c$ ,  $\beta \approx 1$ , the

y-component of the electric field and the z-component of the magnetic field are related by a factor of  $c$ ,  $E_y/c = B_z$ . Because  $K_0(x)$  is smaller than  $K_1(x)$  for all  $x$ , when  $\gamma \gg 1$ ,  $E_y$  is approximately equally to  $\gamma E_x$ . The conditions imposed by the ultra-relativistic limit result in the relationship of Eq. 2.8.

$$\gamma \gg 1 \rightarrow \gamma E_x \gg E_x \rightarrow E_y \gg E_x \quad (2.8)$$

The x-component of the electric field can therefore be ignored and the magnetic and electric fields are left perpendicular to each other. The six field components reduced to one electric component and one perpendicular magnetic field component, which have a configuration identical to a plane wave.

As with plane waves, the energy per area per time transfered by the electromagnetic field is given by the Poynting vector. The Poynting vector takes the simple form of a plane pulse propagating in the x direction.

$$\vec{S} \equiv \vec{E} \times \vec{B} / \mu_0 = (E_y^2 / c \mu_0) \hat{x} = c \epsilon_0 E_y^2 \hat{x} \quad (2.9)$$

The Poynting vector relates to the fluence (energy per unit area) [16],

$$I(b) = \hat{x} \cdot \int_0^\infty \vec{S} d\omega = \int_0^\infty (c \epsilon_0 E_y^2) d\omega = \int_0^\infty \left( \frac{dI}{d\omega} \right) d\omega \quad (2.10)$$

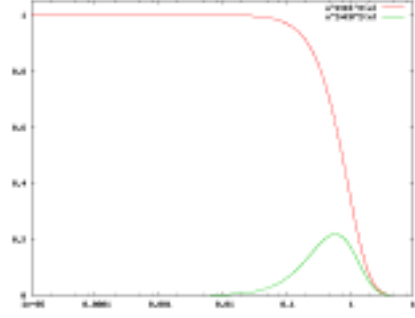


Figure 2.3: The zero and first order modified Bessel functions.

and the spectral fluence (energy per area per frequency).

$$\frac{dI}{d\omega} = c\epsilon_0 E_y^2 = \frac{e^2 Z^2 c}{4\pi^3 b^2 v^2 \epsilon_0} \left(\frac{\omega b}{\gamma v}\right)^2 K_1^2\left(\frac{\omega b}{\gamma v}\right) = \alpha \hbar \left(\frac{Z}{b\beta\pi}\right)^2 \left(\frac{\omega b}{\gamma v}\right)^2 K_1^2\left(\frac{\omega b}{\gamma v}\right) \quad (2.11)$$

Substituting Eq. 2.7 into Eq. 2.10 gives the Poynting vector as a function of frequency. Eq. 2.11 paves the way for Einstein's equation. The spectral fluence given by Eq. 2.11 relates the frequency to energy, which are the same quantities present in Einstein's equation.

Einstein's equation,  $E = \hbar\omega$ , gives the energy of a photon, which is related to the spectral fluence. If the fluence is due to a photon number density,  $N$ , Einstein's equation relates  $N$  to the fluence. The relationship between the number of photons per unit area in an infinitesimal energy range and the spectral fluence in an infinitesimal frequency range is given by Eq. 2.12 [14].

$$\frac{dI}{d\omega} d\omega = \hbar\omega N(\omega) d(\hbar\omega) \rightarrow \frac{1}{\hbar^2 \omega} \frac{dI}{d\omega} = N(\omega) \quad (2.12)$$

Plugging Eq. 2.11 into Eq. 2.12 yields the semiclassical photon flux of an ultra-relativistic nucleus.

$$N(\omega, b) = \frac{\alpha}{\hbar\omega} \left(\frac{Z}{b\beta\pi}\right)^2 \left(\frac{\omega b}{\gamma v}\right)^2 K_1^2\left(\frac{\omega b}{\gamma v}\right) \quad (2.13)$$

Eq. 2.13 replaces the classical electric field of a point charge with a semiclassical field of photons. Physicists can calculate the electromagnetic interactions between nuclei with the final result of the Weizsäcker-Williams approximation, Eq. 2.13. The photon flux in Eq. 2.13 provides the electromagnetic input to the  $J/\psi$  photoproduction cross section calculation.

## 2.4 Vector Meson Dominance

The Vector Meson Dominance method for calculating the  $J/\psi$  photoproduction cross section has three main components. VMD approach is constructed from the Weizsäcker-Williams photon flux, the VMD fit to the proton-electron data, and the Glauber model for calculating the nuclear cross

sections from the proton-electron cross sections. The Weizsäcker-Williams photon flux provides the probe. The proton-electron scattering data combine with the Glauber model create a picture of the initial state of the nucleus. Each of the different approaches to calculating the UPC  $J/\psi$  photoproduction cross section use these same elements. However, the different models each use the last two elements differently to produce different pictures of the nucleus and different cross sections values.

The photon flux in the photoproduction cross section calculation must be finite in order for the cross section to be meaningful. The Weizsäcker-Williams approximation, Eq. 2.13, produces a divergence at  $b = 0$ . The probability of the nuclei interacting would exceed one if the photon flux were infinite. The divergence that arises at  $b = 0$  from  $K_1$  results in an unphysically infinite photon flux. Removing the divergence is necessary. Special treatment of impact parameter,  $b$ , where the colliding nuclei overlap eliminates the divergence.

A modulation of the photon flux can subdue the divergence at  $b = 0$ . A convolution of the photon flux with the nucleon number density functions of the colliding nuclei produces the necessary modulation. Eq. 2.14 gives the nucleon density of a single nucleus,

$$\rho_A(s) = \frac{\rho_0}{1 + \exp[(s - R_{WS})/d]} \quad (2.14)$$

In Eq. 2.14,  $s$  is the distance from the center of the nucleus,  $R_{WS}$  is the radius of the nucleus, and  $d$  is the skin depth, which determines how quickly the nucleon density falls off beyond the nuclear radius. In Eq. 2.15 the depth of the nucleus is integrated out leaving just the transverse dimension in  $T_A$ . The average number of nucleons in the overlap region is given by a convolution of  $T_A$  from each of the two nuclei to produce  $T_{AA}$ .

$$\begin{aligned} T_A(\vec{r}) &= \int dz \rho_A(\sqrt{|\vec{r}|^2 + z^2}) \\ T_{AA}(|\vec{b}|) &= \int d^2\vec{r} T_A(\vec{r}) T_A(\vec{r} - \vec{b}) \end{aligned} \quad (2.15)$$

$T_{AA}$  is the function that modulates the photon flux. As input to the Poisson distribution,  $T_{AA}$  reduces

Eq. 2.13 at values of  $b$  where the nuclei overlap significantly and eliminates the divergence in the photon flux.

Modulating the photon flux by the probability that no nucleon-nucleon collisions occur limits the photon flux at low  $b$  in Eq. 2.13. The convolution of the photon flux with the  $b$  dependent probability that no nucleon-nucleon collisions occur removes the divergence in Eq. 2.13. Using the mean number of nucleons in the overlap region given by  $T_{AA}$ , the Poisson distribution gives the probability that no collisions occur at a given  $b$ :

$$P_0(b) = \exp[-T_{AA}(b)\sigma_{NN}] \quad (2.16)$$

In Eq. 2.16,  $\sigma_{NN}$  is the cross section for a nucleon-nucleon interaction, which gives the probability that a collision will occur given the average number of nucleons in the overlap region. The average photon flux over impact parameter,  $b$ , can be calculated from the integration of the  $b$ -dependent photon flux, Eq. 2.13, with the  $b$ -dependent probability of having no nucleon-nucleon interactions, Eq. 2.16.

$$\frac{dN_\gamma(k)}{dk} = \int_0^\infty 2\pi b db P_0(b) \int_0^R \frac{r dr}{\pi R_A^2} \int_0^{2\pi} d\phi \frac{d^3 N_\gamma(k, b + r \cos(\phi))}{dk d^2 r} \quad (2.17)$$

Eq. 2.17 goes down to  $b = 0$  where the photon flux is infinite, but because the probability of having a nucleon-nucleon collisions is high, the divergence is eliminated. The result of Eq. 2.17 does not diverge.

A power-law fit to the proton photoproduction data gives an analytic expression for the energy dependence of the proton photoproduction cross section. The fitting function is simple and only depends on the photon-proton center of mass energy,  $W$ . Eq. 2.18 gives the parameterization of the forward proton photoproduction cross section fit.

$$\left. \frac{d\sigma(\gamma p \rightarrow V p)}{dt} \right|_{t=0} = b_v(XW^\epsilon + YW^{-\eta}) \quad (2.18)$$

$W$  is the center of mass energy of the proton-photon system in Eq. 2.18. The remaining variables



in Eq. 2.18 are simple power-law fit parameters. The  $XW^\epsilon$  term characterizes pomeron mediated interactions, and the  $YW^\eta$  term characterizes meson mediated interactions[17].  $J/\psi$ 's high mass relative to the  $\pi$  and  $\rho$  renders the second term in Eq. 2.18 negligible as the term falls rapidly with increasing  $W$ . Eq. 2.18 allows for extrapolation and interpolation of the measured forward proton photoproduction cross section. The fit to the data provides estimates for energies that have not yet been probed experimentally.

The proton-electron scattering data is used differently in the VMD method than in the other major methods. The VMD method for calculating UPC photoproduction cross sections relies more on electron-proton scattering data. The proton photoproduction cross sections from the electron-proton scattering data is a direct input to the VMD model. A power-law fit to the proton photoproduction data, as opposed to model dependent gluon densities of other approaches, combines with the Glauber model to provide the nuclear model in the VMD method. Because of the simplicity of the method, the VMD approach incorporates less modifications of the nuclear initial state relative to the proton initial state. As a result, the VMD method produces a higher UPC  $J/\psi$  photoproduction cross section relative to the other methods.

Vector meson dominance and the optical theorem allow for the calculation of the total proton-meson scattering cross section from the fit given by Eq. 2.18. The optical theorem relates a total cross section,  $\sigma$ , to a corresponding forward scattering cross section,  $d\sigma/dt|_{t=0}$ . Vector meson dominance asserts that the colored part of the photon wave function is dominated by vector mesons; therefore, the photon is represented as a quark-antiquark pair in photoproduction calculations. These two components combine to produce Eq. 2.19.

$$\begin{aligned} \frac{d\sigma(\gamma p \rightarrow Vp)}{dt} \Big|_{t=0} &= \frac{4\pi\alpha}{f_V^2(M_V, \Gamma_{l+l^-})} \frac{d\sigma(Vp \rightarrow Vp)}{dt} \Big|_{t=0} \\ \sigma(Vp)_{tot}^2 &= 16\pi \frac{d\sigma(Vp \rightarrow Vp)}{dt} \Big|_{t=0} \end{aligned} \quad (2.19)$$

In Eq. 2.19, the photon-proton scattering is related to meson-proton scattering through the photon-meson coupling, which depends on the vector meson's mass,  $M_V$ , and leptonic decay width,  $\Gamma_{l+l^-}$ .

The result of combining vector meson dominance and the optical theorem in Eq. 2.19 provides the cross section for a meson to scatter off a proton. The total proton-meson scattering cross section, provides the input to the Glauber model calculation of the nuclear photoproduction cross section.

The nucleus-meson scattering cross section relates to Eq. 2.19 through the Glauber model. The Glauber model allows for Eq. 2.19, the proton-meson scattering cross section, to be used to calculate a nucleus-meson scattering cross section. The Glauber model produces nuclear cross section calculations from nucleon (proton or neutron) interaction cross sections by use of  $T_{AA}$ . The combination of the mean number of nucleons in the overlapping region of a nucleus-nucleus collision,  $T_{AA}$ , the nucleon cross section,  $\sigma$ , and the Poisson distribution make-up the core of the Glauber model. For the total nucleus-meson scattering cross section, the equation has the following form:

$$\sigma_{tot}(VA) = \int d^2\vec{r} (1 - e^{-\sigma_{tot}(Vp)T_{AA}(\vec{r})}) \quad (2.20)$$

In Eq. 2.20, the term  $e^{\sigma_{tot}(Vp)T_{AA}}$  gives the probability of having no meson-nucleon scatterings from the Poisson distribution. The probability of having at least one scattering is given by subtracting one from the term  $e^{\sigma_{tot}(Vp)T_{AA}}$  in Eq. 2.20. As seen in Eq. 2.20, the Glauber model leverages scientific knowledge of the proton to understand of the nucleus. The Glauber model is the tool that combines the proton photoproduction data with nucleon distributions in the nucleus to produce a nuclear vector meson photoproduction cross section in the VMD approach.

Reversing the process used for the proton, Eq. 2.20, the meson nucleus scattering cross section, relates to forward nuclear photoproduction cross section through the optical theorem. The nuclear photoproduction cross section is the input to the calculation of the final result, the nuclear vector meson photoproduction cross section in UPC events. Eq. 2.21 uses the optical theorem to produce the nuclear photoproduction cross section from the nucleus-meson scattering cross section:

$$\sigma(\gamma A \rightarrow VA) = \frac{d\sigma(\gamma A \rightarrow VA)}{dt} \Big|_{t=0} = \frac{\alpha \sigma_{tot}^2(VA)}{4\pi f_v^2} \int_{t_{min}}^{\infty} dt |F(t)|^2 \quad (2.21)$$

$F$  in equation Eq. 2.21 is the Fourier transform of the nuclear density function,  $\rho_A$ . To produce the formula for calculating the UPC vector meson photoproduction cross section, Eq. 2.21 is combined with the photon flux incident on the nucleus, Eq. 2.17.

$$\sigma(AA \rightarrow AAV) = 2 \int dk \frac{dN_\gamma}{dk} \sigma(\gamma A \rightarrow VA) \quad (2.22)$$

The factor of 2 in Eq. 2.22 comes from the fact that both of the two colliding nuclei contribute. Combining the three elements of VMD, Eq. 2.22 is the final result of the VMD UPC photoproduction cross section calculation. Vector meson production rates in UPC collisions are predicted by Eq. 2.22, which can be confirmed or denied by experiment.

## 2.5 Leading Twist Approach Derivation

The LTA method for calculating UPC photoproduction cross sections combines elements of the Glauber model with direct use of gluon densities. The proton gluon density is modified by a nuclear modification function in the LTA method to produce the nuclear gluon density. The nuclear modification function converts the proton photoproduction cross section to a nuclear photoproduction cross section in the LTA method. The LTA method is different from the other methods in its direct use of the nuclear modification factor and how the nuclear modification factor calculation incorporates multiple scattering. The direct use of the nuclear modification factor produces the most gluon shadowing out of the three major methods, and results in the lowest cross sections. The LTA method is the easiest to constrain experimentally for this reason.

The LTA method uses the Weizsäcker-Williams approximation to calculate the photon flux created by the colliding nuclei. As in the VMD method, the probability of having no hadronic collisions modulates the flux. The photon flux for the LTA method has the following form [18]:

$$n_{\gamma/A}^i(\omega_\gamma) = \frac{2\alpha Z^2}{\pi} \int_{b_{min}}^{\infty} db \frac{x^2}{b} \left[ K_1^2(x) + \frac{K_0^2(x)}{\gamma_L^2} \right] P_0(b) P_C^i(b) \quad (2.23)$$

$$x = \frac{\omega b}{\gamma_L v}$$

The  $K_0^2(x)$  term contributes a photon flux in the transverse direction.  $P_C^i(b)$  is an additional modulation factor that requires various additional interactions. These interactions result in additional emissions of neutrons from the receding nuclei as the nuclei relax from excited states. The LTA flux reproduces the VMD result when the  $K_0$  term becomes negligible as  $\gamma_L$  approaches  $\infty$  and  $P_C^i = 1$  when all emissions are allowed. The terms  $P_C^i$  and  $K_0$  create additional ways to distinguish UPC events from nuclear collisions experimentally but leave the underlying interaction mechanism the same. For example, the additional terms in the LTA formulation of the photon flux produce calculations of asymmetric neutron emission, which separate UPC events from nuclear collisions.

The LTA method calculates the nucleon photoproduction cross section from the nucleon gluon density. Ref. [18] derives the nucleon cross section from derivations of the nucleon gluon densities from electron-proton scattering data and leading order perturbative quantum field theory calculations. The forward photoproduction cross section of the nucleon has the following form [18]:

$$\frac{d\sigma_{\gamma N \rightarrow J/\psi N}(t=0)}{dt} = \frac{16\Gamma_{l+l-}\pi^3}{3\alpha M_{J/\psi}^5} [\alpha_s \mu^2 x G_N(x, \mu^2)]^2 \quad (2.24)$$

Here  $G_N$  is the gluon density of the nucleon,  $x$  is the fraction of the nucleon's momentum the gluon carries, and  $\mu$  is related to momentum at which the nucleon is being probed, which is equal to  $M_{J/\psi}/2$  for  $J/\psi$  photoproduction. In Eq. 2.24 the nucleon cross section is explicitly connected to the gluon density. By connecting the gluon density to the cross section, Eq. 2.24 allows for the gluon density to be experimentally probed.

Ref. [18] exploits the optical theorem to relate the forward photoproduction cross section of the nucleon to the nuclear cross section. Eq. 2.25 gives the relation:

$$\sigma_{\gamma A \rightarrow J/\psi A}(\omega) = \frac{d\sigma_{\gamma N \rightarrow J/\psi N}}{dt}(\omega, t_{min}) R_g^2 \int_{t_{min}}^{\infty} dt |F(t)|^2 \quad (2.25)$$

$$R_g = \frac{G_A(x, \mu^2)}{A G_N(x, \mu^2)}$$

$R_g$ , the nuclear modification function, is the ratio between the gluon density of the nucleon,  $G_N$ , to the gluon density of the nucleus,  $G_A$ . As with the VMD method, the optical theorem relates the forward cross section,  $\frac{d\sigma_{\gamma N \rightarrow J/\psi N}}{dt}(\omega, t_{min})$ , to the total cross section,  $\sigma_{\gamma A \rightarrow J/\psi A}$ . The LTA method relates the measurable UPC photoproduction cross section to the gluon density of the nucleus. Eq. 2.25 further connects the gluon density of the nucleon to the relative reduction of the gluon density in the nucleus through  $R_g$ .

From Eq. 2.25, the LTA method can predict the angular distribution of photoproduced  $J/\psi$  with respect to the beam axis. In Ref. [19] the angular distribution is expressed in the form of the rapidity dependency of the UPC photoproduction cross section.

$$\frac{d\sigma_{A_1 A_2 \rightarrow A_1 A_2 J/\psi}}{dy} = n_{\gamma/A_1}(y) \sigma_{\gamma A_2 \rightarrow J/\psi A_2}(y) + n_{\gamma/A_2}(-y) \sigma_{\gamma A_1 \rightarrow J/\psi A_1}(-y) \quad (2.26)$$

$$y = \ln\left(\frac{2\omega}{M_{J/\psi}}\right)$$

Eq. 2.26 is comprised of two terms, one for photons from the forward going nucleus interacting with the backward going nucleus, and a second for the reverse situation. The integration of Eq. 2.26 over  $y$  produces the factor of 2 that is present in Eq. 2.22. The rapidity distribution of the photoproduction cross section given in Eq. 2.26 provides a more detailed prediction and allows for more direct experimental comparison. Eq. 2.26 allows for comparison to rapidity regions that are covered by experiments.

The LTA method is distinct from the pQCD method and VMD method through the use  $R_g$ , the nuclear gluon modification factor. As opposed to using  $R_g$ , the pQCD method uses the nuclear gluon density, and VMD model uses proton photoproduction cross sections directly. In the LTA method,  $R_g$  is calculated through a combination of  $J/\psi$  photoproduction data from proton-electron scattering and DGLAP evolution equations, which incorporates nuclear multiple scattering effects [18]. The DGLAP evolution equations give the depends of nuclear gluon densities on the momentum scale at which the nucleus is probed,  $\mu$  in Eq. 2.24. The unique way the LTA method calculates  $R_g$  results in lower cross sections than the other major methods and allows for experimental sensi-

tivity. Experimental measurements of the UPC  $J/\psi$  photoproduction cross section with CMS have the opportunity to distinguish whether  $R_g$  as calculated in the LTA method accurately predicts the gluon density of the nucleus.

## 2.6 Perturbative Quantum Chromo-dynamics

To calculate the UPC  $J/\psi$  photoproduction cross section, the pQCD method uses the nuclear gluon density to characterize the nucleus and the Weizsäcker-Williams approximation for the probing photon flux. The pQCD method combines these components such that the nuclear gluon density is a direct variable. The nuclear gluon density term in the pQCD formulation allows for the use of a variety of nuclear gluon density models. A range of nuclear gluon densities are present in the available models resulting in a wide range of cross section values. The UPC  $J/\psi$  photoproduction cross section is correlated with the gluon density of the nucleus rising with higher densities and shrinking with lower densities. In the pQCD approach, the calculation of the UPC  $J/\psi$  photoproduction cross section allows experiments to constrain many different nuclear gluon density models.

In the pQCD method, the photon interacts with the nucleus by fluctuating to a quark-antiquark pair. For  $J/\psi$ , the photon fluctuates to a  $c\bar{c}$  pair. The probability for the photon to fluctuate to a  $c\bar{c}$  pair depends on the  $M_{J/\psi}$ , the mass of  $J/\psi$ ,  $\Gamma_{l+l-}$ , the  $J/\psi$  leptonic decay width, and  $\alpha$ , the electromagnetic coupling constant. These three variables connect the  $c$  quark to the electromagnetic force mediator, the photon. Recast as a  $c\bar{c}$  pair, the photon couples to the nuclear gluon density. Ref. [20] uses the fluctuation of the photon to a  $c\bar{c}$  pair as the foundation for calculating the forward  $J/\psi$  photoproduction cross section.

The  $c\bar{c}$  pair arising from the photon fluctuation scatters off the gluons of the nucleus. The density of gluons in the nucleus determines how likely and therefore how large the cross section is for the quarks to scatter and form a  $J/\psi$ . The forward scattering cross section is the portion of those scattering events which transfer the minimum amount of momentum between the photon and

the nucleus. The forward cross section for  $J/\psi$  photoproduction in the nucleus has the following form [20]:

$$\left. \frac{d\sigma_{\gamma A \rightarrow J/\psi A}}{dt} \right|_{t=0} = \xi_{J/\psi} \left( \frac{16\pi^3 \alpha_s^2 \Gamma_{l+l^-}}{3\alpha M_{J/\psi}^5} \right) [x G_A(x, \mu^2)]^2 \quad (2.27)$$

In Eq. 2.27,  $\xi_{J/\psi}$  is an experimentally derived correction factor,  $\alpha_s$  is the strong coupling constant,  $x$  is the momentum fraction of the nucleus the scattering gluons carry, and  $G_A$  is the gluon density of the nucleus. Both the  $c$  and  $\bar{c}$  couple to the gluon density, and the double coupling results in the squared dependence of the cross section on the gluon density in Eq. 2.27. Fitting Eq. 2.27 to proton-electron scattering data sets  $\xi_{J/\psi}$  [20]. The forward scattering cross section given by Eq. 2.27 connects the photon flux to the gluon density and provides the input to calculate the total cross section by the optical theorem. Eq. 2.27 is the crux of how UPC measurements provide insight into the gluon content of the nucleus.

The optical theorem relates the forward cross section in Eq. 2.27 to the total photoproduction cross section. The total cross section calculated by use of the optical theorem gives the probability that a photon incident on the nucleus will produce a  $J/\psi$  regardless of the momentum transferred in the interaction. Ref. [20] gives the form of the total cross section equation:

$$\sigma_{\gamma A \rightarrow J/\psi A}(k) = \left. \frac{d\sigma_{\gamma A \rightarrow J/\psi A}}{dt} \right|_{t=0} \int_{t_{min}(k)}^{\infty} dt |F(t)|^2 \quad (2.28)$$

Here  $t_{min} = (M_{J/\psi}^2/4k\gamma_L)^2$ , which is the minimum amount of momentum transfer required to produce a  $J/\psi$  given the photon wave number  $k$ . The  $k$  dependence of  $t_{min}$  produces the rapidity,  $y$ , dependence of the total cross section. The total cross section for photoproduction, Eq. 2.28, provides the input to Eq. 2.26, which gives the rapidity dependence of the UPC photoproduction cross section. Eq. 2.28 as input to Eq. 2.26 allows for experimental comparison of the pQCD method to measurements of UPC photoproduction cross sections. With the pQCD method's direct use of the nuclear gluon density in Eq. 2.27, the pQCD method allows for experimental exploration of any gluon density model.

## 2.7 Incoherent Photoproduction

## 2.8 Photon Induced Nuclear Break-up

Two different approaches are discussed. The first is to measure the desired cross-section directly. This can be done by bombarding the target material with mono-energetic real photons, varying the energies of the photons over a range of frequencies, and extrapolating that data up to the photon energies that arise in the Weizäcker-Williams approximation [3]. The other approach is to create a theoretical model of how the target reacts to a photon flux [4]. In the theoretical model that will be discussed in this paper, the photonuclear cross-section, the cross-section governing the absorption of photons by a nucleus, is formulated as the sum of two other cross-sections that are known better. In both, the more detailed theoretical approach and the empirical approach to the problem, the interaction of the Weizäcker-Williams quasi-real photons is assumed to be identical to the interaction of real photons with the target.

To model the interaction of the photons with the target nuclei, as done in Ref. [4], the photonuclear cross-section is broken down into two parts.

(16) The Giant Dipole Resonance (GDR) cross-section dominates at lower photon frequencies and is the result of the collective motion of the protons relative to the neutrons. The Quasi-Deuteron (QD) cross-section dominates at higher photon energies and is the result of treating the nucleus as a collection of proton-neutron pairs, which is deuterium.

The giant dipole resonance has been studied for decades. In 1947, Baldwin and Klaiber first observed the giant dipole resonance [6]. At the General Electric Research Laboratory, Baldwin and Klaiber found that by bombarding a uranium target with photons in the range 10 – 100 MeV, a peak in the spectrum was found for photons at 20 MeV. A year later, Goldhaber and Teller theorized that this was the result of the protons moving back and forth with respect to the neutrons [6]. In this model, the protons and neutrons are treated as two separate liquid dots. Then in 1950, Steinwedel and Jensen modified this theory by modeling the protons and neutrons as fluids contained in a single sphere rather than two separate dots moving back and forth [6].



In order to understand the Goldhaber and Teller model, it is useful to consider a nucleus where the number of protons and neutrons are equal,  $Z=A/2$ . The collection of protons and the collection of neutrons move opposite each other and only in the  $z$  direction. In order to construct a Hamiltonian, first the kinetic energy should be considered.

(17) Eq. 17 is the familiar equation for kinetic energy simply summed over all the constituent nucleons of the nucleus. The protons and neutrons are modeled as separate liquid drops with densities  $\rho_p$  and  $\rho_n$ . These liquid dots will oscillate back and forth in opposite phase relative to the center of mass maintaining their individual density profiles.

The potential holding protons and neutrons together depends on the difference of the two densities squared. If the two exactly overlap, there is no difference in the densities and the potential energy is zero. If the two density distributions are separated, there will be regions where the neutron density is greater and regions where the proton density is greater. In the separated configuration, there will be potential energy. The potential energy can be shown to have the form of a harmonic oscillator with a spring constant that depends on the initial density distribution [6].

(18) If the nucleus has a shape cut off in density at its very edge, then the integral is dominated by the region at the surface, and the spring constant  $K$  becomes proportional to the mass number to the 2/3rds power,  $A^{2/3}$ . This is the consequence of the geometry of a sphere. The surface area of a sphere is proportional to its volume to the 2/3rds power. Recalling the angular frequency of a harmonic oscillator, (19) it is seen that the frequency of the giant dipole resonance in the Goldhaber and Teller model is proportional to the mass number to the negative 1/6th power,  $A^{-1/6}$ . This dependence describes light nuclei well, but it does not describe heavier nuclei [6].

In order to describe heavier nuclei, the Steinwedel and Jensen model must be used. In the Steinwedel and Jensen model, the proton and neutron fluids are confined to a single sphere where they are allowed to slosh back and forth creating the same effect as the Goldhaber and Teller model. In this model, there is no global separation of the proton and neutron fluids. The dipole is created by underdensities and overdensities of the proton and neutron fluids. It can be shown that this results in a frequency of oscillation which depends on one over the radius of the nucleus [6]: (20)

As before, the relationship in Eq. 20 arises from the geometry of a sphere. The dependence of the giant dipole resonance that is seen in the Steinwedel and Jensen describes medium and heavier mass nuclei well. Empirically, both models are stitched together to give the following mass number dependence of the peak dipole resonance [6].

(21) In order to compute the effect of an excitation in either model, the harmonic oscillator solutions found earlier can be driven by an interacting force. The resulting differential equation can then be solved using a Fourier transform to eliminate the time derivatives and reduce the equation to an algebraic equation. Following this procedure produces the shape of energy dependence of the giant dipole resonance, and this gives a cross-section for photon absorption by the giant dipole resonance with Lorentzian form [6]: (22) here  $\sigma_{\max}$  is the maximum cross-section, when  $E\gamma = E_{\text{GDR}}$ ,  $E_{\text{GDR}}$  is the peak resonance energy, and  $\Gamma_{\text{GDR}}$  is the width of the resonance. The width,  $\Gamma_{\text{GDR}}$ , of this distribution lies in a range from 4-8 MeV and depends on the orbital arrangement to the neutrons and protons in the given nucleus [6].

For higher energy photons, the quasi-deuterium cross-section is needed. The quasi-deuterium approach amounts to treating the nucleus as a bunch of proton-neutron pairs, which are screened by the rest of the nucleus. Eq. 23 models this behavior [4].

(23) Here  $\sigma_d$  is the deuterium disintegration cross-section for  $\gamma + d \rightarrow p + n$ .  $F$  is a function that arising from Pauli blocking of fermions, and  $L$  is an empirical parameter set by data that is equal to 6.5. Certain energy levels are not available to the products of the deuterium disintegration process because of the presence of the rest of the nucleus. The result is a reduction of the cross-section.

$F$  can be modeled with an exponential cutoff below 20 MeV, a polynomial in the intermediate range with nearly linear dependence on  $E\gamma$ , and above 140 MeV an inverted exponential pushing  $F$  to one at higher values of  $E\gamma$  [4]. Essentially, the model at low photon energies disallows deuterium disintegration because the products have no available state to occupy, and at high energies the rest of the nucleus becomes transparent and looks more and more like a collection of deuterium. The deuterium disintegration cross-section is found empirically and is fit to the following function [4]: (24) In order to produce a final state for the target nucleus, a branching ratio is

needed. The branching ratio gives the probability that the photo-excited nucleus will end up in a particular state. This determines the sort of emission that will result from the de-excitation process. There are two phases of deexcitation, the nonequilibrium phase and the equilibrium phase. In the time before reaching equilibrium, fast nucleons are emitted. Subsequently, in the equilibrium phase, slow nucleons evaporate. These two phases are simulated in complex computer codes that calculate branching ratios (see discussion in Ref. [4]).

All the tools are now assembled to calculate the cross-section for any particular electromagnetic dissociation process. The first step in the calculation is to assume that the number of photons absorbed by either nucleus in the collision obeys the Poisson distribution [3,4]. An average number of absorptions is calculated and used in the construction of the distribution.

(25) When using the model of Ref. [4], the cross-section involved in Eq. 25 will be the photonuclear cross-section, and the calculation will produce the average number of photons absorbed by the target. If instead the empirically measured photoneutron cross-section is used as in Ref. [3], the mean calculated in Eq. 25 will be the number of photons absorbed that result in neutron emission from the target. This restricts the calculation to only de-excitation modes that produce neutrons. Both averages are for a given impact parameter  $b$ .

Following Ref. [3] and using the experimentally measured photoneutron cross-section, the probability  $P_n$  for the target to produce a number of neutrons,  $k$ , due to the photon flux of the projectile can be calculated using Eq. 26.

(26) This is just the Poisson distribution. In the collider situation, where both nuclei can be treated as the target and the projectile, the probability of mutual emission, one nucleus emitting  $x$  neutrons and the other emitting  $y$  neutrons, can be calculated from Eq 27.

(27) It is also interesting to consider the situation where at least one neutron is emitted. This can be calculated by subtracting the probability of no neutrons being emitted from one.

When using the model of Ref. [4], a branching ratio is needed to calculate the probability of de-exciting into a given state. The probability of photon absorption is calculated as in Eq. 26, only using the model of Ref. [4]. This is the probability of the target absorbing  $k$  photons rather than

then the nucleus absorbing a photon and emitting a neutron. In Ref. [4], the probability of any final state  $i$  due to the absorption of a single photon can be calculated using Eq. 28.

(28) Here  $P_a$  is the probability that the target absorbs a single photon as calculated by Eq. 26,  $q$  is the probability that the photon will have the frequency  $\omega$ , and  $f_i$  is the branching ratio. The following equation describes  $q$  [5].

(29) By multiplying Eq. 26 and 29 in Eq. 28, the  $m(b)$  terms cancel and produce a simplified equation. The forms for probability functions, like Eq. 28, that involve absorption of multiple photons have additional terms. But they follow that same scheme of multiplying the probability of absorption times the probability that the absorbed photon has a particular frequency times the branching ratio.

The probability functions Eq. 26 and Eq. 28 can then be used to produce cross-sections. For any given process, using Eq. 28 can be used by inserting the appropriate branching ratio. For emission of neutrons, Eq. 26 can be used. This is done by integrating over the impact parameter to get an area that is weighted by the probability functions [3,4].

(30) If the branching ratio for neutron emission is selected in Eq.28, then Eq.28 and Eq.26 can be used to compute the same cross-section through the use of Eq.30.

Three parameters arise when calculating the cross-section in Eq. 30, the minimum impact parameter  $b_0$ , the minimum emitted photon frequency  $\omega_{\min}$ , and the maximum emitted photon frequency  $\omega_{\max}$ . The need for a minimum impact parameter is necessitated by the Bessel function in the photon flux in Eq. 14. At zero, the modified Bessel function does not converge. Physically, a minimum impact parameter is selected in order to separate the domains between electromagnetic interactions and the strong interactions that happen inside the nucleus. To serve this end, the minimum impact parameter is set to the radius of the nuclei [3,4]. This excludes collisions where the nuclei overlap in the calculation, and assures only electromagnetic interactions are involved.

Model	$\sigma_{AA \rightarrow AAJ/\psi}(mb)$
VMD/STARlight MC	23
LTA	9
pQCD-MSTW08	34
pQCD-EPS08	7
pQCD-EPS09	14
pQCD-HKN07	23

Table 2.1:  $\sigma_{AA \rightarrow AAJ/\psi}(mb)$  the LTA, VMD, pQCD methods. Four different gluon density models are used in the pQCD method. STARlight is a simulation software package that utilizes the VMD model.

## 2.9 Theoretical Results

The UPC photoproduction cross section calculations depend significantly on how the nucleus is represented in the calculation. The results from the VMD, LTA, and pQCD methods vary from a relatively large cross section in the VMD model, ranging through a variety of values in the pQCD method, to a relatively small cross section in the LTA method. Each of these methods utilizes the same probe of the nucleus, the equivalent photon flux that is calculated using the Weizsäcker-Williams approximation. The three methods deviate in how they calculate the forward photoproduction scattering cross section. The differences in the UPC photoproduction cross sections predicted by the different models demonstrates the amount of experimental sensitivity there is to distinguishing between the models. The dependence of the cross section on rapidity shows where in phase space a measurement of the cross section is most sensitive.

The predicted value for the UPC  $J/\psi$  photoproduction cross section in PbPb collisions at the LHC differ widely depending on which of the three main methods is used. The cross section value calculated by Eq. 2.22 in the VMD, LTA, and the various gluon density models in pQCD method vary significantly. Table 2.1 gives the predicted values for the three main methods taken from Ref [21], Ref [18], and Ref [17]. The cross sections in Table 2.1 differ by a factor of  $\approx 4$  from the smallest to largest and create an experimental opportunity. The clear discrepancy between the models in Table 2.1 demonstrates the high amount of experimental sensitivity there is for distinguishing between the models.

The rapidity dependence of the cross sections determine which values of rapidity will be most sensitive to differences in the models. The rapidity dependence calculated by Eq. 2.26 overlap between the models at certain values of  $y$  leaving the models indistinguishable at that rapidity. Fig. 2.4 [22] shows the rapidity dependency of the UPC  $J/\psi$  photoproduction cross section for the three main models including several different gluon density models using the pQCD method. In

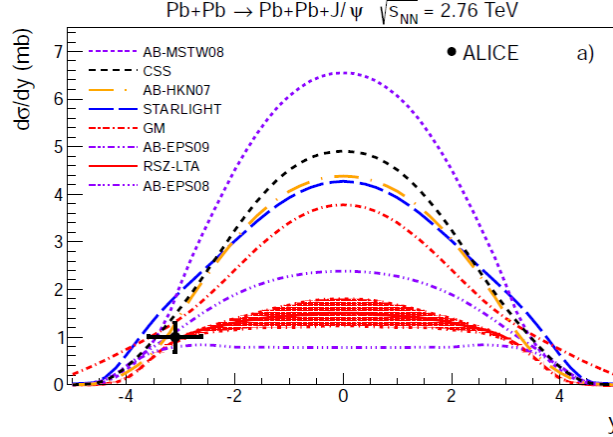


Figure 2.4: AB is the pQCD method, RSZ-LTA is the LTA method, and STARlight is the VMD model.

Fig. 2.4 at higher rapidities, in particular  $|y| > 3$ , the various models give similar values for  $d\sigma/dy$ . At  $y = 0$  the models vary the most. Fig. 2.4 shows that experiments that can measure  $J/\psi$  at  $y = 0$  have the best opportunity to distinguish between the models. The high sensitivity at  $y = 0$  creates an advantage for experiments that can measure particles with small rapidity and low momentum.

The UPC photoproduction models each have different shapes to their rapidity dependence. The slope of  $d\sigma/dy$  in Fig. 2.4 depends on the model. Through the rapidity region  $1 < |y| < 3$ , each of the models has a progressively steeper slope. The LTA method and the pQCD method utilizing the EPS08 gluon density model are relatively flat where as the VMD and other gluon density models using the pQCD method have a noticeable slope. The differing slopes provide an additional experimental observable. The shape of the rapidity distributions provide experimental sensitivity at rapidities away from  $y = 0$  and creates an opportunity for experiments that can not measure  $J/\psi$  at  $y = 0$ .

The nuclear suppression factor,  $S$ , demonstrates the difference between how the models represent the nucleus.  $S$ , which is a ratio between the nuclear photoproduction cross section and the free nucleon photoproduction cross section, is a measure of how the nuclear gluon densities evolve in each of the models. Fig. 2.5 from Ref.[23] shows the nuclear suppression, which is equivalent to  $R_g$  in Eq. 2.25, for the LTA and pQCD method. Fig. 2.6 shows the nuclear suppression for

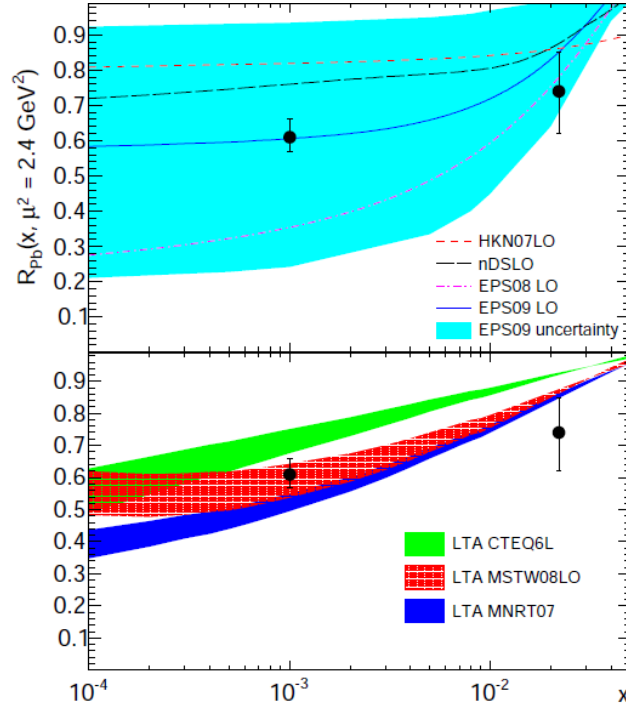


Figure 2.5: Nuclear suppression factor,  $S$ , in the pQCD and LTA methods.

the VMD method [23]. Fig. 2.6 and Fig. 2.5 show that as the momentum of the probing photon goes up, increasing  $W_{\gamma p}$ , and momentum of the probed gluon goes down, decreasing  $x$ , the nuclear gluon density decreases relative to the free nucleon. The nuclear suppression factor,  $S$ , allows for the different models' representations of the gluon content of the nucleus to be directly compared to each other and to data.  $S$  can be measured from data by assuming a Weizsäcker-Williams photon flux and provides insight into nuclear gluon densities.

## 2.10 Experimental Results

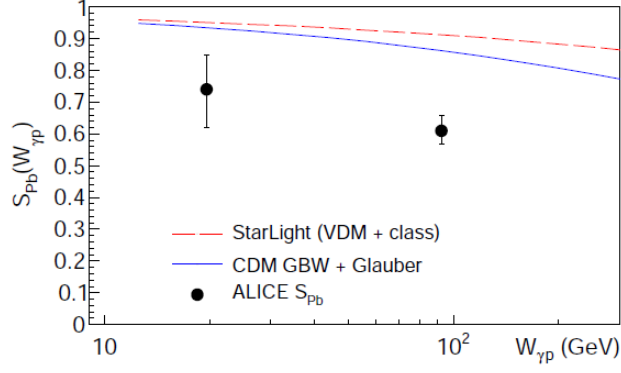


Figure 2.6: Nuclear suppression factor,  $S$ , in VMD method.

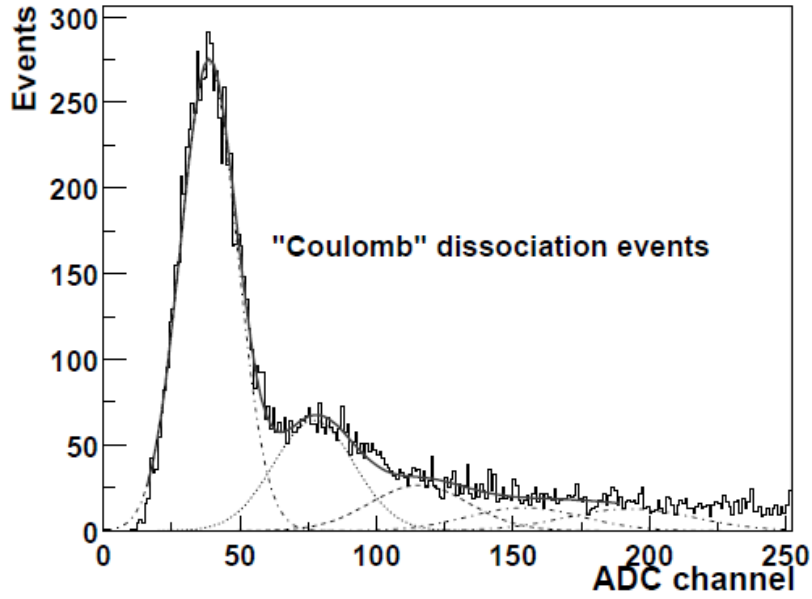


Figure 2.7: from [4]

TABLE I. Ratios of cross sections for experiment and theory. The values of  $\sigma_{\text{tot}}$  and  $\sigma_{\text{geom}}$  are in barns.

$\sigma_i$	PHENIX	PHOBOS	BRAHMS	[3]	[4]
$\sigma_{\text{tot}}$	...	...	...	$10.8 \pm 0.5$	11.2
$\sigma_{\text{geom}}$	...	...	...	7.1	7.3
$\frac{\sigma_{\text{geom}}}{\sigma_{\text{tot}}}$	$0.661 \pm 0.014$	$0.658 \pm 0.028$	$0.68 \pm 0.06$	0.67	0.659
$\frac{\sigma(1,X)}{\sigma_{\text{tot}}}$	$0.117 \pm 0.004$	$0.123 \pm 0.011$	$0.121 \pm 0.009$	0.125	0.139
$\frac{\sigma(1,1)}{\sigma(1,X)}$	$0.345 \pm 0.012$	$0.341 \pm 0.015$	$0.36 \pm 0.02$	0.329	...
$\frac{\sigma(2,X)}{\sigma(1,X)}$	$0.345 \pm 0.014$	$0.337 \pm 0.015$	$0.35 \pm 0.03$	...	0.327
$\frac{\sigma(1,1)}{\sigma_{\text{tot}}}$	$0.040 \pm 0.002$	$0.042 \pm 0.003$	$0.044 \pm 0.004$	$0.041 \pm 0.002$	...

Figure 2.8: from [4]



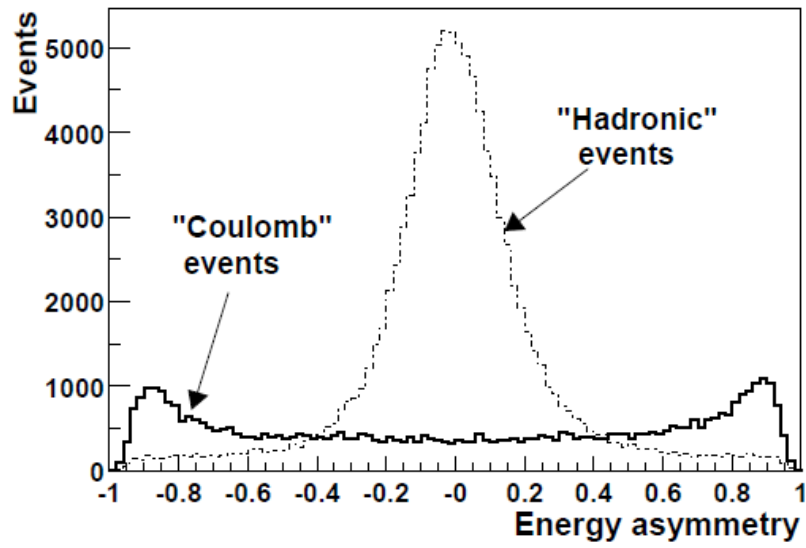


Figure 2.9: from [4]

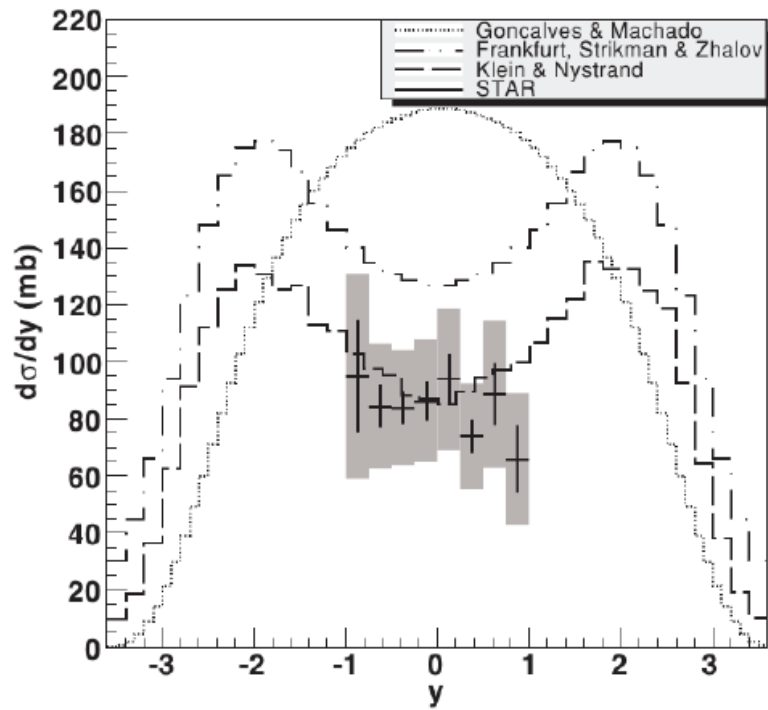


Figure 2.10: from [5]

Cross section	STAR		
	$\sqrt{s_{NN}} = 62.4 \text{ GeV (mb)}$	$\sqrt{s_{NN}} = 130 \text{ GeV (mb)}$	$\sqrt{s_{NN}} = 200 \text{ GeV (mb)}$
$\sigma_{XnXn}$	$10.5 \pm 1.5 \pm 1.6$	$28.3 \pm 2.0 \pm 6.3$	$31.9 \pm 1.5 \pm 4.5$
$\sigma_{0nXn}$	$31.8 \pm 5.2 \pm 3.9$	$95 \pm 60 \pm 25$	$105 \pm 5 \pm 15$
$\sigma_{0n0n}$	$78 \pm 14 \pm 13$	$370 \pm 170 \pm 80$	$391 \pm 18 \pm 55$
$\sigma_{total}$	$120 \pm 15 \pm 22$	$460 \pm 220 \pm 110$	$697 \pm 25 \pm 73$

Figure 2.11: from [5]

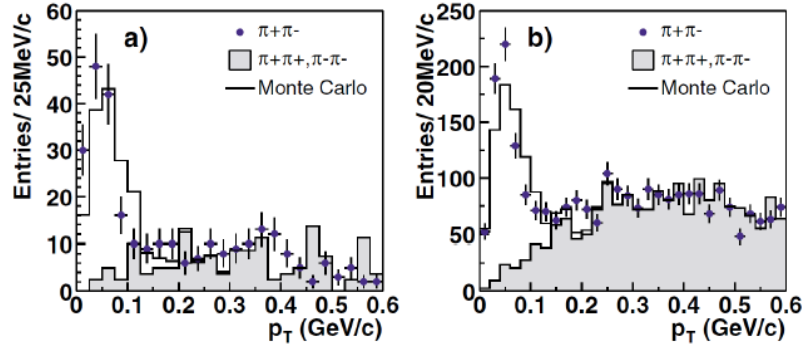


Figure 2.12: from [6]

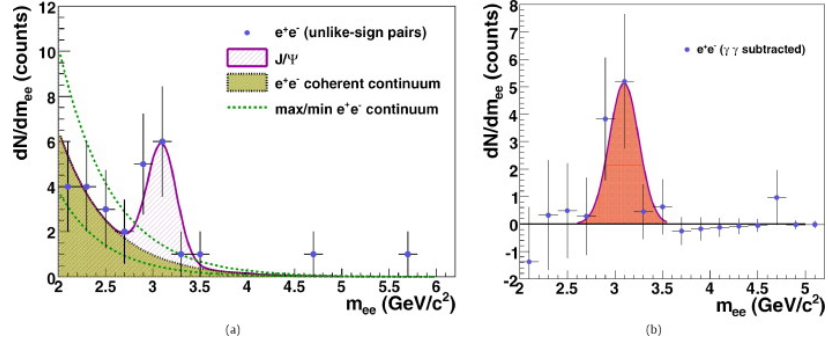


Figure 2.13: from [7]

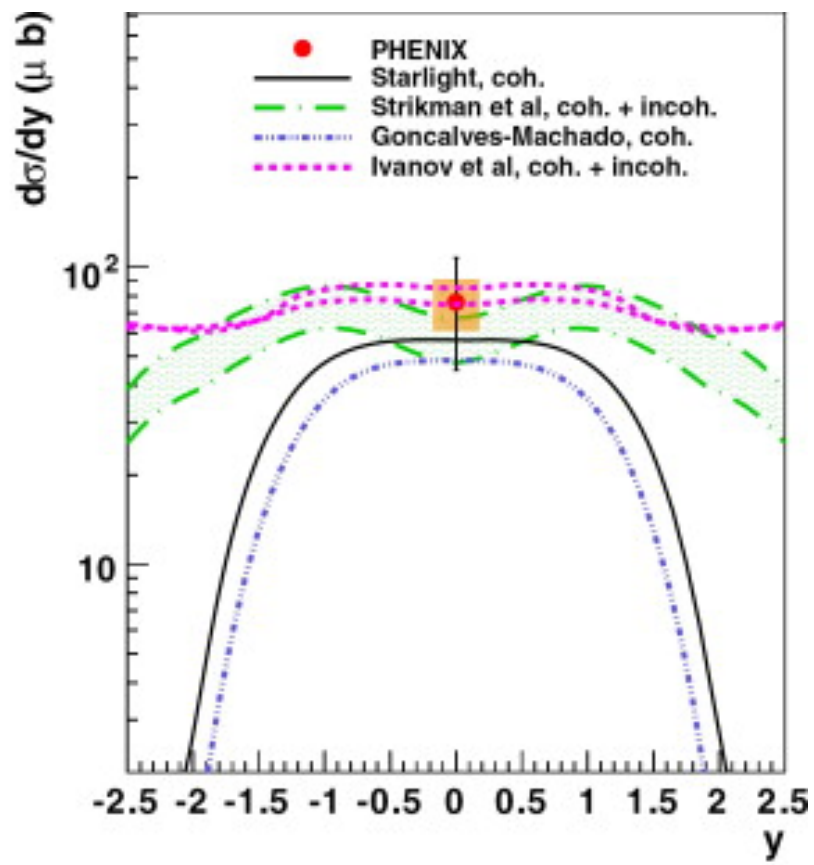


Figure 2.14: from [7]

# Chapter 3

## The CMS Detector

CMS is housed at interaction point 5 of the LHC. The LHC is designed to pursue physics at the TeV scale. This is the scale where electroweak symmetry breaking is believed to occur [24]. While this means that the search for the standard model Higgs boson was the central driving design consideration, the wide range of possibilities for finding new physics signals requires a general purpose detector. The expedient discovery of new physics through low cross section interactions requires high luminosity. While the difference is scale, 125 GeV for the mass of the Higgs boson as compared to 3.1 GeV for the mass of the  $J/\psi$ , create difficulties which will be discussed below, these two considerations created the opportunity to explore UPC  $J/\psi$ . Prior to the discovery of the Higgs boson, the decay  $H \rightarrow Z^0 Z^{0*} \rightarrow \mu^+ \mu^- \mu^+ \mu^-$  because very few other process can create a four muon final state. Muon capabilities developed for this process can be used to study  $J/\psi$ , which also decays to muons. A versatile trigger is needed to accommodate the high interaction rates that accompany the high luminosities. By exploiting the versatility of the trigger and CMS's muon systems it is possible to explore process like UPC  $J/\psi$  production, which push to the very edge of the detectors capabilities.

The general purpose design of CMS is dominated by the massive 4T superconducting solenoid at its core. The magnets is 13m long with a 6m diameter, and pushes the limits of power and compactness [8]. These two conflicting limits are achieved through the novel design of interweaving

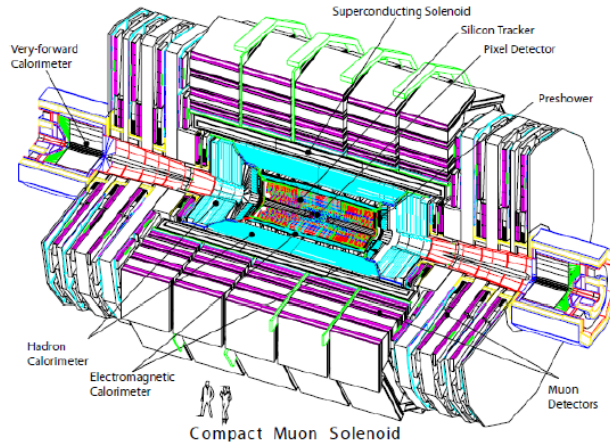


Figure 3.1: The Compact Muon Solenoid from Reference [8].

structural and conducting elements together in the coil of the solenoid.

Within the solenoid resides three different sub detectors. The inner most is the world’s largest silicon tracker [8]. The tracker is surrounded by a highly effective lead tungstate crystal electromagnetic calorimeter (ECAL). ECAL is encapsulated in a brass scintillating hadronic calorimeter (HCAL). Outside the magnet, muon chambers are used to aid in the measurement and triggering of muon events. Altogether CMS weighs 12,500 metric tons, has a diameter of 14.6m, and a length of 21.6m [8].

### 3.1 Tracker

The Silicon Tracker is the innermost sub-detector of CMS, and has active elements as close as 4.4cm to the interaction point [8]. The tracker has a length 5.8m, a diameter of 2.6m and covers a range in pseudorapidity of  $|\eta| < 2.5$ . At the center of the tracker are three rings of silicon pixels around the beam with two disks of silicon pixels to cap the rings. The pixel portion of the silicon tracker is comprised of  $66 \times 10^6$  pixels. The silicon pixels are surrounded by silicon strips. The silicon strips are separated into 4 different sections: the Tracker Inner Barrel, the Tracker Inner Disk, the Tracker Outer Barrel, and the Tracker End Caps. The silicon strip detectors as a whole are comprised of  $9.3 \times 10^6$  silicon strips. The high number of pixels and strips allow for the ability

to distinguish and collect enough distinct points to reconstruct the path of the 1000 or so charge particles per bunch crossing expected at peak luminosity [8].

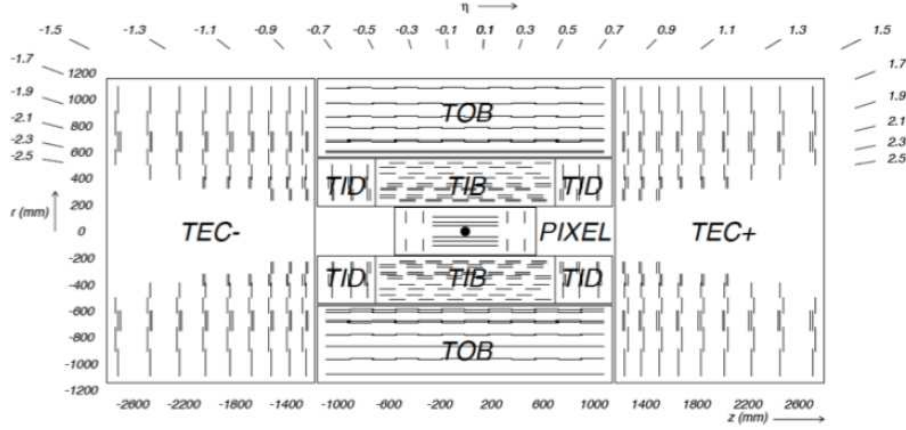


Figure 3.2: Layout of the silicon tracker with the pixels closest to the interaction point marked with a black dot and the strips segments beyond making up the remainder.

The amount of material present in the tracker is substantial enough to alter the path of particles as they pass through the tracker. Fig. 3.3 shows the amount of material in the tracker as a function of radiation lengths ( $X_0$ ). The radiation length is the mean distance a high energy particle travels before giving up one e-fold of kinetic energy through electromagnetic interactions. For example, after one radiation length  $E \rightarrow E/e$ , where  $e = 2.71828183$ . As opposed to the deflection angle set by the strength of the magnetic field, momentum resolution for lower momentum tracks is limited by the lose of energy due to scattering of these particles off the material of the detector. For UPC  $J/\psi$ , this is the primary factor contributing to the resolution of the reconstructed muon tracks.

## 3.2 ECAL

The next detector beyond the tracker is ECAL. ECAL is made of 61,200 lead tungstate ( $\text{PbWO}_4$ ) crystals in the central barrel and 7,324 on each of the two endcaps [8]. The barrel (EB) covers a pseudorapidity range  $|\eta| < 1.479$  and has an approximate  $\eta - \phi$  segmentation of  $0.0174 \times 0.0174$ . Lead tungstate is very dense, which is reflect in the high number of interaction lengths the short depth of one crystal provides. The crystals of the barrel have a depth of 230 mm corresponding

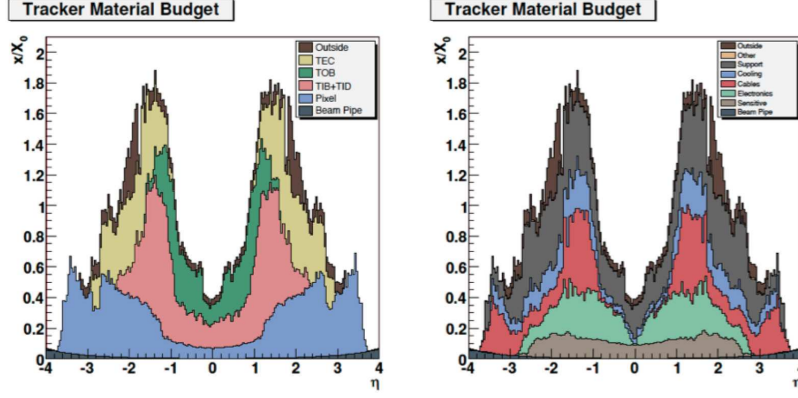


Figure 3.3: Material in the tracker broken down by sub-detector(left) and category (right).

to  $25.8 X_0$ . The endcaps (EE) cover the pseudorapidity region  $1.479 < |\eta| < 3$ . In the endcap the crystals have an exposed area of  $28.62 \times 28.62 \text{ mm}^2$ , and a depth of 220 mm corresponding to  $24.7 X_0$ . The energy resolution of the ECAL as measured by test beam data can be seen in Figure 3.4.

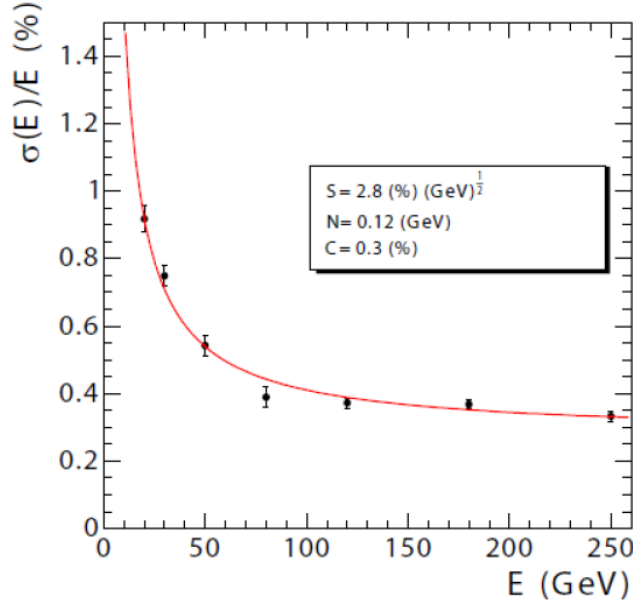


Figure 3.4: The energy resolution of ECAL as a function of energy from Reference [8].

### 3.3 HCAL

The HCAL like the ECAL has both a barrel (HB) and endcaps (HE). The pseudorapidity region  $|\eta| < 1.3$  is covered by HB [8]. HB has an  $\eta - \phi$  segmentation of  $0.0897 \times 0.0897$ , and is 25 times

more sparsely granulated than EB. HE covers the pseudorapidity region  $1.3 < |\eta| < 3$ . HE, like EE and the tracker endcaps, is aligned perpendicular to the beam axis resulting in granularity that changes with  $\eta$ . In the region  $1.3 < |\eta| < 1.6$  HE has an  $\eta - \phi$  segmentation of  $0.0897 \times 0.0897$ . The  $\eta - \phi$  segmentation roughly doubles to  $0.17 \times 0.17$  in the region  $1.6 < |\eta| < 3$ . The energy resolution of the barrel and endcaps can be seen in Figure 3.5. The thickness of the hadronic calorimeter is best described in interaction lengths, the mean distance for a particle to give up an e-fold of energy through nuclear interactions. At  $\eta = 0$  the barrel has a thickness 5.82 interaction lengths ( $\lambda_I$ ), and increases as the path length through the material increases to  $10.6 \lambda_I$  at  $|\eta| = 1.3$ .

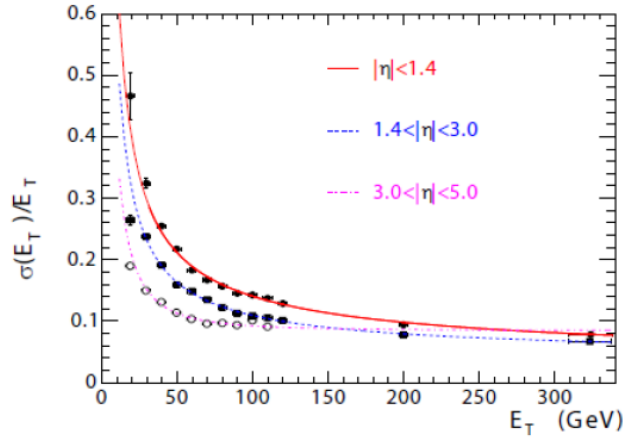


Figure 3.5: The  $E_T$  resolution of HCAL as a function of  $|\eta|$  and  $E_T$  from Reference [8].

In addition to HB and HE, HCAL has two additional calorimeters. Because the space between ECAL and the magnet is restricted to 1.18 m, an outer hadronic calorimeter section (HO) is placed beyond the magnet in the region  $|\eta| < 1.3$  [8]. The main function of HO is to collect energy from the highest energy hadrons before they reach the muon system. HO is not used in this analysis, but does contribute to the material budget. To increase the total calorimetric coverage, HCAL also has a quartz fiber calorimeter (HF) in the forward region,  $3 < |\eta| < 5$ . For the majority of HF's 13  $\eta$  rings the  $\eta - \phi$  segmentation is  $0.175 \times 0.175$ . In the lowest  $|\eta|$  ring the segmentation is  $0.111 \times 0.175$  in  $\eta - \phi$ . In the highest two  $|\eta|$  rings the segmentation in  $\phi$  is 0.349, with an  $\eta$  segmentation of 0.175 in the outer and 0.300 in the innermost ring. The longitudinal direction



is effectively segmented by using short fibers and long fibers. The measure energy deposited deeper than 22 cm is measured in both the short and long fibers, where as the long fibers are present throughout. This allows electromagnetic showers to be distinguished from purely hadronic showers [8]. The energy resolution for HF can be seen in Figure 3.5.

### 3.4 ZDC

Beyond HF, the Zero Degree Calorimeters(ZDC) covers the very forward rapidity region. ZDC sit between the beam pipes on either side of the interaction point covering the area around  $\theta = 0$ ,  $|\eta| > 8.3$ . In heavy ion collisions the ZDC has the ability to measure neutral particles that do not participate in the collision [8].

The ZDC has a total of 18 channels. Half of these 18 channels are on either side of the interaction point. The 9 channels on the side of CMS that correspond to positive  $\eta$  are denoted  $ZDC^+$ , where as the 9 channels on the negative side are denoted  $ZDC^-$ . The 9 channels on each side are further sub-divided into an electro-magnetic (EM) section and a hadronic (HAD) section. The EM section is positioned in front of the HAD section with respect to the interaction point and is segmented transverse to the beam direction. The 5 EM sections are positioned in front to absorb the energy from electro-magnetically induced showers, which develop over a shorter distance than hadronically induced showers. The transverse segmentation allows for a measurement of the transverse shower width and the size of the beam spot at the ZDC. The HAD section is segmented in the direction of the beam and consists of 4 channels. The longitudinal segmentation allows for absorption of the full extended hadronic shower and the ability to measure the longitudinal shower shape.

Each the 18 channels contains a tungsten target and quartz fibers. The dense tungsten target is used to initiate the shower. The quartz fibers shine Cerenkov light as the high momentum charged particles from the shower pass through it. the light from the quartz fibers is channeled to photo-multiplier tubes, one for each ZDC channel. Through a cascade of photon induced electrical

discharges, the photo-multiplier converts the Cerenkov light to an electrical pulse.

This electrical pulse travels  $\sim 200$  m down a coaxial cable from the LHC tunnel to the counting house in the CMS service cavern. There the electrical pulse is digitized by the Charge Integrator and Encoder (QIE). The QIE integrates the current each 25 nano seconds. The charge is then mapped logarithmically to the 128 bits. This bit is sent across a small fiber optic cable to the HTR firmware card. Here each 25 ns signal is stored in a 250 ns buffer, and the timing is sync with the rest of the detector to insure the ZDC signal arrives at the central data acquisition system at the same time as the other sub detectors from the same collision.

### 3.5 Muons

The muon system resides just outside of the superconducting magnet. It consists of three complementary systems: drift tube (DT) chambers in the barrel, cathode strip chambers (CSC) in the endcaps, and resistive plate chambers (RPC) in both the barrel and endcap regions [8]. Each of the gaseous detectors function in the same basic way. As the muon penetrates the gas volume electrons are knocked off of the gas atoms and these electrons are collected in the positively charged anode, where as the ionized gas moves to the cathode. The DTs in the barrel and the CSCs in the endcap have better spatial precision relative to the RPCs, which have are quicker and have more precise timing. The combination of the DTs and RPCs in the barrel and the CSCs and RPCs in the endcap allow for fast triggering and muon identification during data reconstruction.

As seen in Fig. 3.6, the DTs reside only in the barrel, covering the region  $|\eta| < 1.2$ . Consisting of a total of 172,000 cells, the DT cells are collected into 250 chambers. The DT chambers are interwoven into the magnet field return yoke and are labeled by 5 segmentations in  $z$ , YB-2 to YB+2. Each  $z$  segment is divided into 12  $\phi$  segments labeled 1 at  $\phi = 0$  and going to 12 rotating in positive  $\phi$  with segments 4 and 10 contain 2 chambers. The segmentation in  $r$  is divided in to four parts, MB1-MB4. Fig. 3.7 shows how each chamber is made of three super layers. Super layers  $SL \Phi_1$  and  $SL \Phi_2$  measure  $(r, \phi)$ , whereas  $SL \Theta$  measures  $z$ .

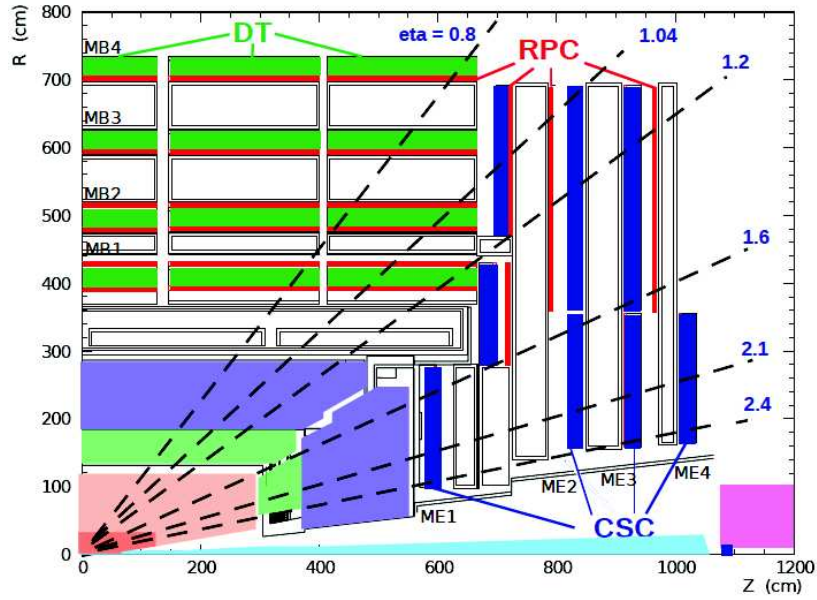


Figure 3.6: The CMS muon system showing the four DT stations in the barrel (MB1-MB4), the four CSC stations in the endcap (ME1-ME4), and the RPC stations.

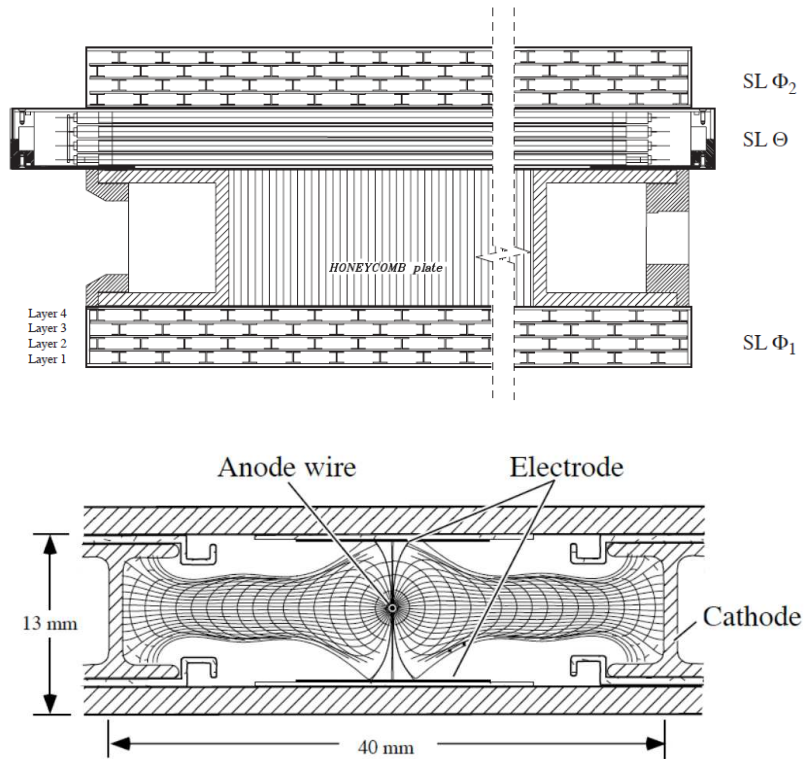


Figure 3.7: Schematic of the DT chambers and an individual DT cell.

The RPC complement the DTs in the barrel and the CSCs in the endcap primarily for the purpose of triggering.

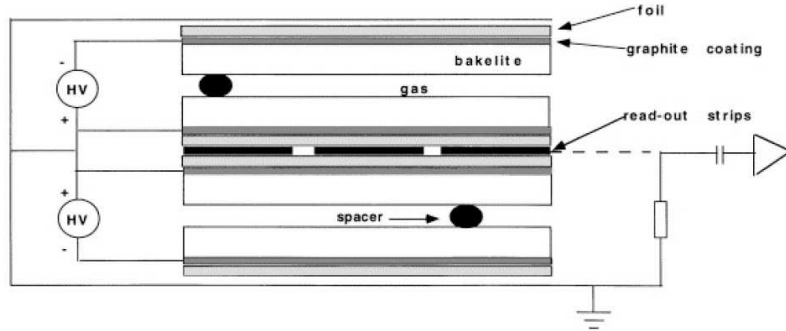


Figure 3.8: Schematic of a RPC cell.

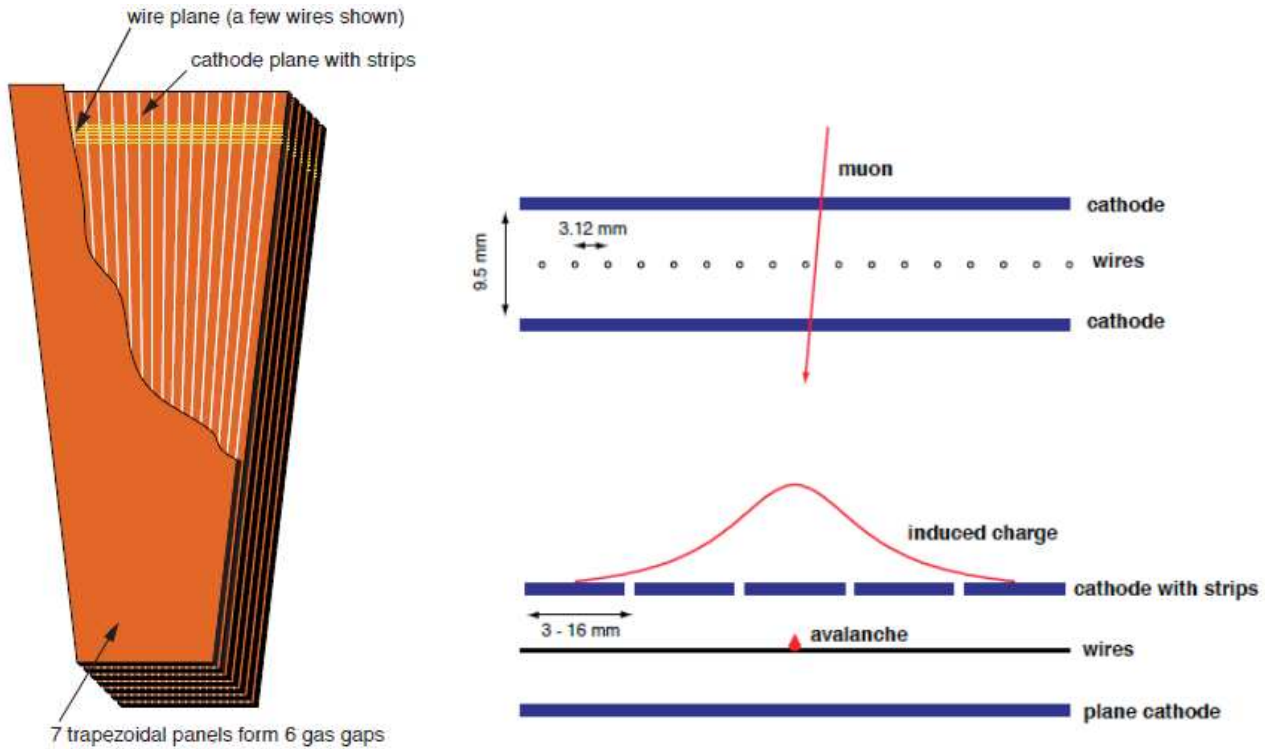


Figure 3.9: Schematic of the CSC chambers and an individual CSC cell.

The primary function of the muon systems are to allow for triggering on and identification of muons. The tracker is still the primary instrument for measuring the muons. Fig. 3.10 shows the resolution of reconstructed muons with the tracker only is only improved upon for muons with momenta above 100 GeV. For UPC  $J/\psi$  events where muons momenta are between 1-2 GeV, the

muon system does not provide any advantage in terms of improved resolution. The muon system does distinguish muons from other particles. Because of their increase mass relative to electrons, muons emit less bremsstrahlung, or breaking radiation, as it penetrates the inner layers of the CMS on it's way to the muon systems. Fig. 3.11 shows the amount of material traversed by particles traveling through CMS as a function of  $|\eta|$ . The total of nearly 10 interaction lengths between the interaction point and the muon chambers, ensures that hadrons like charged pions, which nearly exclusively decay to muons, are collected in the calorimeters before converting to muons. By eliminating backgrounds from both electrons and hadrons, the CMS muons system allows for identification of muons for both triggering and reconstruction.

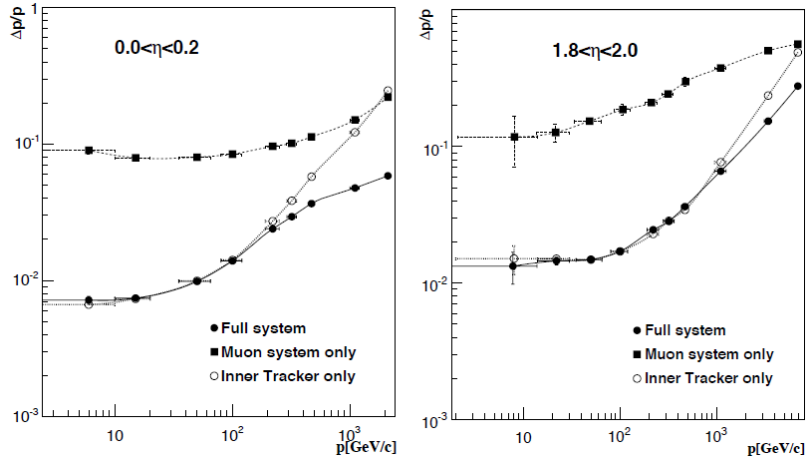


Figure 3.10: The momentum resolution of the muon system using only the tracker and the whole muon system in the barrel (left) and end cap (right).

i

The low-momentum nature of UPC physics creates complications due to the large amount of material between the interaction point and the muon systems. About 3 GeV of momentum is needed to reach the first layers of the muon system. In the rest frame of the  $J/\psi$ , the  $J/\psi$  equally shares its rest mass with its decay products creating 2 muons with momenta of about 1.5 GeV. For these daughter muons to reach the muon system, their parent  $J/\psi$  must be pushed to higher momentum by the initial particles which created the  $J/\psi$ . For this reason, muons from UPC  $J/\psi$ s are only detected at higher  $\eta$  values. Understanding this momentum restriction of the muon system

was a major focus of the analysis discussed in this thesis with details described in Section. 4.6.

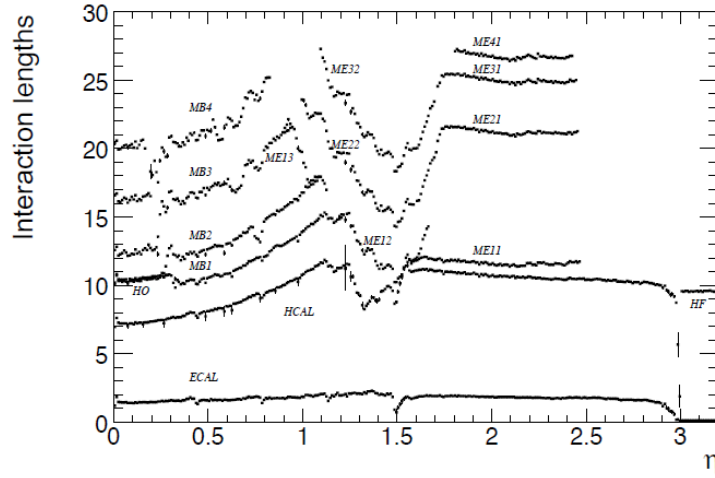


Figure 3.11: The amount of material in CMS as a function of  $\eta$  in number of interaction lengths.

### 3.6 Trigger

The CMS trigger is two tiered. The L1 trigger is the lower level hardware based system. The High Level Trigger (HLT) is software base and runs on a computer farm at point 5 where CMS is housed.

The purpose of the L1 trigger is to make quick decisions about which events will be kept temporarily for further processing. The L1 trigger is used to identify events where the tracker should be read out. Only the calorimeters and the muon system are used in the L1 trigger. Each of the sub-detectors has its triggering hardware. The output from the sub-detectors is synchronized to ensure that the signal from each of the sub-detectors comes from the same collision. The global trigger hardware then makes the final decision to initiate the HLT and to read out the tracker.

If an event passes the L1 trigger, the data from all the sub-detectors including the Tracker are sent to the HLT computing farm. At this level the raw data from all the sub-detectors is unpacked and combined. The information from the calorimeters, muon system, and tracker can all be used to reconstruct basic physics objects in the HLT farm. For example, tracks can be combined with either ECAL energy clusters to form electron candidates, tracks can be combined with hits in the

muon system to create muon candidates. At the HLT the whole detector is used together to select events. The raw data from the events that survive the HLT are recorded permanently, those that do not are lost forever.

The HLT farm must always be ready to accept events from the L1 trigger. For this reason, the amount of computing time each HLT trigger path uses must be balanced. For more rare L1 triggers, which will occur at a lower rate, more complex reconstruction software can be used. Conversely, simpler, faster, methods must be used for more common high rate triggers. Because of this time constraint in the HLT farm, the reconstruction algorithms used for triggering tended to differ from the final reconstruction algorithms. In the HLT these algorithms are optimized for quickness, whereas the final reconstruction is optimized for precision and accuracy. By having the ability to spend different amounts of computing time on different L1 triggered events, the complexity of the event selection offered by the HLT is heightened.

The two tiered triggering system creates very low dead times while maintaining purity and selectivity. During data taking the L1 trigger is continuously monitoring, and the HLT allows for sophisticated event selection. The wide gamete of physics topics that are pursued by the CMS collaboration are a testament to the effectiveness and versatility of the CMS two tiered triggering system.

# Chapter 4

## Analysis

In this chapter the various parts of the analysis are explained. In Section 4.1, the simulations used to estimate the detector's ability to measure UPC processes are discussed. Section 4.2 explains the considerations that went into the triggers that were developed for this measurement. The selection of UPC events is detailed in Section 4.3. Extraction of the number of coherent  $J/\psi$  candidates is explained in Section 4.5. The determination of the detector's efficiency for measuring UPC events is explained in Section 4.6. Finally, Section 4.7 lays out the systematic uncertainties for the measurement.

### 4.1 MC simulation

Every physical measurement is the product of the underlying physics folded with the response of the detector used to do the measurement. In order to understand the underlying physical process, the detector's effect on the measurement must be understood and accounted for. As instruments become more and more complicated, the interplay among all of the many parts of the detector makes an analytic approach to the problem untenable. For this reason, the numerical technique of Monte Carlo (MC) simulation is often the most effective approach.

MC simulations use random number generation to model the many statistical effects of particles interacting with different parts of the detector. First, particles are generated according to



theoretical distributions. These particles are then propagated through a simulation of the detector. As the particles pass through the detector, random numbers are again used to determine how these particles interact with the materials of the detector based on the known properties of the material. In this way, the theoretical distributions are convolved with a realistic model of the detector's response. A more detailed picture of how the detector shapes the underlying distributions emerges with each successive event. The set of events that are produced resemble as closely as possible the results that would be seen were the physical process to be measured by the detector.

In this thesis, two main classes of MC simulation samples were used, STARlight and a particle gun. The STARlight samples corresponds to the theoretical calculations described in Section 2.4, while the particle gun produces particles with a user defined momentum distribution. For STARlight three different physical process are simulated; coherent  $J/\psi$  production, where the photon couples to the nucleus as a whole, incoherent  $J/\psi$  production, where the photon couples to a nucleon within the nucleus, and photon-photon interactions, where the photons from the two nuclei interact with each other to produce a pair of oppositely charge muons directly. All three STARlight samples contain a  $\mu^+$  and  $\mu^-$  in the final state. The second class uses PYTHIA6 to decay  $J/\psi$ s produced with a user defined  $p_T$  and rapidity distribution into muon pairs.

Because STARlight is not integrated into the standard CMS software framework (CMSSW), a simulation software chain with 5 steps was developed. First, STARlight is run in the specified mode, and a single file is created for each physics process. In step 2, the STARlight output file is converted to the Les Houches (LHE) format [25], and the momentum of the parent  $J/\psi$  or the initial photon-photon pair is added to the record of each event. The event record produced by STARlight only contains the final state particles. To process the events in parallel, the STARlight files are subdivided in step 2, creating several LHE files from a single STARlight file. The LHE files are used as input to CMSSW.

Steps 3 to 5 take place within CMSSW. In step three the generated particles are propagated through the GEANT4 [26] detector simulation. This accounts for all the interactions with the detector and produces as output a format identical to the raw data that is recorded during data

taking. Steps 4 and 5 are processed using the same software as in data taking. In step 4 the reconstruction software used during data taking is run on the output of the detector simulation. The output of the reconstruction is reduced to the information that is needed for the final analysis in the final step.

The particle gun samples were created entirely within CMSSW.  $J/\psi$  mesons were created according to user defined  $p_T$  and rapidity distributions. PYTHIA6 [27] decays the  $J/\psi$ s to  $\mu^+$  and  $\mu^-$ . As with the STARlight samples, these muons are propagated through the GEANT4 simulation of the detector, and the raw data is produced. The remaining steps of running the reconstruction code and reducing the data to the final data needed for the analysis are identical to the STARlight production.

The momentum of the final state muons is the main drivers of whether the candidate can be measured. One of the two daughters muons must have enough momentum to fire the trigger, and both muons must have enough momentum to be reconstructed and tagged as a muon. There are at least 10 interactions lengths of material through which the muons must travel in order reach the muon chambers (see Fig. 3.11). This imposes an effect momentum threshold on which muons can fire the trigger and be reconstructed.

The  $p_T$  distribution and the polarization of the  $J/\psi$ s produced are the main factors controlling the momentum of the muon daughters, which vary for the different MC samples. The polarization effects how the momentum is shared between the daughters [28]. In the rest frame of the parent  $J/\psi$ , equal momentum is given to each daughter muon. However in the lab frame of the detector, the muon daughters which are emitted from transversely polarized  $J/\psi$  will tend to be emitted in the direction the  $J/\psi$  is traveling and will have unequal momentum in the lab frame. The daughter traveling in the direction of the  $J/\psi$  will have increased momentum, whereas the daughter traveling opposite to the  $J/\psi$  direction will have decreased momentum.

In Fig. 4.1 the  $p_T$  of  $J/\psi$ s from the coherent, incoherent, and photon-photon samples are compared. Both the coherent and the photon-photon samples are concentrated a low  $p_T$ , and neither sample extends much beyond 0.15 GeV. The incoherent sample is peaked near 0.5 GeV and ex-

tends beyond 1 GeV. The two particle gun samples resemble the incoherent and coherent samples  $p_T$  distributions. The first sample has a Gaussian  $p_T$  distribution extending to approximately 0.15 GeV, whereas the second is flat in  $p_T$  up to 2 GeV.

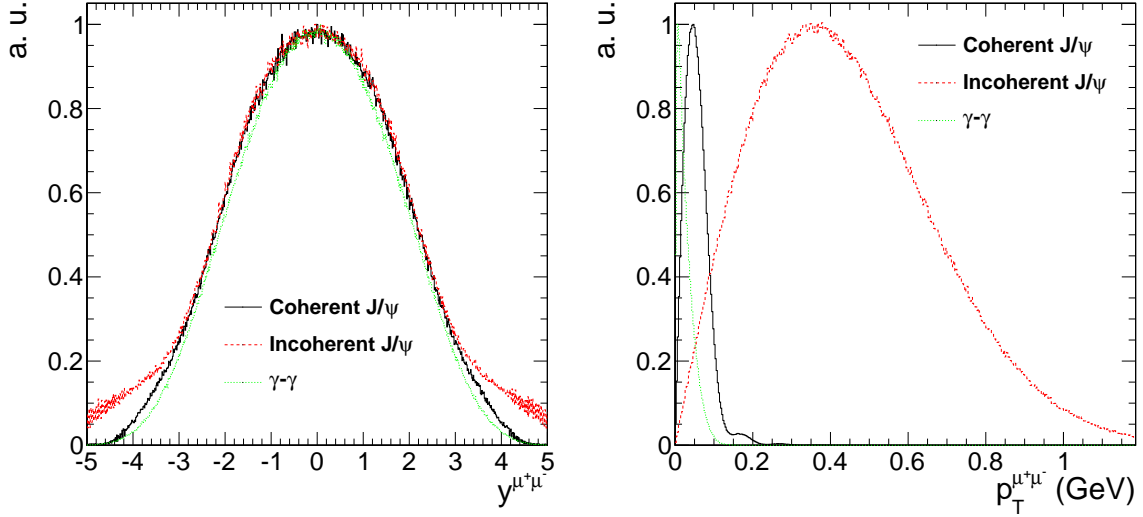


Figure 4.1: Generator level rapidity (left) and  $p_T$  (right) distributions for the coherent (black), incoherent (red), and photon-photon process (green).

The particle gun samples are unpolarized, whereas the STARlight samples have transverse polarization. In Fig. 4.2, the cosine of the helicity angle of the particle gun samples and the STARlight samples are shown. For the STARlight sample the helicity angle, the angle between the direction of the  $\mu^+$  daughter and the  $J/\psi$  direction in the rest frame of the  $J/\psi$ , prefer to be either parallel or anti-parallel. However, the particle gun samples have no preferred direction of emission.

## 4.2 Trigger development

The increase in collision rate of the LHC PbPb beams from 2010 to 2011 was nearly a factor of 15. To accommodate this increase in rate, the 2011 trigger scheme needed to be more selective than in 2010 where CMS could take any event which appeared to have a collision. The available bandwidth was allocated equally amongst the various heavy ion analysis groups to pursue as wide a

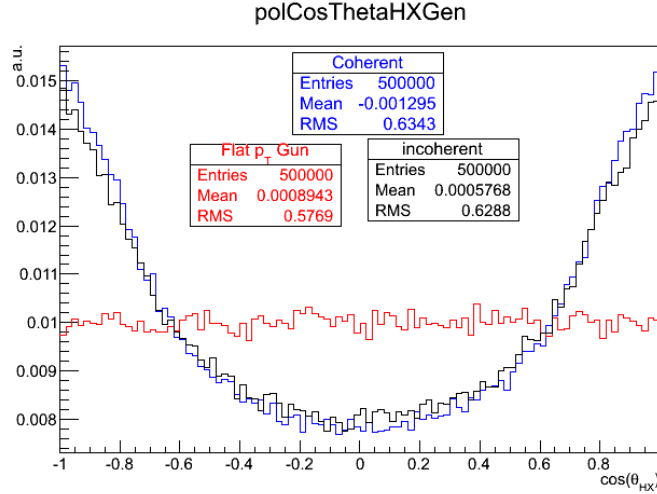


Figure 4.2: The  $J/\psi$  polarization of the particle gun (red), coherent (blue), and incoherent samples are plotted as the cosine of the helicity angle.

physics program as possible. From this consideration, bandwidth limits were placed on the trigger rates for each analysis group's trigger package. To ensure that UPC physics could be explored all while respecting the goals of the CMS Heavy Ions group as a whole, a collection of UPC triggers were commissioned.

The UPC trigger for 2011 were created by combining existing triggers from the 2010 run. By calculating the ratio between the UPC trigger rates and the minimum bias trigger rate, the UPC trigger rates were scaled up to the anticipated 2011 interaction rates using the 2010 data. The trigger package for 2011 contained ZDC based efficiency monitoring triggers, muon and electron based triggers for measuring  $J/\psi$ , and backup triggers in case there was a problem with the original muon and electron triggers.

#### 4.2.1 L1 trigger

The goal of the UPC L1 triggers were to record enough data to measure UPC  $J/\psi$  production via the dimuon and dielectron channels. To achieve this, the loosest muon and electron triggers were paired with a trigger on energy in the ZDC and a veto on energy in the BSCs. Additional triggers that vetoed on energy in HF were commissioned in case radiation damage during the run reduced

the sensitivity of the BSCs. These triggers are summarized in Table 4.1. The 5 and 2 in the ECAL trigger names in Table 4.1 indicate a 5 and 2 GeV threshold on  $E_T$  measured in the ECAL. The Open in the muon trigger indicates that the trigger only requires a muon candidate in one of the three muon sub-systems and that there is not momentum threshold.

L1 trigger	Rate (Hz)	Prescale	Id	Type
MuonOpen and (ZDC <sup>+</sup> or ZDC <sup>-</sup> ) and BSC veto	2.1	1	1	Physics
ECAL2 and (ZDC <sup>+</sup> or ZDC <sup>-</sup> ) and BSC veto	1.8	2	2	
ECAL5 and (ZDC <sup>+</sup> or ZDC <sup>-</sup> ) and BSC veto	0.3	1	3	
(ZDC <sup>+</sup> or ZDC <sup>-</sup> )	35	1500	4	Monitor
MuonOpen and (ZDC <sup>+</sup> or ZDC <sup>-</sup> ) and HF veto	0	off	5	Backup
ECAL2 and (ZDC <sup>+</sup> or ZDC <sup>-</sup> ) and HF veto	0	off	6	
ECAL5 and (ZDC <sup>+</sup> or ZDC <sup>-</sup> ) and HF veto	0	off	7	

Table 4.1: List of 2011 L1 seeds.

The cumulative L1 trigger rate for all the UPC L1 trigger seeds was required to be no greater than 200 Hz. This requirement stemmed from the need to keep the tracker read-out rate low. The trackers baseline voltage can fluctuate due to the high tracker hit multiplicities in PbPb collisions. In order to monitor the zero suppression of the tracker, the zero suppression algorithm was executed using the HLT computing farm rather than in the tracker firmware.

In order to record the efficiency monitoring data, the ZDC triggers had to be prescaled to a lower rate. The scaling down of the monitoring trigger was setup to ensure overlap with the signal triggers. The prescales for the triggers were set to balance the competing objectives of rate reduction and increasing the overlap between the monitoring and signal triggers.

### 4.2.2 HLT trigger

As opposed to the L1 trigger, which has access only to information from calorimeters and muon chambers, the HLT has access to all the sub-detectors including the tracker. Reconstruction of a track in the pixel detector is used by the UPC trigger paths. The use of the pixel detector only, as opposed to using the whole tracker including the silicon strip detector, allows for quick track reconstruction saving computing cycles. The requirement of at least one reconstructed pixel track

for the HLT triggers was designed to reject backgrounds where no particles are reconstructed by the tracker. For the muon trigger in Table 4.2 the rate was reduced by nearly a factor of 4 compared to its L1 seed rate in Table 4.1. This is due to the additional pixel track requirement.

HLT trigger	Rate (Hz)	L1 prescale	HLT prescale	L1 seed	Type
L1UPCMuon and Pixel Track	0.52	1	1	1	Physics
L1UPCECAL2 and Pixel Track	1.65	2	1	2	
L1UPCECAL5 and Pixel Track	0.26	1	1	3	
L1ZDCOr	3.6	1500	11	4	Monitor
L1ZDCOr and Pixel Track	2.8	1500	1	4	
L1UPCMuonHFVeto and Pixel Track	0	off	off	5	Backup
L1UPCECAL2HFVeto and Pixel Track	0	off	off	6	
L1UPCECAL5HFVeto and Pixel Track	0	off	off	7	

Table 4.2: List of 2011 HLT trigger.

The total HLT output for the UPC trigger package was limited to 20 Hz. The limiting factor for the HLT rate was the amount of disk space available to store the data. To meet the bandwidth requirements and collect a significant sample of data for estimating efficiencies, the prescales were balanced with the goal of achieving at least 5% statistical precision on the efficiency estimates. As an example of the balancing of the prescales, the ZDC trigger that was passed through from the L1 was given a additional prescale factor of 11 on the HLT. The ZDC path that also required a pixel track on the HLT, which used the same L1 seed, was only prescaled at the L1. The prescale of 11 was set to ensure that at least 1000 of the pixel track ZDC triggers overlapped with the ZDC L1 only triggers so that efficiency of the pixel track requirement in the trigger could be estimated from the tracks lost.

### 4.3 Event selection

In order to investigate novel physics processes like UPC  $J/\psi$  production, the LHC has delivered unprecedented amounts of data. The data for this analysis was recorded during the 2011 LHC PbPb run. During this period,  $150 \mu b^{-1}$  were recorded by the CMS detector, corresponding to over a billion PbPb collisions. Of this,  $143 \mu b^{-1}$  were used in this analysis.

### 4.3.1 Data sets

Three specially selected samples were used for this analysis, Physics, Monitoring, and Zero bias (see Table 4.3). By recording this hierarchy of samples, interesting events are selected with a much higher purity in the physics sample, while the zero bias and ZDC triggered samples allow for the investigation of the selection criteria. These samples were recorded using subsets of the HLT triggers found in Table 4.2 of Section 4.2. The  $J/\psi$  events discussed in this thesis were obtained analyzing the sample labeled in Table 4.3 as physics. A ZDC triggered monitoring sample was recorded for the sake of estimating efficiencies. Lastly, a zero bias sample was recorded for investigating the ZDC and the noise distributions of HF.

The physics sample containing the  $J/\psi$  signal was recorded by the muon trigger labeled "L1UPCMuon and Pixel Track" in Table 4.2. Because of the characteristically low momentum of UPC  $J/\psi$  as compared to  $J/\psi$  created by other physics processes, the loosest muon trigger was used. The noise trigger rate for the muon trigger alone was 50Hz, but in coincidence with the BCS veto and the ZDC trigger the noise rate was below 2Hz. By pairing the muon trigger with the ZDC on the L1, the noise contribution was reduced from the noise contribution from either of the two sub-detectors to the noise coincidence between the two sub-detectors. Contributions from hadronic interactions are reduced by the veto on the BSCs. This trigger was designed to balance reducing the rate with maximizing the efficiency, allowing for the data to be recorded without producing high rates resulting in dead time for the detector.

In order to investigate the muon trigger and the other parts of the event selection, a monitoring sample was recorded by requiring energy consistent with at least one neutron in either of the ZDCs. This process is much more common than the UPC  $J/\psi$  production. Neutron production has cross sections on the order of 100 b compared to 10 mb predicted from  $J/\psi$  production. For this reason, the rates of this trigger are much higher than the physics trigger, and only a small sub set of these events are recorded. From this trigger the pixel track portion of the HLT trigger efficiency was estimated as well as the ZDC trigger efficiency, as will be described in Section 4.6.

In addition to the monitoring and physics sample, a zero bias sample was recorded to examine

Sample	Events	$\mathcal{L}_{int}$
Physics	346K	$143.3 \mu b^{-1}$
Monitor	1.1M	$31.6 mb^{-1}$
Zero Bias	8.8M	$580 b^{-1}$

Table 4.3: Integrated luminosities and number of events for the three samples used in this analysis.

the ZDC neutron reconstruction and the HF noise distributions. The zero bias trigger fired every time both beams passed through CMS. Only 4 events out of every million triggered were recorded for this sample. This sample allowed for an unbiased measurement of the ZDC neutron threshold energies as discussed in Section 4.4. Because the zero bias trigger does not require any activity in any of the CMS sub detectors, the sample contains very few hadronic collisions. This allowed for a measurement of the electronic noise distribution in the HF, which are important to reducing contamination from hadronic interactions.

The integrated luminosity for each of the three samples is calculated by recording activity in HF [29]. The cross section for HF activity is measured from a van der Meer scan, and the cross section was found to be 45 mb for proton-proton running. In this way, the amount of integrated luminosity for any running period is related to the activity in HF.

### 4.3.2 Event selection cuts

The analysis described in this thesis focuses on UPC  $J/\psi$ s decaying to muons. The trigger used for this analysis recored 346841 events. A set of off-line cuts were applied to increase the relative contribution of UPC events to background processes. Two sets of event selection cuts were applied to reject background events. The first set rejects background from the beam. The second rejects events where hadronic collisions have occurred. Table 4.4 summarizes all the event selection cuts.

To reject beam induced background the following cuts were applied:

- The reconstructed vertex must be within 2 cm in the transverse direction and 25 cm in the longitudinal direction. This cut ensures that reconstructed particles come from interactions between the two beams rather than event where one of the two beams interact with gas



Cut type	Cut	Events
–	all triggered	346841
beam background rejection	good vertex requirement	340997
	beam halo muon rejection	302777
	cluster shape compatibility requirement	233590
hadronic interaction rejection	single-sided neutron requirement	149992
	two track requirement	32732
	HF signal rejection	5392
fake muon rejection	muon quality requirement	2047
kinematic cut	$J/\psi$ mass requirement	696
	muon detectability cuts	567

Table 4.4: Effects of event selection cuts.

particles near the interaction point.

- Beam halo muons were rejected using the timing of the muon hits. The beam halo cut rejects events where muons surrounding the beam stream through the detector.
- Pixel cluster shape should be compatible with the vertex. This cut requires that energy deposits in the silicon tracker point back to the reconstructed primary vertex.

These beam background cuts do not reject any UPC  $J/\psi$  candidates.

The second set of background rejection cuts were designed to reduce contamination from hadronic interactions.

- No more than 2 reconstructed tracks in the event. The track requirement rejects events that produce many charged particles.
- Maximum reconstructed hit energy in HF was required to be below the threshold for electronic noise. Nearly all hadronic interactions (about 98%) produce particles in the range  $3 < |\eta| < 5$  covered by the HF detector. By requiring that the energy deposits in HF resemble noise, nearly all elastic hadronic collisions are expected to be rejected.
- Energy in the ZDCs consistent with neutrons on only one side of the interaction point. In hadronic interactions both nuclei break-up. By requiring that ZDC only reconstruct neutrons

on one side of the interaction point, hadronic interactions that produce neutrons on both sides were rejected.

Each of these cuts were designed to reject topologies produced by hadronic interactions. The effect of these cuts can be seen in Table 4.4 and are denoted hadronic interaction rejection.

To establish the HF noise thresholds, the noise distributions were measured in zero bias events. An offline selection of events with no reconstructed tracks was used to ensure that no collision had taken place. The HF noise threshold was defined as the cut that keeps 99% of the zero bias events. The noise distribution from this zero bias sample is compared to the physics sample and MC in Fig. 4.3.

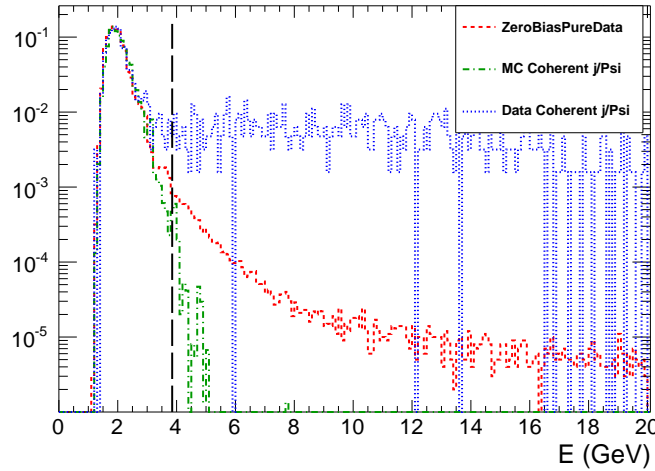


Figure 4.3: Comparison of HF noise distributions in zero bias data, physics triggered data, and MC.

The following standard muon quality cuts are applied:

- Tracker track matched with at least one muon segment (in any station) in both X and Y coordinates ( $< 3 \sigma$ ).
- Cut on number of tracker layers with hits  $> 5$ .
- Number of pixel layers  $> 0$ .
- The  $\chi^2$  per degrees of freedom of the track fit  $< 3$ .

- Loose transverse and longitudinal impact parameter cuts, with in 3 cm in the transverse direction and withing 30 cm in the longitudinal direction with respect to the primary vertex.

These cuts are applied to reduce the number of fake muons and have been validated for standard muon analyses.

## 4.4 Break up determination

As described in Section 2.5, UPC  $J/\psi$  photoproduction can be accompanied by the emission of neutrons from either of the two colliding nuclei. The various neutron emission scenarios, or break-up modes, can be distinguished by the two ZDCs. By separating events where the ZDC signal is consistent with 1 neutron versus several neutrons, or where neutrons are present on only one or both sides, the different break-up modes can be separated and compared to theory.

In order to maximize the ability to explore the one neutron peak, which sits at the bottom of the ZDCs dynamic range, a new ZDC reconstruction method was devised. This new reconstruction method was then used to establish a one neutron and many neutron threshold. This section describes the ZDC signal reconstruction and how the neutron thresholds on this signal were set.

### 4.4.1 ZDC signal reconstruction

The signal from each ZDC is built up from the pulse shapes for each of the 18 individual ZDC channels. The pulse shape is recorded in 250 ns second chunks and is divided into 10 time slices of 25 ns (See Fig 4.4). Counting from 0, the 4th time slice is synced with the timing of the rest of the detector and corresponds to when the products of the recorded collision reached the ZDC. The channel signal is therefore taken from the 4th time slice.

The ZDC signal sits on top of a low frequency noise pedestal with a period of about  $2\mu$  seconds. Over the time scale of 250 ns, this low frequency noise signal appears as a constant that shifts randomly from event to event. The contribution from this noise is therefore measured event by event in order to subtract it. Time slice 5 is used for this purpose. Time slices 1 and 2 could also be

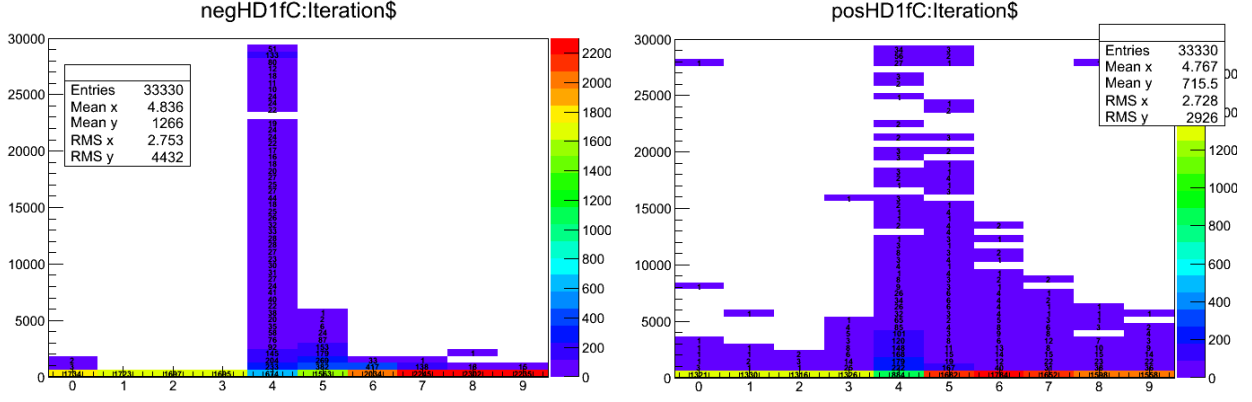


Figure 4.4: Average ZDC pluse shape is plotted as the charge as a function of time slice for the first hadronic from  $ZDC^-$  (left) and  $ZDC^+$  (right).

used to estimate the low frequency noise. However because the noise fluctuates to negative values of charge that cannot be measured, these time slices can only provide a measurement of the noise half the time. By using time slice 5 which contains the falling tail of the signal, the noise can be measured any time the signal raises significantly above the noise. If the fraction of signal in time slice 4 and 5 are constant and the noise contributes the same value to both time slices, the following formula is applicable:

$$Ts4 \propto (Ts4 + C) - (Ts5 + C) = Ts4 - R_{Ts5/Ts4} Ts4 = Ts4(1 - R_{Ts5/Ts4}), \quad (4.1)$$

where  $Ts4$  is the signal contribution in time slice 4,  $Ts5$  is the signal contribution to time slice 5,  $C$  is a random noise constant from the low frequency noise, and  $R_{Ts5/Ts4}$  is the ratio between the signal contribution from time slice 5 over time slice 4. Fig. 4.5 demonstrates the consistence of the fraction and validates the unconventional method of using the falling tail of the signal to estimate the low frequency noise. By using time slice 5, the chances of measuring the noise are maximized. Separating the signal from the noise is especially important because the ZDC signal for the one neutron peak sits near the noise at the bottom of the ZDC dynamic range.

When summing the 9 channels in each ZDC only channels with signals above zero in time slices 4 and 5 were included. The EM section of the calorimeter is more densely packed with

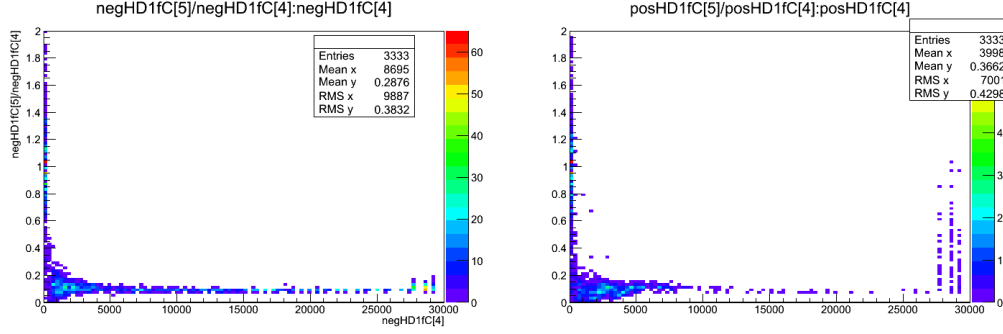


Figure 4.5: The fraction of signal in time slice 5 over time slice 4 as a function of the signal in time slice 5 in  $ZDC^-$  (left) and  $ZDC^+$  (right).

quartz fibers and therefore has a higher gain relative to the HAD section. To account for this, the EM channels were weighted with a factor of 0.1 to match the HAD channel gains.

#### 4.4.2 Determination of the one neutron thresholds

The ZDC thresholds used to establish the various break-up modes were measured from zero bias data. Figure 4.6 shows the weighted sum of the EM and HAD sections for  $ZDC^-$  and  $ZDC^+$  for the zero bias dataset. The neutron spectrum for this dataset does is biased since the trigger only required that both beams were present in CMS. This does, however, include a significant electronic noise contribution due to events where no neutrons are emitted in the direction of the ZDC. It is clear from Fig. 4.6 that the gain of  $ZDC^+$  is lower than that of  $ZDC^-$ . This is because of a damaged phototube on the first HAD section of  $ZDC^+$ .

To determine the thresholds for one and multiple neutrons, the  $ZDC^+$  and  $ZDC^-$  spectra were fit. Four Gaussian functions were combined to fit the spectra. The electronic noise was fit to a Gaussian around zero. The one, two, and three neutron peaks are fit to Gaussians that are successively broader. The mean of each peak was initially set to multiples of the mean of the one neutron peak. The threshold for a neutron in the ZDC was taken from the fits in Fig. 4.6. Any signal greater  $2\sigma$  below the mean of the one neutron peak was considered signal. Any signal greater than  $2\sigma$  above was considered multiple neutrons. The single neutron break up modes were separated from the multiple neutron modes by use of these definitions.

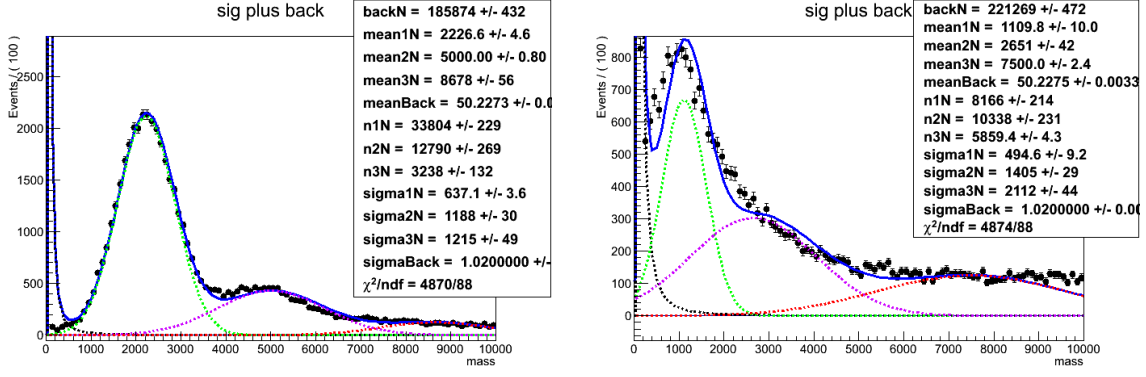


Figure 4.6: Fit to the signal spectra for ZDC<sup>-</sup> (left) and ZDC<sup>+</sup> (right)

Several of the break-up mode calculations that have been done involve single sided configurations where neutrons are present on one side of the interaction point and not the other. These modes can be hard to identify because the single neutron peak in ZDC<sup>+</sup> overlaps with the noise peak at zero. To identify events where the ZDCs only measured noise, the noise spectrum were measured directly. Placing an additional criteria based on the ZDCs noise distributions for when the ZDCs are devoid of signal provides assurance that the events tagged as single sided events are truly single sided.

The noise distributions for the EM sections and the HAD sections were measured separately from out of time time slices. In Fig. 4.4 higher than average signal can be seen in the 0th time slice, which precedes the main signal time slice time slice 4 by 200 ns. This is due to events where activity was present in the ZDC for two consecutive collisions. Time slices 1 and 2, however, occurred between collisions. These time slices, which occur out of time, were used to measure the noise spectrum.

As with the signal measurements, the low frequency noise pedestal is subtracted event by event by subtracting time slice 2 from time slice 1 leaving only the high frequency noise. The noise distributions do not depend on the amount of quartz fibers, but because the signal does, the noise distributions for EM and HAD sections are measured separately. Fig 4.7 shows the noise spectrum for each of the EM and HAD sections for the two ZDCs. If the HAD or EM signals measured from the in time time slices, time slices 4 and 5, are less than  $2\sigma$  above the mean of the noise distribution

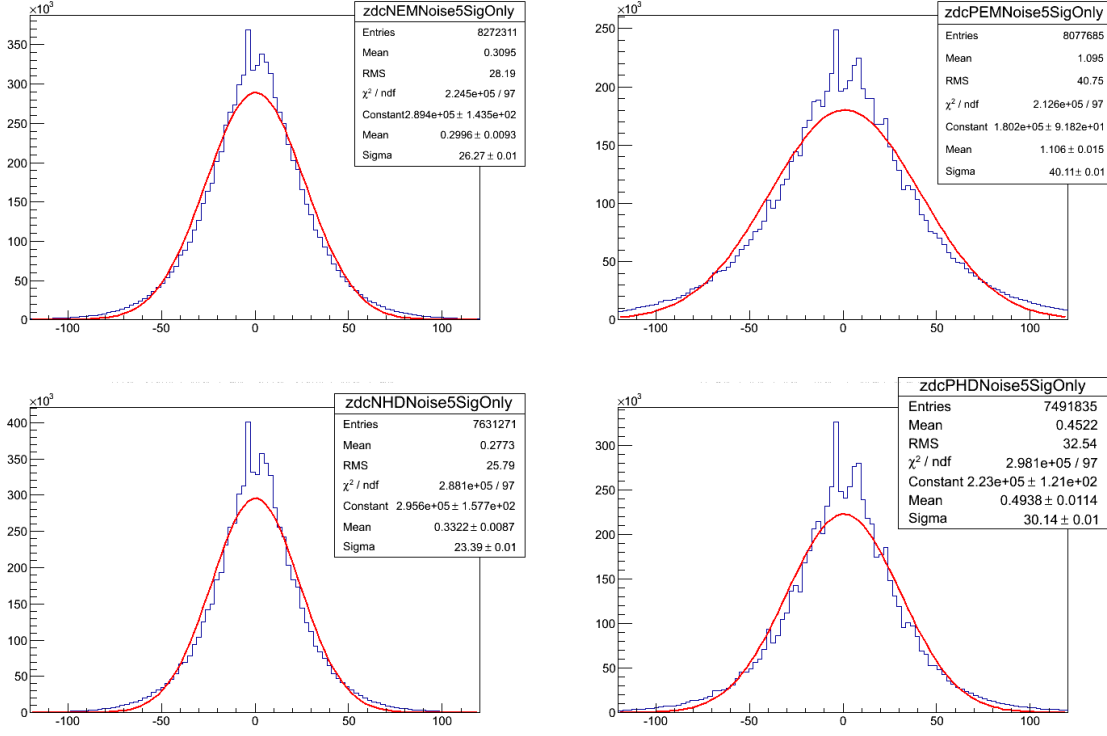


Figure 4.7: ZDC noise spectra from  $ZDC^-$  EM section (upper left),  $ZDC^+$  EM section (upper right),  $ZDC^-$  HAD section (lower left), and  $ZDC^+$  HAD section (lower right) from out of time slices.

or lower, these sections are considered consistent with noise. A ZDC is considered consistent with noise if both the HAD section and EM section from that ZDC have signal measurements consistent with noise.

## 4.5 Signal extraction

After all event selection cuts, the coherent  $J/\psi$ , incoherent  $J/\psi$ , and photon-photon process all contribute to the remaining events. Each process must be separated from the final mix. To achieve this, the invariant mass and  $p_T$  distributions are used to distinguish between the three processes. The photon-photon process is extended in invariant mass whereas the  $J/\psi$  is peak strongly near 3.1 GeV. In  $p_T$  the photon-photon and coherent process have similar distributions, both peaked shapely below 0.1 GeV, whereas the incoherent process is more broadly distributed across an interval ex-

tending to nearly 1 GeV. The mass distribution was fit to separate the photon-photon process from the  $J/\psi$  process. The  $p_T$  distribution was used to separate the incoherent process from the photon-photon process, and the coherent process. In this way, a separate yield was extracted for all three processes.

The invariant mass distribution for opposite sign dimuons is shown in Fig. 4.8. A  $J/\psi$  signal is clearly visible together with tails at higher and lower mass due to the photon-photon process. A fit to the invariant mass distribution was done using a Gaussian to account for the  $J/\psi$  signal and a first order polynomial function for the photon-photon process. The extracted number of  $J/\psi$  candidates from this fit includes all  $J/\psi$ s in the mass window that passed the analysis cuts, i.e. both coherent and incoherent process contribute to yield from the mass fit. The  $p_T$  distribution is needed to separate the two different contributions to the  $J/\psi$  peak.

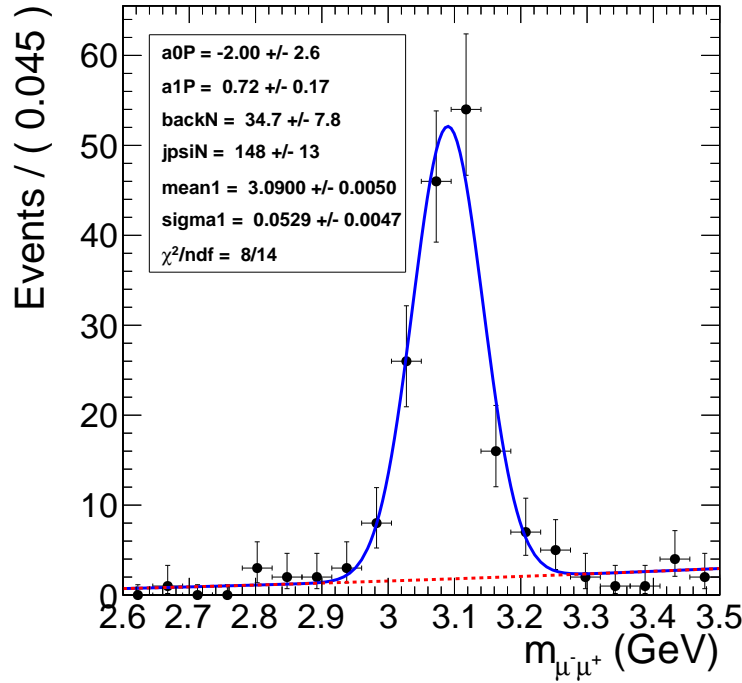


Figure 4.8: Mass fit to  $J/\psi$  using Gaussian for the signal and a first order polynomial for the photon-photon continuum

Figure 4.9 shows the  $p_T$  spectrum of the events plotted in Fig. 4.8. There is a clear coherent peak at  $p_T = 60$  MeV followed by broad distribution that peaks near  $p_T = 450$  MeV. To extract



the contribution of coherent, incoherent and gamma-gamma processes in the data the spectrum in Fig. 4.9 was fit to the sum of three MC templates corresponding to the final output of the MC simulations for these three processes. The clear overlap of the coherent and photon-photon process, and the clear separation of these two lower  $p_T$  processes from the incoherent process is apparent. The shape of the  $p_T$  distribution for the coherent, incoherent, and photon-photon process are taken from the final output of MC after applying all analysis cuts. In Fig.4.9, the yield parameters that were fit were left unconstrained for all three process.

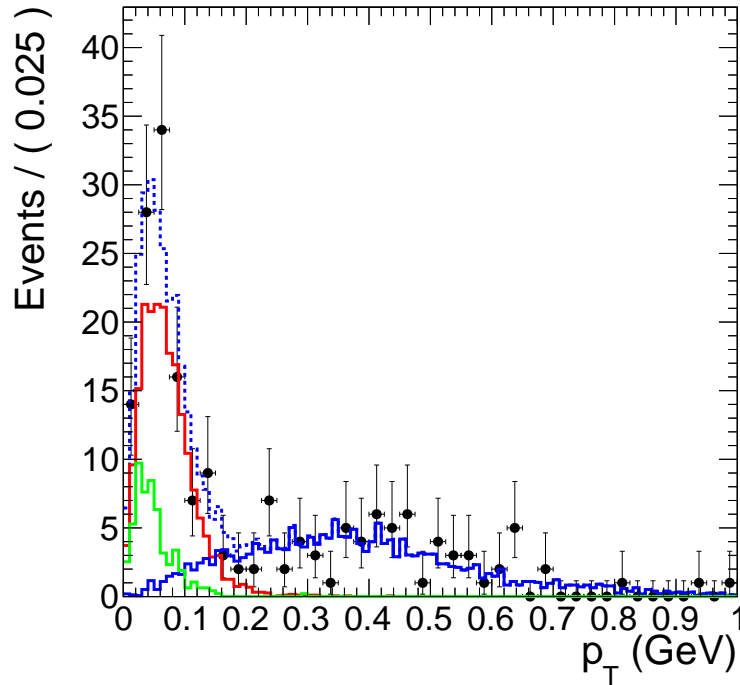


Figure 4.9: Fit to MC  $p_T$  templates.

The shape of the photon-photon and coherent  $J/\psi$  process are very similar in  $p_T$ . Accordingly, the contribution from the photon-photon process and the coherent process are difficult to separate from the  $p_T$  distribution. The confidence contours in Fig. 4.10 from the template fit in Fig. 4.9 demonstrate the strong anti-correlation between the coherent yield parameter,  $nCo$ , and the yield parameter for the photon-photon process,  $nGamma$ . Because of the anti-correlation, the statistical uncertainty on  $nCo$  and  $nGamma$  from the fit are larger than  $\sqrt{nCo}$  and  $\sqrt{nGamma}$  expected from Poisson statistics. The information from the invariant mass and  $p_T$  distributions were combined to

break this correlation. Through this combination, the contribution to the final yield from the three process was measured.

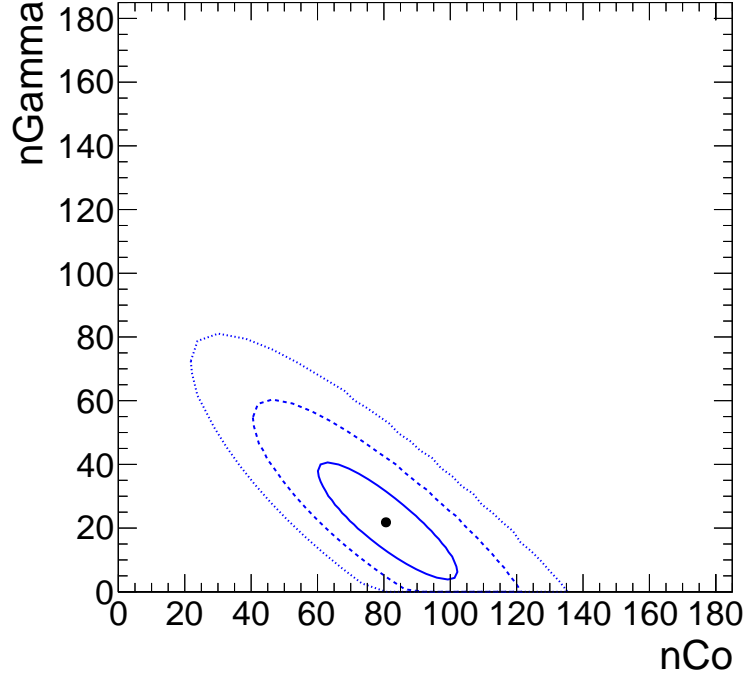


Figure 4.10: 68%, 95%, and 99% confidence contours from the  $p_T$  template fit.

A simultaneous fit to the mass spectrum and  $p_T$  spectrum was preformed to utilize the mass fits ability to distinguish the photon-photon process from the coherent and incoherent process all while utilizing the  $p_T$  fits ability to separate the coherent and photon-photon processes from the incoherent. Fig. 4.11 shows the result of the simultaneous fit. The simultaneous fit forces the parameter  $nGamma$  to both describe the photon-photon continuum present in the side bands of the  $J/\psi$  mass peak as well the photon-photon contribution to the low- $p_T$  part of the  $p_T$  spectrum. In addition, the  $J/\psi$  yield from the mass fit is forced to equal the contribution from the incoherent and coherent process in the fit to the  $p_T$  distribution. In this way, the correlation between the yield parameters was broken, and the contribution from the three process were made independent of each other.

Fig. 4.12 shows the confidence contours for  $nCo$  and  $nGamma$  from the simultaneous fit in Fig. 4.11. The slope of the confidence contours in Fig. 4.12 is noticeably than in Fig. 4.10. The

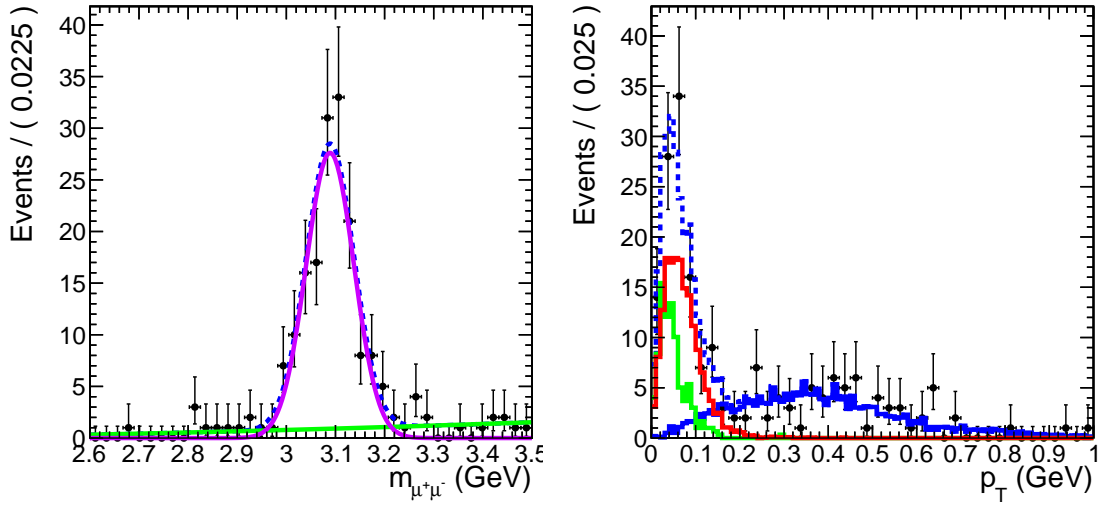


Figure 4.11: Simultaneous fit to the mass and  $p_T$  spectra.

contours for the simultaneous fit are also reduced compared to Fig. 4.10 with widths in  $nCo$  and  $nGamma$  similar to those expected from Poisson statistics. From the simultaneous fit, reasonable statistical errors were obtained along with the yields for the three processes.

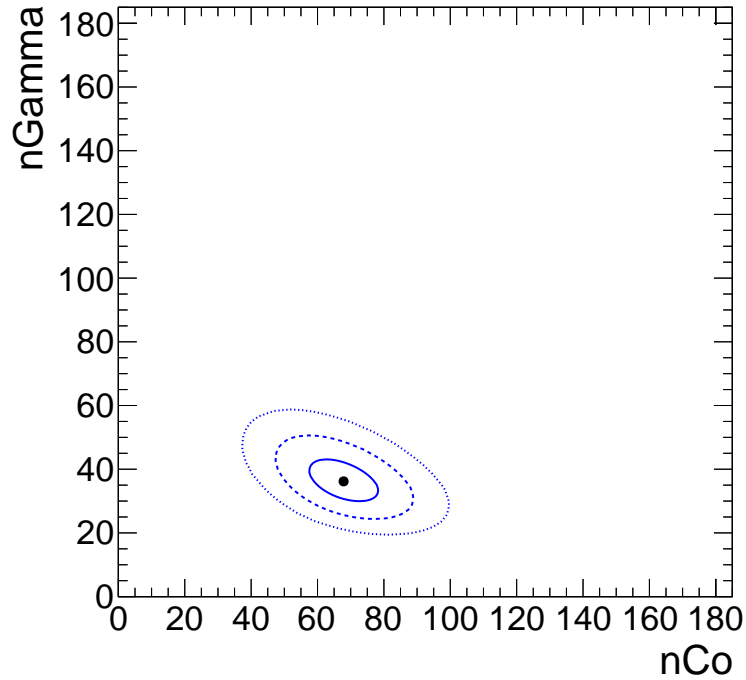


Figure 4.12: 68%, 95%, and 99% confidence contours from the simultaneous fit.

## 4.6 Efficiency determination

Each step of the triggering, event selection, and analysis has an associated efficiency that must be accounted for in the measurement of the  $J/\psi$  cross section. The ZDC trigger efficiency, the muon trigger efficiency, and the muon reconstruction efficiency are the two most significant contributors to the total efficiency measurement. The efficiency of the pixel track requirement, and the veto on activity in the BSCs from the trigger are also estimated but found to be consistent with fully efficient. The following section explains how each of these efficiencies were measured with a special emphasis on the ZDC trigger efficiency and the muon trigger and reconstruction efficiencies.

### 4.6.1 Muon efficiencies

The muon efficiencies were measured using a combination of MC and data based methods. The MC based measurement accounts for the detector acceptance and the efficiency of the muon quality cuts discussed in Section 4.3. The trigger efficiencies were measured in data using the tag and probe method [30], which is discussed below.

CMS has a limited acceptance for  $J/\psi$ s, particularly in the case of  $J/\psi$ s with low momentum like those produced in UPC events. To measure the acceptance of CMS for  $J/\psi$ s, reconstructed dimuon candidates were considered detectable if both reconstructed muon daughters fell into a detectability region in  $p_T$  and  $\eta$ . The muon detectability region was defined using the coherent  $J/\psi$  events obtained from STARlight. The efficiency for reconstructing single muons  $\epsilon_{reco}^\mu$  is defined by  $\epsilon_{reco}^\mu = \frac{N_{reco}^\mu}{N_{gen}^\mu}$ , where  $N_{reco}^\mu$  is the number reconstructed muons obtained after the full CMS detector simulation and that passed the standard muon quality cuts, and  $N_{gen}^\mu$  is the number of generated muons from STARlight. Fig. 4.13 shows the efficiency for reconstructing single muons from coherent  $J/\psi$  events. To avoid the edges of the detectors acceptance, all reconstructed muons that fall into a  $(p_T, |\eta|)$  bin that has an efficiency less than 20% were rejected. This condition defines the detectability region. The acceptance for reconstructing dimuons was calculated from MC using

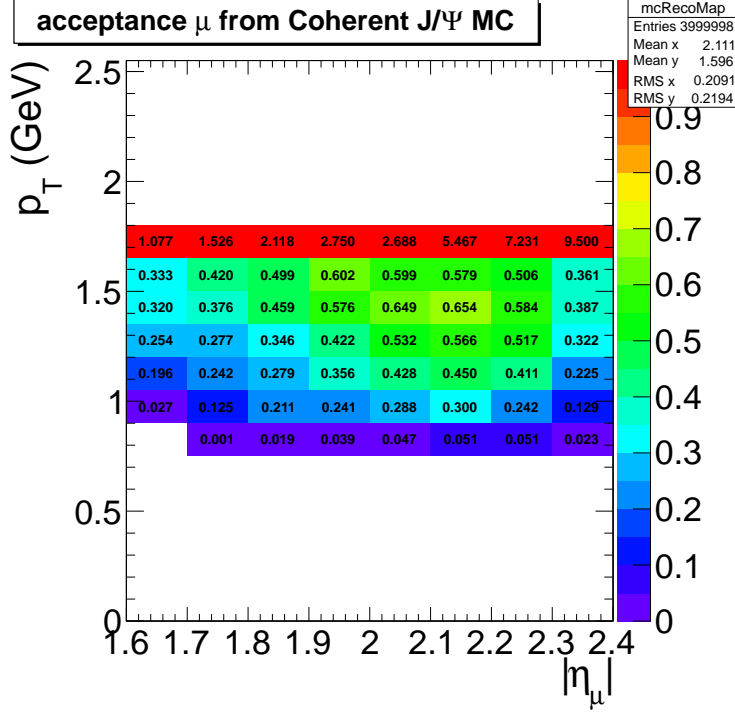


Figure 4.13: Muon daughter detectability from coherent  $J/\psi$  MC

the following formula:

$$A = \frac{N_{det}(|y|, p_T)}{N_{gen}(|y|, p_T)}, \quad (4.2)$$

where  $N_{det}$  is the number of reconstructed dimuons where both daughters fall into the detectability region, and  $N_{gen}$  is the number of generated dimuons. From Eq. 4.2, the acceptance for  $J/\psi$  was calculated as a function of  $|y|$ , and  $p_T$  (see Fig. 4.14).

The tag and probe method is a data driven approach used to measure the trigger efficiency of the muon daughters from  $J/\psi$  decays. In this method there are three categories of daughter muons. *Tag muons* are high quality muons. *Passing probes* are reconstructed muons that match the muon trigger, while *failing probes* do not. Each dimuon will have one daughter classified as a tag and the other as a probe. From here three invariant mass histograms are studied. One histogram is created from all pairs. The second comes from pairs where the probe is a passing probe. The last histogram comes from pairs where the probe fails to fulfill the trigger, *i.e.* the probe is a failing probe. By matching the tag to the trigger, the probe is unbiased by the trigger and the efficiency can be measured by fitting the three mass histograms.

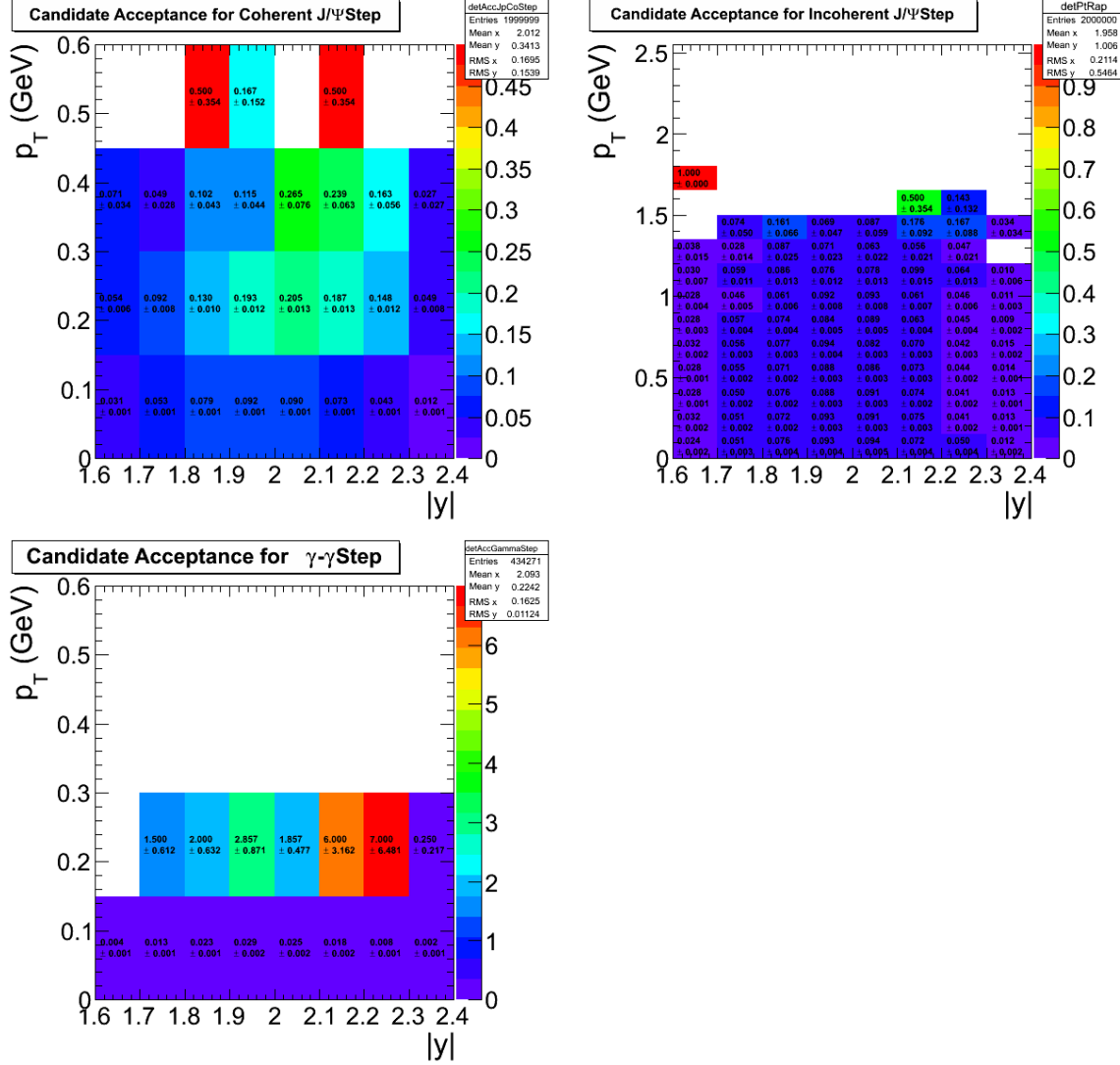


Figure 4.14: Dimuon acceptance from coherent  $J/\psi$  (top left), incoherent  $J/\psi$  (top right), and photon-photon interactions (lower).

Because the trigger efficiency depends on the  $p_T$  and  $|\eta|$  of the muon, one set of three histograms for each  $(p_T, |\eta|)$  bin of the probe is created. To extract the single muon trigger efficiency  $\epsilon_{trig}^\mu$ , each set of invariant mass histograms were simultaneously fit. The signal was fitted using a Crystal Ball function, and the background was fitted to an exponential. The Crystal Ball parameters were simultaneously fitted to all three histograms. The exponential function was fitted to the failing and passing probe histograms separately. Because the background shapes are in principle different for the two samples, the efficiency is driven by this difference.

Fig. 4.15 shows the fit of the three sets of pairs. This fit was done for each bin of the probes  $p_T$

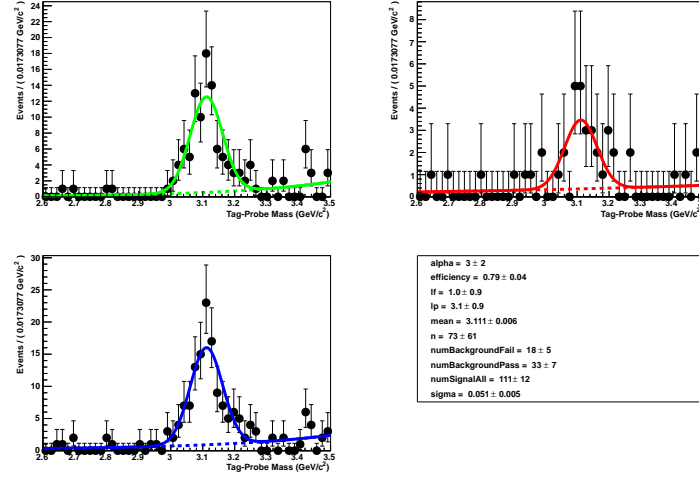


Figure 4.15: Fits to tag and probe pairs in the  $J/\psi$  mass region for pairs with a probe  $2 < |\eta| < 2.2$  and  $1.55 < p_T < 1.8$  GeV.

and  $\eta$ . The efficiency from the fits in each bin are in Fig. 4.16.

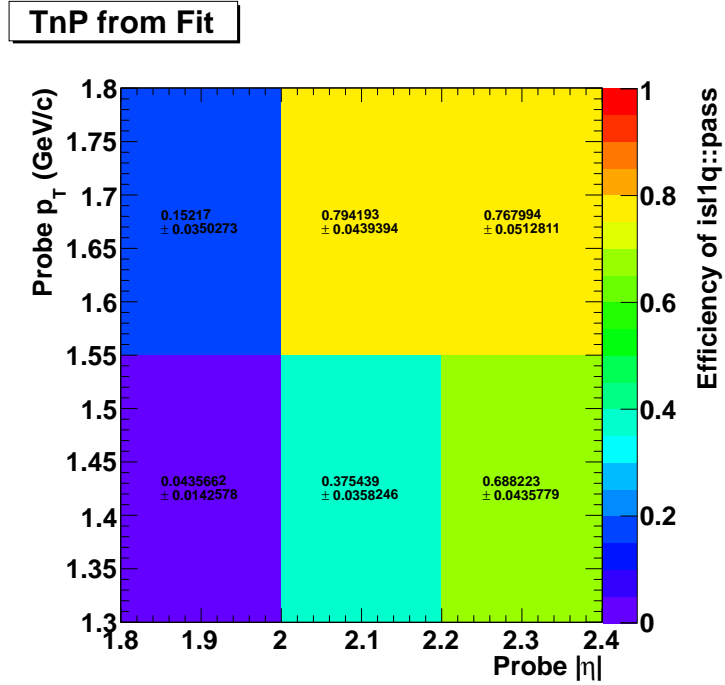


Figure 4.16: Muon trigger efficiencies in  $p_T$  and  $\eta$  bins from the tag and probe method.

The dimuon trigger efficiency  $\epsilon_{trigger}^{dimuon}$  was calculated from the single muon efficiencies using

the following equation:

$$\epsilon_{trigger}^{dimuon} = 1 - (1 - \epsilon_{trigger}^{\mu_1})(1 - \epsilon_{trigger}^{\mu_2}), \quad (4.3)$$

where  $\epsilon_{trigger}^{\mu_1}$  is the tag and probe efficiency of the first dimuon daughter, and  $\epsilon_{trigger}^{\mu_2}$  is the efficiency of the second muon daughter. In Eq. 4.3 the probability of at least one daughter firing the trigger is calculated by subtracting one from the probability that neither daughter fires the trigger, thus giving the dimuon trigger efficiency.

The average dimuon trigger efficiency for each dimuon  $(p_T, |y|)$  bin was calculated by averaging the efficiency of dimuon candidates in each bin. The dimuon trigger efficiency ranges from

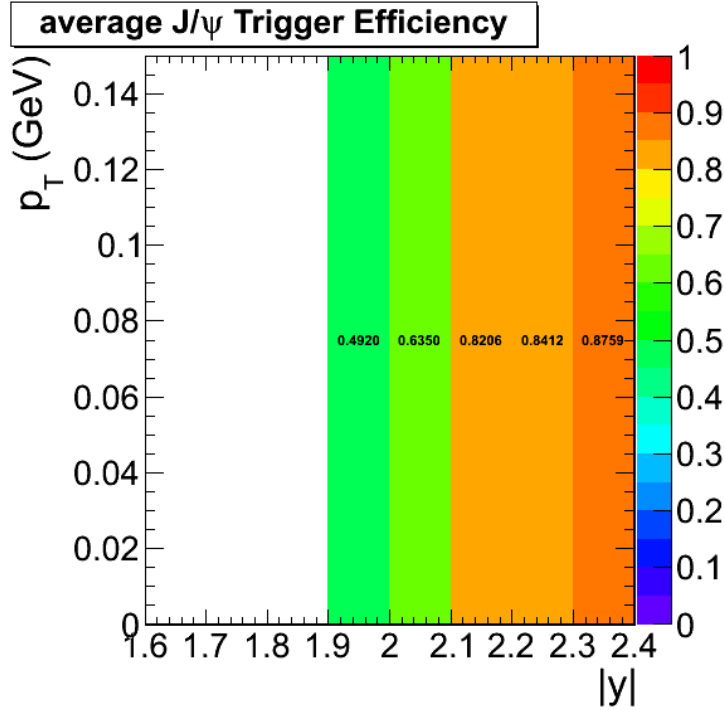


Figure 4.17: The trigger efficiency from tag and probe averaged over candidates in each  $(p_T, |y|)$  bin.

$\approx 50\%$  to  $87\%$ . As expected the  $J/\psi$  trigger efficiency increase with rapidity since the longitudinal momentum of the  $J/\psi$  is given  $p_z = M_{J/\psi} \cdot \sinh(y)$ . Thus  $J/\psi$  mesons at forward rapidity distribute more momentum to their daughter muons which therefore have a greater chance of punching through into the muon chamber. The average trigger efficiency was multiplied by the acceptance and reconstruction efficiency from the MC to produce a total factor for both efficiency



and acceptance.

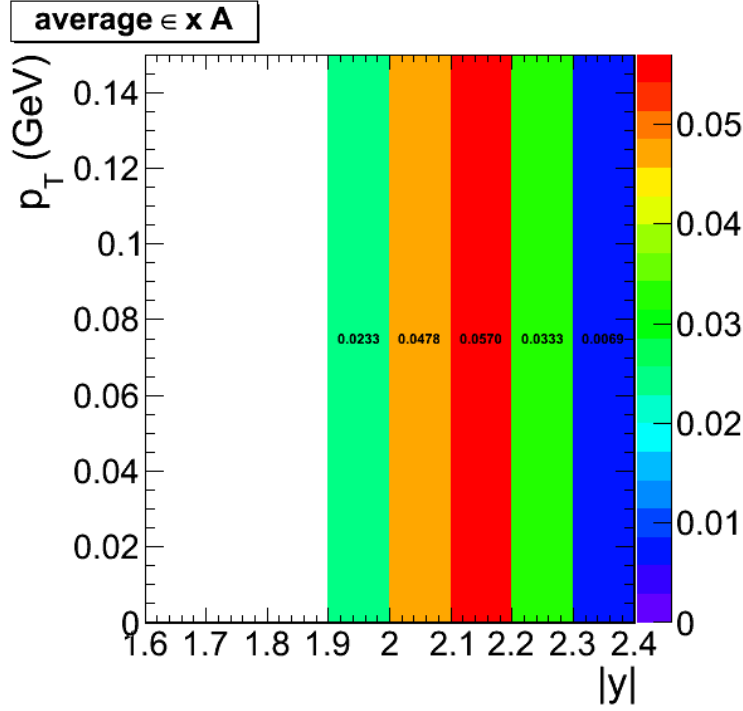


Figure 4.18: The acceptance times averaged trigger efficiency from tag and probe.

The total combined efficiency and acceptance factor coherent  $J/\psi$  between  $2.0 \leq |y| \leq 2.2$  was found to be  $\approx 5\%$ . The acceptance factor of roughly 7% from the MC was found to be the main contributor to the total efficiency. The interplay of the polarization of the  $J/\psi$  and the material in detector drive down the efficiency by creating an effective momentum threshold for detection (see Section 4.1). The reconstruction efficiency of the daughters range between 20%-60% for muons in the defined detectability range. The trigger efficiency for the detectable muons ranges from 30%-80% depending on  $p_T$ .

#### 4.6.2 ZDC trigger efficiency

As discussed in Section 4.4, the trigger labeled "L1ZDCOr and Pixel Track" in Table 4.2 was used to estimate the measure the ZDC trigger efficiency. This trigger required either a  $ZDC^+$  or  $ZDC^-$  trigger, together with at least one pixel track. The veto on the BSC minimum bias trigger, as in the physics triggers, was applied offline. The BSC veto excludes events where BSCs from both

	ZDC Side	Reco Method	$N_{events}$	$N_{trig}$	$\epsilon_{ZDC}$
zo	ZDC <sup>+</sup>	1	72946	71688	$0.982 \pm 0.005$
	ZDC <sup>+</sup>	2	73028	71706	$0.9819 \pm 0.005$
	ZDC <sup>-</sup>	1	76137	71786	$0.9429 \pm 0.005$
	ZDC <sup>-</sup>	2	76132	71859	$0.9439 \pm 0.005$

Table 4.5: ZDC trigger efficiencies for ZDC reconstruction method 1 and 2

sides of the interaction point are above threshold. This trigger was used in order to collect the most inclusive possible sample without using the minimum bias triggers designed to collect hadronic interactions.

This ZDC triggered sample suffers from a trigger bias. For example, a sample triggered by ZDC<sup>+</sup> would always produce a ZDC<sup>+</sup> trigger efficiency of one. To avoid this, a similar technique to tag and probe was used. Each event is either tagged as triggered by ZDC<sup>+</sup> or triggered by the ZDC<sup>-</sup>. The ZDC<sup>+</sup> trigger efficiency is measured from the ZDC<sup>-</sup> tagged sample, and vice versa.

To estimate the efficiency, the number of events with energy in ZDC<sup>+</sup> greater than the single neutron threshold,  $N_{events}$ , were measured. From this set of events, the number of events that also fire the ZDC<sup>+</sup> was measured. The ratio between the number of single neutron events that fired the trigger and all single neutron events was taken as the estimate of trigger efficiency. The same procedure was applied for each side of the ZDC. The trigger efficiency was found to be 98% for ZDC<sup>-</sup> and 94% for ZDC<sup>+</sup>.

## 4.7 Systematic checks

Table 4.6 shows the systematic errors that were estimated. The method used to separate the coherent from the photon-photon process is the most dominant error. The ZDC reconstruction method used to estimate the neutron thresholds is the next most dominant, followed by the method used to estimate the HF noise threshold.

systematic	uncertainty in %
Template fit normalized	+9.5% -12%
ZDC reconstruction	2.9%
ZDC trigger efficiency	2.2%
HF noise threshold	+1.3% -3.4%
MC acceptance	1.1%
Total systematic	8.1%

Table 4.6: Summary of systematic uncertainties

### 4.7.1 HF noise threshold

The way in which the HF noise distribution is measured effects the event selection and therefore the final candidate yeild. This cut plays a significant role in rejecting hadronic events. In Table 4.4 the importance of cutting on HF noise is evident. The HF noise cut rejects a nearly 1/5 of the remaining events. The systematic uncertainties on the HF noise requirement is important for this reason.

The most fine grained data from the HF detectors are called RecHits. Their is one RecHit per phototube on HF. The RecHit signal is calibrated in GeV and no noise subtraction is done. The CaloTowers are formed from geometrical groups of RecHits. They are the first stage of the CMS jet trigger and perform some noise suppression.

The default HF noise cut required that the maximum RecHit energy from both HF+ and HF- be less than 3.85 GeV. This cut was designed to accept 99% of the noise events, see Fig. 4.3. The stability of this cut was tested by

1. Summing CaloTowers instead of RecHits
2. Making separate cuts on HF- and HF+
3. Tightening the threshold so that only 98% or 97% noise events passed the cut.

Table 4.7 shows the noise thresholds for RecHits and CalowTowers for both the combined HF+ and HF- calorimeters and the individual calorimeters when 99% of noise events are accepted.

Table 4.10 compares the threshold for the cases when 99%, 98% and 97% of noise events are accepted. The number of  $J/\psi$  events remaining after these cuts is shown in EXPANDED TABLE. The efficiency corrected numbers are also shown. The fractional systematic error is then estimated by finding the maximum and minimum deviation from the default method. The systematic uncertainty from this method is calculated to be +1.3% -3.4%.

Object type	HF (GeV)	HF <sup>-</sup> (GeV)	HF <sup>+</sup> (GeV)
RecHits	3.85	3.25	3.45
CaloTowers	4.25	3.25	3.75

Table 4.7: HF noise thresholds for various noise measurement methods.

Object type	Combinded HF threshold	Two-sided thresholds
RecHits	298	290
CaloTowers	302	288

Table 4.8: Candidate yields below 1.05 GeV  $p_T$  for various HF noise cuts.

Table 4.9: Values of the energy cuts for the HF calorimeter for RecHit and CaloTower in GeV.

%	$E_{RecHit}$ GeV	$E_{CaloTower}$ GeV
99	3.85	4.25
98	3.25	3.75
97	2.95	3.25

Table 4.10: Number of dimuon candidates with  $p_T < 1.05$  when changing HF calorimeter cuts for RecHit and CaloTower.

%	RecHit cut	CaloTower cut
99	298	302
98	287	294
97	284	280

## 4.7.2 Template fit normalization

The  $p_T$  template fit depends on the functions chosen for the fit to the mass distribution. As described in Section 4.5, the similarity of the  $p_T$  distribution for the coherent and photon-

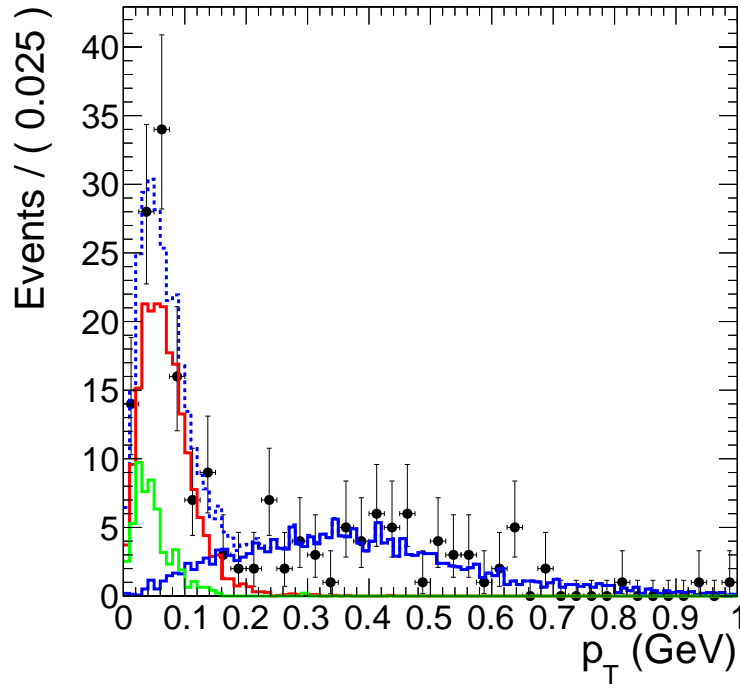


Figure 4.19: Coherent, incoherent, and photon-photon process  $p_T$  template fit to data.

photon process make the contributions from the two process difficult to separate from the  $p_T$  distribution alone. The mass distribution was used to distinguish between these two processes. In turn, the  $p_T$  becomes dependent on the mass fit.

The systematic uncertainty due to the choose of functions used to fit the mass distribution was estimated by varying the signal and background functions. The contribution to the background from the mass fit was used to fix the contribution from the photon-photon process in the  $p_T$  template fit. Two functions were used to describe the signal, a Gaussian, and a Crystal ball function. The background was fit to a linear function, a 2nd order polynomial, and a 2nd order Cheby-Chev polynomial. The resulting variation on the coherent contribution was used to as an estimate of this systematic effect.

Moving from left to right in Fig 4.20, the contribution from the photon process increases. The  $\chi^2$  pre degree of freedom is similar between the three fits indicating a similar goodness of fit. On this basis, neither fit is preferred. The left most fit uses a Crystal Ball function to account for the radiative decay of the final state daughters of the  $J/\psi$ . The low mass exponential portion

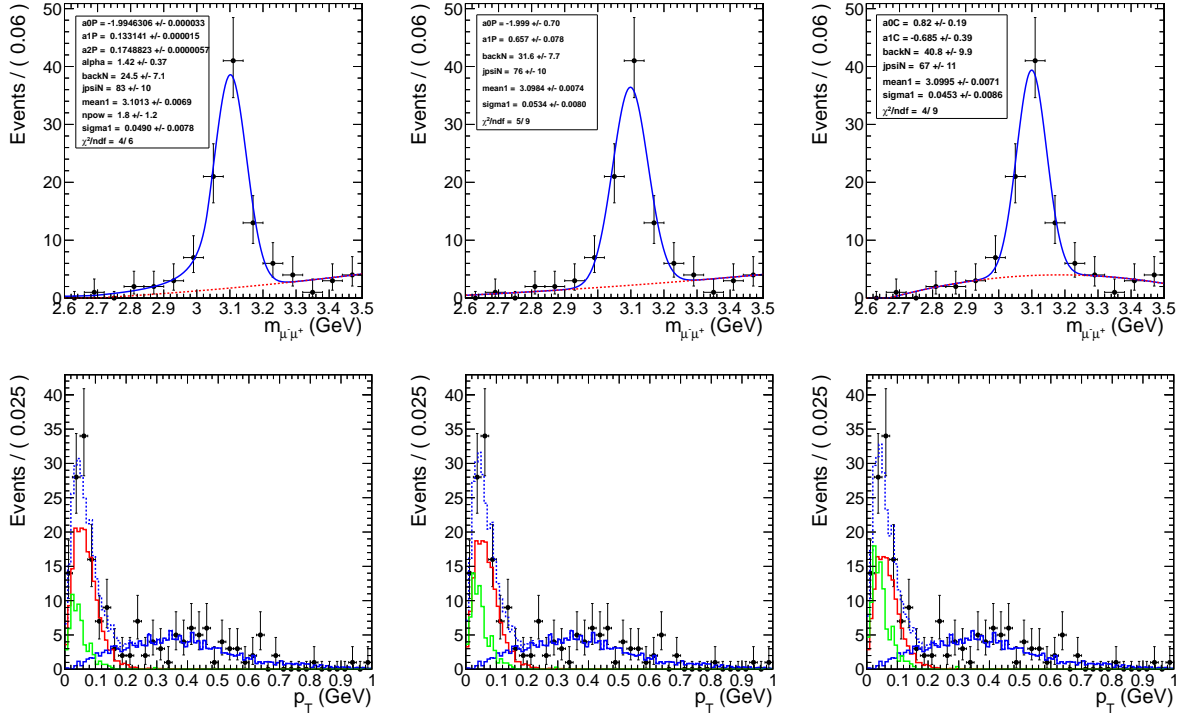


Figure 4.20: Various mass distribution fits and the corresponding  $p_T$  template fit.

however picks up background events and overestimates the  $J/\psi$  contribution. The right most plot fits the background to a 2nd order Cheby-Chev polynomial. Because the Cheby-Chev peaks just below the  $J/\psi$  peak, this fit overestimates the background and in turn underestimates the signal contribution. The Gaussian fit with a linear background however does a reasonable job of fitting both the background and the signal.

From these three fits an upper and lower bound of the systematics due the choice of fit functions was estimated. The difference between the Gaussian-Linear fit and the Crystal Ball-polynomial fit was taken as an upper bound. The difference between the Gaussian-Linear fit and the Gaussian-Cheby-Chev fit was taken as a lower bound. The overall systematic uncertainty due to the choose of mass fit functions is found to be +9.5% -12%.

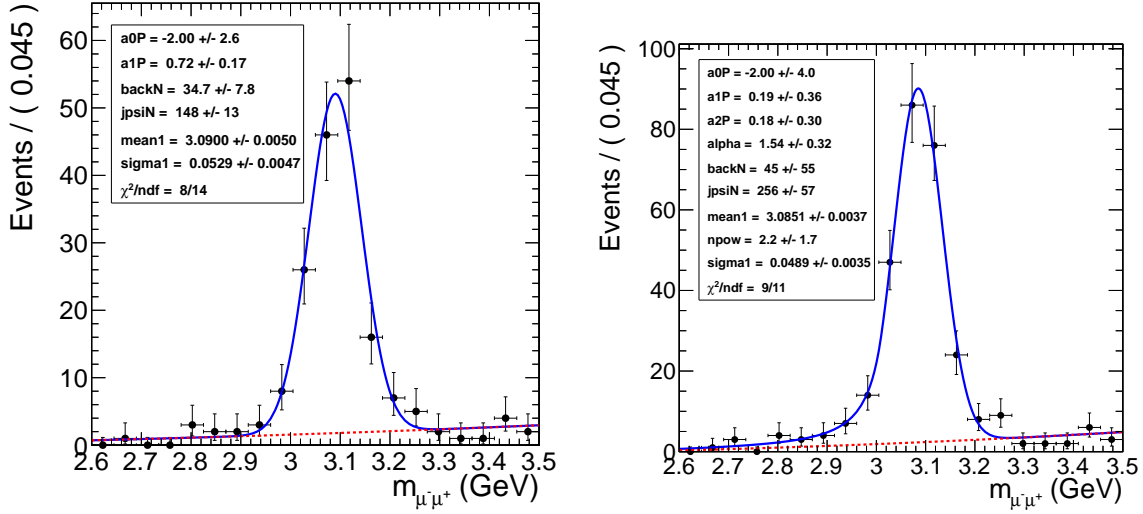


Figure 4.21: Mass fit to  $J/\psi$  using Gaussian (Left) and Crystal Ball (Right) for the signal and a polynomial for the background

### 4.7.3 Mass fit

Fig. 4.21 demonstrates the small dependence the raw  $J/\psi$  yield has on the fitting function. Both fit functions agree well, with reduced  $\chi^2$  values below one. The Crystal ball fit give an upper estimate for the  $J/\psi$  yield. The Gaussian fit gives an lower estimate. The main difference comes from the lower mass tails. In the Crystal ball fit the lower tail is considered to be signal due to shifting of the mass spectrum to lower mass due to radiation from the final state muons. In the Gaussian fit the lower mass tail is considered to be background and the signal is sharper.

As check on the simultaneous  $p_T$  and mass fit, the mass fit is done using mass templates from STARlight.

### 4.7.4 MC acceptance

The MC derived acceptance correction factors depend on the input physics generator. The underlying  $p_T$  distribution was assumed to be correctly described by STARlight for the coherent cross section measurement. To estimate the effect of changing the underlying  $p_T$  distribution on the acceptance measured from the MC, the incoherent sample was used to correct the coherent yield.

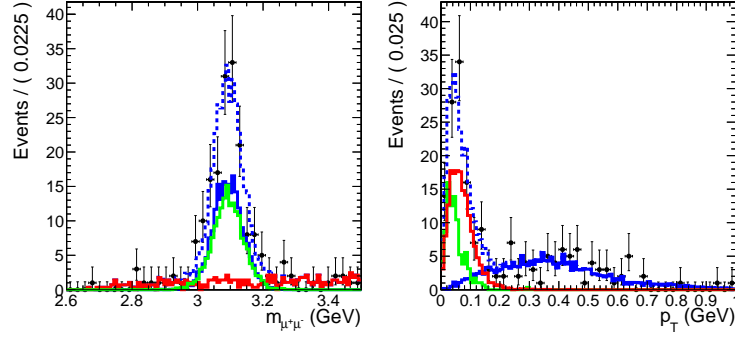


Figure 4.22: Simultaneous fit to the mass and  $p_T$  using mass templates for the mass fit.

By using the broader  $p_T$  distribution of the incoherent process, an estimate of acceptance measurements dependence on the assumed shape of the  $p_T$  distribution was obtained. The systematic uncertainty due to the dependence of the acceptance correction on the  $p_T$  distribution of the input physics generator was estimated by the difference between the correction factors from the coherent and incoherent MC samples. Half the difference was used as the estimate and was found to be 1.1%.

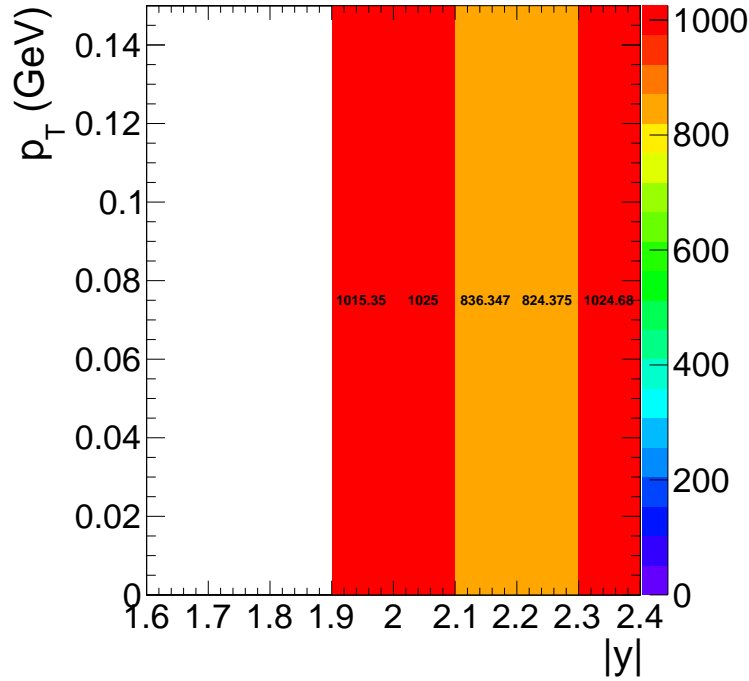


Figure 4.23: Yields corrected by the MC incoherent acceptance map.

The effect of polarization was estimated by correcting by the acceptance for an unpolarized



$J/\psi$  sample.

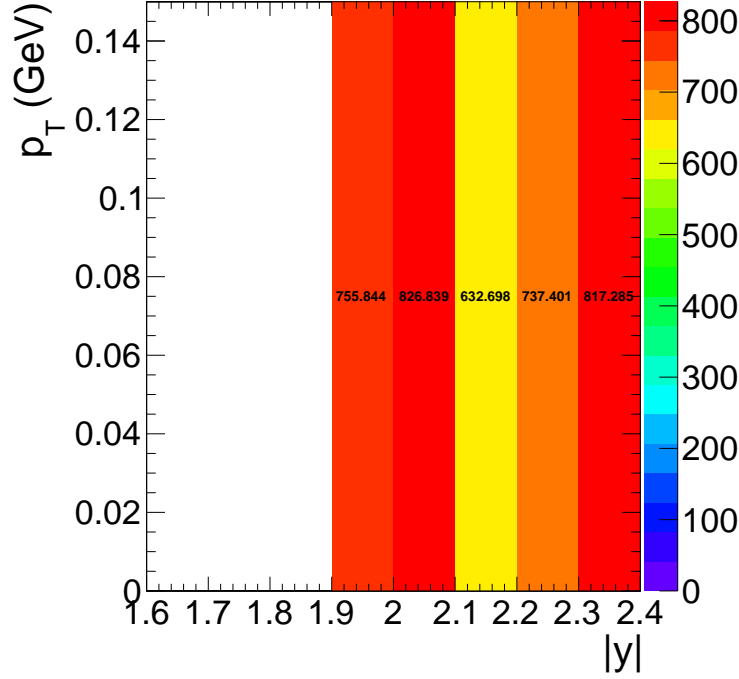


Figure 4.24: Yields corrected by an unpolarized  $J/\psi$  sample.

#### 4.7.5 ZDC reconstruction

An additional method for estimating the ZDC neutron thresholds was used to estimate the systematic errors on the threshold measurements. This additional method, used in previous ZDC measurements, differs in the way the signal time slices are used to calculate the signal from each channel. In the standard method, the signal is taken from the sum of time slices 4, 5, and 6. To estimate the event by event noise pedestal the sum of time slice 1 and 2 are used. The signal for an individual ZDC channel is then calculated as the sum of the signal time slices minus the sum of the noise time slices weighted by a factor of 3/2 to account for the differing number of noise versus signal time slices. The advantage of the standard method is that by using multiple signal and noise time slices the signal and noise are effectively averaged reducing time slice to time slice fluctuations. However, by using time slices 1 and 2 for measuring the noise, the noise can only be measured half the time due to unmeasurable negative fluctuations of the dominant low frequency

component of the noise.

As in the new method described in Section 4.4, the standard method combines the channels to create a signal measurement from the whole of each side of the ZDC, one measurement for  $ZDC^+$ , and one for  $ZDC^-$ . The noise subtracted signal from each of the HAD channels are added together. Then the EM section channels are summed. The EM section is weighted by a factor of 0.1 as in the new method. After the weighting the EM and HAD channels are added to each to create one measurement for  $ZDC^+$  and another measurement for  $ZDC^-$ .

Fig. 4.25 shows the spectra for  $ZDC^+$  and  $ZDC^-$  using the standard method. The same fit used for the new method is applied to standard method. As in the new method, the single neutron threshold is set to  $2\sigma$  below the mean from the fit to the one neutron peak. The multi-neutron threshold was set to  $2\sigma$  above the one neutron peak.

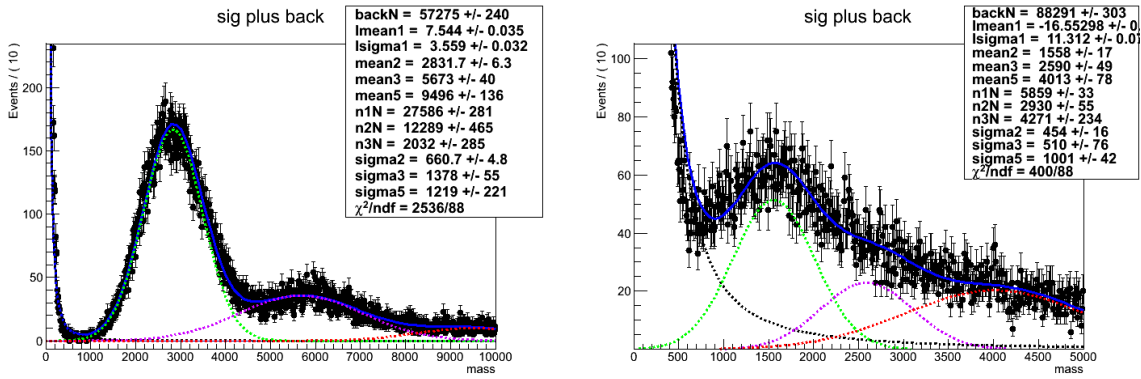


Figure 4.25: Fit to charge spectrum from  $ZDC^-$  (left) and  $ZDC^+$  (right) using the standard reconstruction method

The systematic uncertainty due to the ZDC reconstruction method are estimated from the difference between the UPC  $J/\psi$  candidate yields. Both the reconstruction method and thresholds were changed to calculate the effect of the reconstruction method. The yields for the new and standard ZDC reconstruction method in the  $Xn0n$  break up were found to be 298 and 315 respectively. Half the difference between the two methods was used as an estimated of the systematic uncertainty. The systematic uncertainty due to the ZDC reconstruction method was found to be 2.9%.

### 4.7.6 ZDC trigger efficiency

The ZDC trigger efficiency measurement is sensitive to the underlying neutron distribution. The more neutrons that high the ZDC the higher the trigger efficiency will be. To estimate the effect the input sample has on the efficiency, the ZDC trigger efficiency was measured from five different samples. The Table 4.11 shows the results from the five samples. Both the new and standard ZDC reconstruction methods are shown for comparison.

The amount of electronic noise in the sample also effects the measurement. The more noise sits below the one neutron peak, the worse the efficiency is. In Table 4.11, the Zero Bias sample compared the Zero Bias sample with the timing cuts the described in the previous section shows a significant increase in efficiency in the sample with reduced noise. The same increase is seen when comparing the ZDC triggered sample with the ZDC triggered sample that also requires a pixel track. The effect of the electronic noise is also present in the difference seen in using the two methods. As seen in Fig. 4.26, the new reconstruction method shows better separation of the one neutron peak from the electronic noise, in particular in  $ZDC^+$  where the signal gain is lower. For this reason, the Zero Bias data, which contains that largest contribution from electronic noise, shows the most separation between the two methods and give the lowest estimate for the ZDC trigger efficiency.

The systematic uncertainty due to the uncertainty in the underlying distribution was estimated by calculating the standard deviation of the least extreme values from Table 4.11. Any value greater than three standard deviations from the mean was thrown out.

### 4.7.7 ZDC reconstruction method comparison

The new method relative to the standard method separates low signal from the noise more effectively for both sides of the ZDC. This is particularly important for  $ZDC^+$  where the 1st HAD section had a lower gain than the other sections. The  $ZDC^+$  and  $ZDC^-$  signals near the one neutron peak using the standard and new reconstruction methods were plotted for comparison in Fig. 4.26. In Fig. 4.26, the shrinking of width of the noise peak around zero in the new method versus the old

ZDC Side	Reco Method	$N_{events}$	$N_{trig}$	$\epsilon_{ZDC}$
(ZDC <sup>+</sup> or ZDC <sup>-</sup> ) and 1 pixel track				
ZDC <sup>-</sup>	1	72946	71688	$0.982 \pm 0.005$
ZDC <sup>-</sup>	2	73028	71706	$0.9819 \pm 0.005$
ZDC <sup>+</sup>	1	76137	71786	$0.9429 \pm 0.005$
ZDC <sup>+</sup>	2	76132	71859	$0.9439 \pm 0.005$
(ZDC <sup>-</sup> or ZDC <sup>+</sup> ), 1 pixel track, and L1 EG trigger				
ZDC <sup>-</sup>	1	613758	602123	$0.9810 \pm 0.0018$
ZDC <sup>-</sup>	2	614014	601863	$0.9802 \pm 0.0018$
ZDC <sup>+</sup>	1	643905	602671	$0.9360 \pm 0.0017$
ZDC <sup>+</sup>	2	647888	603089	$0.9309 \pm 0.0017$
(ZDC <sup>-</sup> or ZDC <sup>+</sup> ), 1 pixel track, and L1 Muon trigger				
ZDC <sup>-</sup>	1	65466	63376	$0.9681 \pm 0.0054$
ZDC <sup>-</sup>	2	65543	63358	$0.9667 \pm 0.0054$
ZDC <sup>+</sup>	1	71929	63512	$0.8830 \pm 0.0048$
ZDC <sup>+</sup>	2	72932	63582	$0.8718 \pm 0.0047$
Zero Bias with ZDC timing cuts				
ZDC <sup>-</sup>	1	88676	84429	$0.9521 \pm 0.0046$
ZDC <sup>-</sup>	2	88480	84202	$0.9517 \pm 0.0046$
ZDC <sup>+</sup>	1	59878	54728	$0.9140 \pm 0.0054$
ZDC <sup>+</sup>	2	60467	54733	$0.9052 \pm 0.0053$
(ZDC <sup>-</sup> or ZDC <sup>+</sup> )				
ZDC <sup>-</sup>	1	30986	30333	$0.9789 \pm 0.0079$
ZDC <sup>-</sup>	2	31029	30339	$0.9778 \pm 0.0079$
ZDC <sup>+</sup>	1	39178	30164	$0.7699 \pm 0.0059$
ZDC <sup>+</sup>	2	35703	30443	$0.8527 \pm 0.0067$
Zero Bias				
ZDC <sup>-</sup>	1	109967	101598	$0.9239 \pm 0.0040$
ZDC <sup>-</sup>	2	110230	101561	$0.9214 \pm 0.0040$
ZDC <sup>+</sup>	1	253241	86660	$0.3422 \pm 0.0013$
ZDC <sup>+</sup>	2	156336	87401	$0.5591 \pm 0.0024$

Table 4.11: ZDC trigger efficiencies for ZDC reconstruction method 1 and 2 for different trigger samples

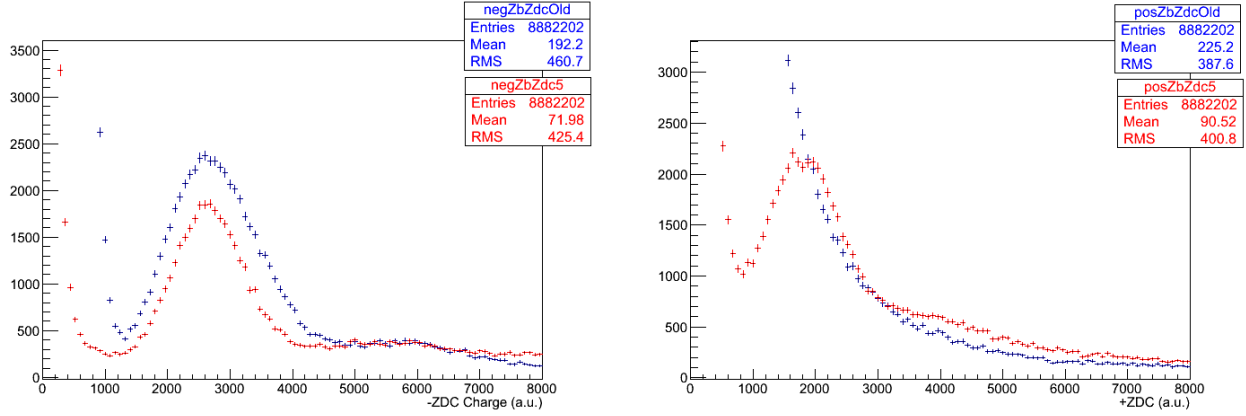


Figure 4.26: Comparison of the **new** ZDC reconstruction method and the **standard** method for  $ZDC^-$  (left) and  $ZDC^+$  (right).

method is apparent for both  $ZDC^+$  and  $ZDC^-$ . For the standard method no single neutron peak is resolved in  $ZDC^+$ , whereas the single neutron peak is resolved using the new method.

Timing cuts were applied to enhance the signal relative to the background in order to resolve the one neutron peak in  $ZDC^+$  using the standard method. Because the products of the collision are synced with time slice 4, noise can be rejected by selecting channels where the maximum signal falls into time slice 4. The noise will have no preferred time slice (see Fig. 4.4). Using this fact, signal can be preferably selected by requiring that the hadronic channels of the ZDC have a peak signal in the fourth time slice. Through these timing cuts the single neutron peak was recovered using the standard reconstruction for  $ZDC^+$ .

To examine the effectiveness of the timing cuts, event by event noise subtraction was removed from the standard reconstruction. The signal from each channel was taken from time slices 4,5, and 6 with out subtracting 1 and 2. The signal spectrum from  $ZDC^-$  was then plotted with the result shown in Fig. 4.27. As each additional hadronic channel is required to have a maximum signal in the fourth time slice, the single neutron peak emerges. Fig. 4.27 demonstrates that the single neutron peak can be recovered from the noise using timing cuts alone.

Using the standard noise subtraction method, the same signal that emerges from the timing cuts alone appear without timing cuts. Fig. 4.28 confirms that both noise subtraction and the timing requirement produce the same signal. This gives confidence that the signal is not an artifact

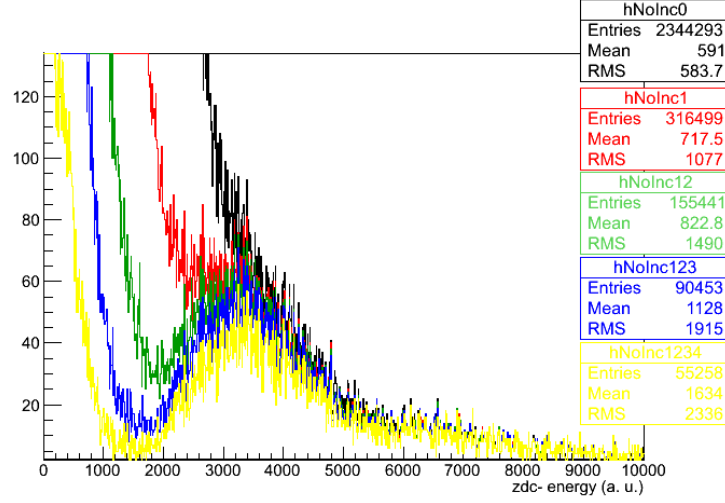


Figure 4.27: Effects of requiring in-time signal in successively more ZDC hadronic channels, no timing, at least **one**, at least **two**, at least **three**, and all **four** HAD channels have a maximum signal in the fourth time slice.

of either cut, but the true neutron signal.

Fig. 4.28 and Fig. 4.26 demonstrate the consistence of the using timing cuts and noise subtraction to enhance the signal neutron peak. Fig. 4.28 confirms the legitimacy of the timing requirement method in  $ZDC^-$  by showing the that the same signal emerges from the noise subtraction method as the timing method. Fig. 4.26 demonstrates the corresponds between the new noise subtraction method and the standard method on in  $ZDC^-$  where signal is better separated from the electronic noise. This allows for confidence that the signal seen in  $ZDC^+$  using the new method is the one neutron peak.

#### 4.7.8 Tag and probe

The main purpose for fitting the mass spectra to estimate the efficiency is to separate the background from true signal. The background may not have the same efficiency as the signal, so separating the two is important if this is the case. In the tag and probe fit the signal peak from the  $J/\psi$  resonance is fit to the probes, passing probes, and failing probes alike (see Fig. 4.15). The signal shape, if from the same physical signal, will be identical in each of the three distributions. The background is for the passing and failing probes is fit using different parameters for

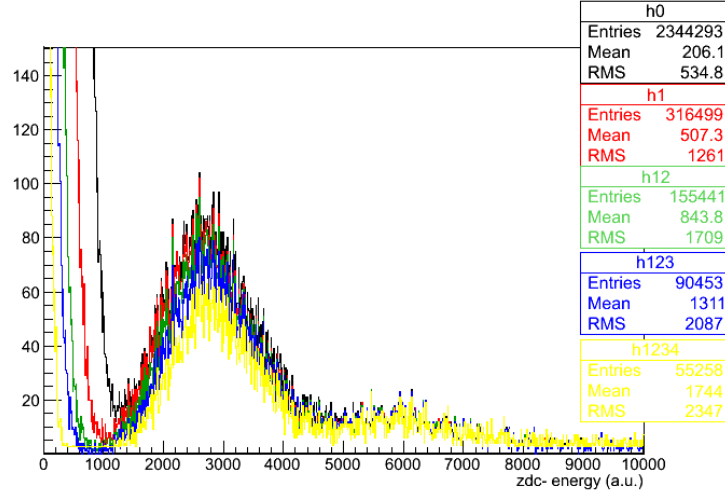


Figure 4.28: Effect of ZDC signal timing requirements after noise subtraction.

the background because the background may come from different physical processes than the signal or non-physical sources like combinatorial backgrounds or misidentified fake particles. When the background comes from sources other than the physical signal, the background may give an efficiency estimate that is lower than the signal.

The trigger efficiency measured by the tag and probe method depend on the fitting functions use to estimate the background and signal contributions. Depending on what functions is used to fit the spectra, the amount of amount of background can be over or underestimated and effect the efficiency measurement. To estimate this effect, the tag and probe efficiencies were additionally measured by counting probes in the  $J/\psi$  mass window. The whole mass window is used to estimate the efficiency including all the events from the mass side bands. In this way, a worst case scenario estimate is given where all background events are included as signal.

From Fig. 4.29 it is apparent that the choice of fit function and therefore the amount of background from the mass side bands is included in the signal measurement has very little effect on the tag and probe efficiency measurement. The small effect of including the side bands is due to the side bands being comprised mostly of photon-photon events. Because this background is neither decays from other particles like pions nor is it non-physical background like combinatorics, the efficiency for muons from the sidebands are nearly identical to  $J/\psi$  signal. The photon-photon

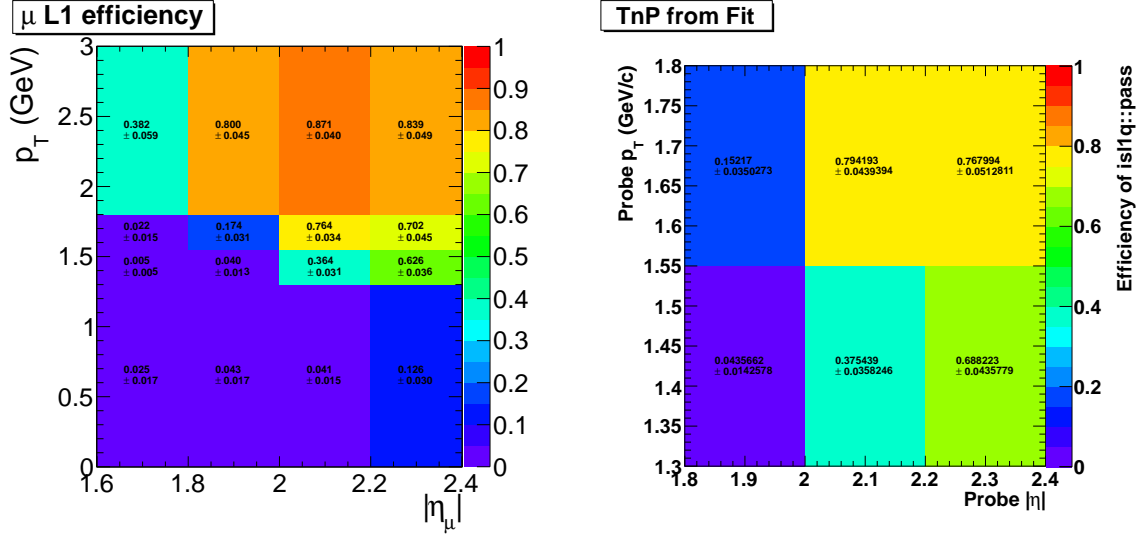


Figure 4.29: Tag and probe trigger efficiencies from counting (left) compared to fitting (right)

process directly produces two muons just like the  $J/\psi$ , therefore efficiency estimated from the side bands has little effect on the measurement because of this similarity. The counting and fitting trigger efficiency measurements agree within statistical uncertainties, so this uncertainty was taken to be negligible.

#### 4.7.9 MC vs Data compairson



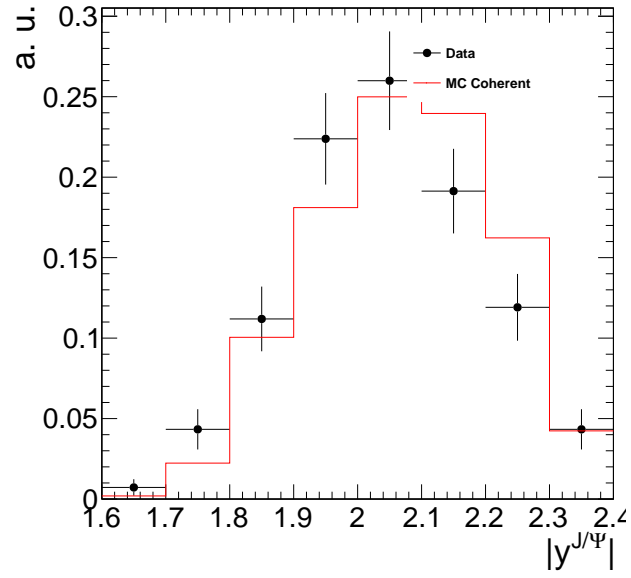


Figure 4.30: Comparison of the of the dimuon rapidity distributions between coherent MC sample and Data.

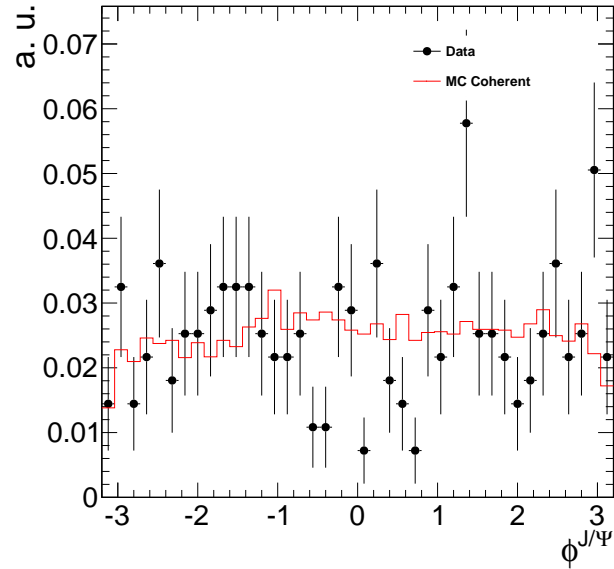


Figure 4.31: Comparison of the of the dimuon  $\phi$  distributions between coherent MC sample and Data.

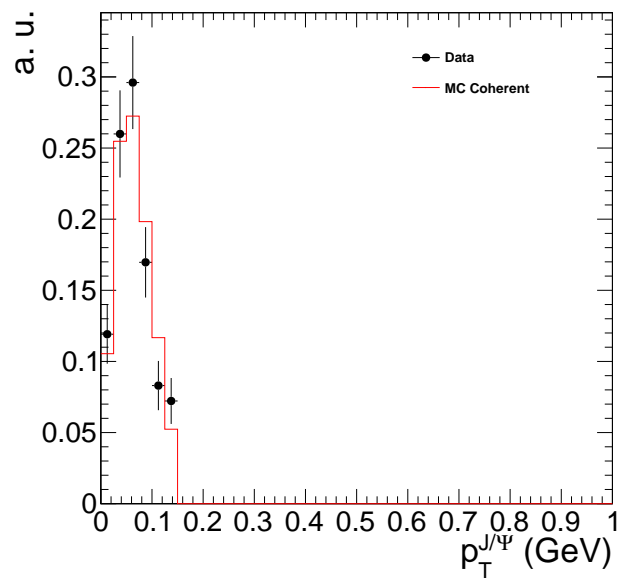


Figure 4.32: Comparison of the of the dimuon  $p_T$  distributions between coherent MC sample and Data.

# Chapter 5

## Results

The main results of this thesis are give here: the cross section for coherent  $J/\psi$  production, the incoherent  $J/\psi$  cross section, the cross section for muon pairs from photon-photon interactions, the ratio between break up mode yields, and the rapidity correlations between dimuon candidates and neutrons in the ZDC.

### 5.1 Coherent cross section

The coherent cross section in calculated from the following equation:

$$\frac{d\sigma_{co}^{J/\psi}}{dy} = \frac{N_{cor} f_{co}}{\Delta y \mathcal{L}_{int} \epsilon_{ZDC} \epsilon_{p_T} BR_{\mu^+\mu^-}} \quad (5.1)$$

where  $N_{cor}$  is corrected dimuon yield,  $f_{co}$  is the fraction of events that come from the coherent process,  $BR_{\mu^+\mu^-}$  is the branching ratio for  $J/\psi$  to  $\mu^+\mu^-$ ,  $\epsilon_{ZDC}$  is the efficiency for triggering the ZDC,  $\epsilon_{p_T}$  is the efficiency for the 0.15 GeV cut in  $p_T$ ,  $\mathcal{L}_{int}$  is the integrated luminosity, and  $\Delta y$  is the width the rapidity interval.

The raw yield of dimuon candidates was measured after applying the cuts described in Section 4.3.  $N_{cor}$  was calculated by dividing the raw yields from Fig. 5.1 by the acceptance and efficiency factor from Fig. 4.18, which combines  $A$  and  $\epsilon_{trigger}^{dimuon}$  as described in Section. 4.6. The

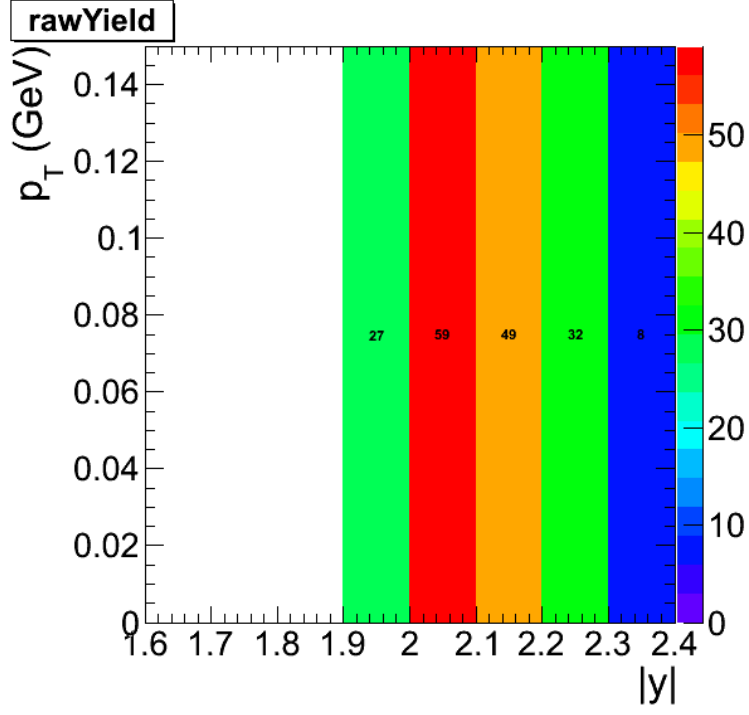


Figure 5.1: Raw yield for the Coherent cross section measurement.

corrected yields,  $N_{cor}$ , are shown in Fig. 5.2. For the coherent cross section measurement,  $N_{cor}$

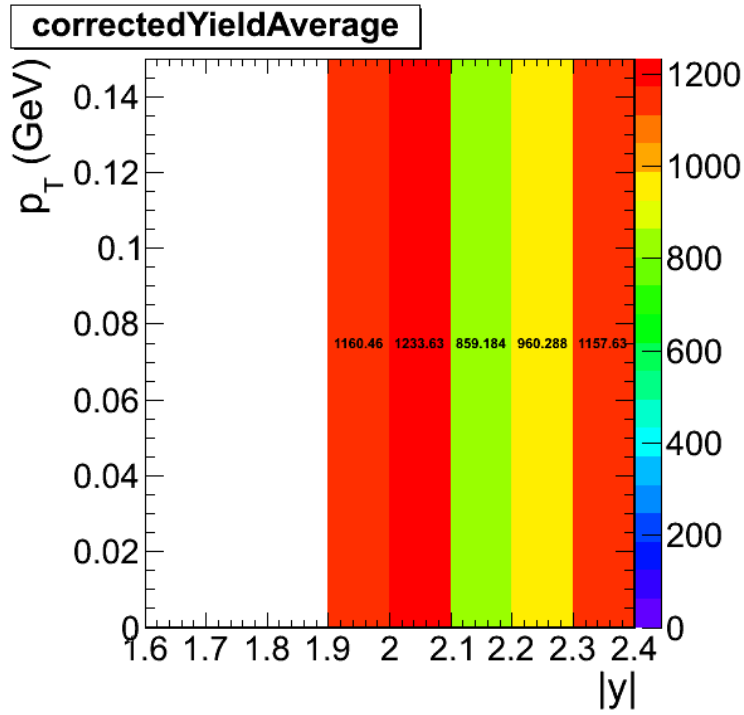


Figure 5.2: Corrected yields for the coherent  $p_T$  region.

is taken from the region  $2.0 < |y| < 2.2$  and  $p_T < 0.15$  GeV to avoid the edges of the detectors acceptance, bin migration in the calculation of  $A$ , and overlap between the coherent and incoherent process. From this procedure, the  $N_{cor}$  was measured to be 1903.

To measure  $f_{co}$ , the simultaneous fit shown in Fig. 4.11 was used. The normalizations for each of the three components to the signal are fixed by the fit as described in Section 4.5. The normalized coherent template is integrated up to 0.15 GeV in  $p_T$  and divided by the integral of the data  $p_T$  spectrum up to 0.15 GeV. The statistical error taken from the fit,  $f_{co} = 0.60 \pm 0.11$ .

The two efficiency terms,  $\epsilon_{ZDC}$  and  $\epsilon_{p_T}$ , were measured from data and MC respectively. As described in Section 4.4,  $\epsilon_{ZDC}$  was measured in the from the ZDC triggered data set by dividing the number of events both fire the ZDC trigger and pass the one neutron threshold.  $\epsilon_{ZDC}$  was measured to be 0.96 with a negligible statistical error. The efficiency of the 0.15 GeV  $p_T$  cut was estimated from MC by dividing the number of events that are lost by applying the  $p_T$  cut after all other cuts are applied. From this method  $\epsilon_{p_T} = 0.95$ .

The remaining two terms,  $\mathcal{L}_{int}$  and  $BR_{\mu^+\mu^-}$ , depend on Ref. [29] and Ref. [31]. Ref. [29] describes the method of using activity in HF to measure the luminosity. From this method,  $\mathcal{L}_{int}$  was measured to be  $143.3 \mu b^{-1} \pm 7.2$ .  $BR_{\mu^+\mu^-}$  from Ref. [31] is  $0.0593 \pm 0.0006$ . From Equation 5.1,  $\frac{d\sigma_{co}^{J/\psi}}{dy} = 368 \mu b$ .

## 5.2 Incoherent cross section

The same basic procedure for measuring the coherent cross section was used to calculate the incoherent cross section.

## 5.3 Break up ratios

In Table 5.2 the ratio between raw yields for different break up modes are shown.

Fig. 5.3 and Fig. 5.4 compare the raw break up ratios two STARlight and LTA predictions.

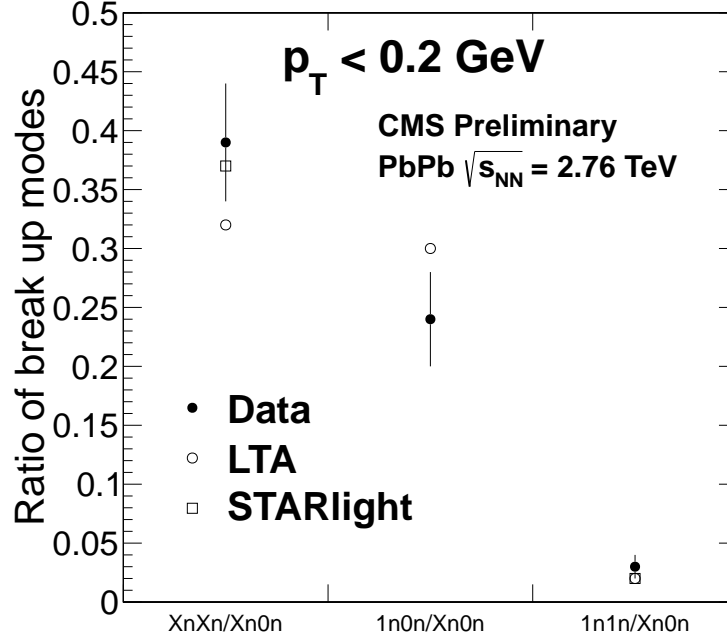


Figure 5.3: Ratio between  $J/\psi$  yeilds  $X_n X_n$  and  $1_n 0_n$  break-up modes compared the  $X_n 0_n$  break-up mode for  $J/\psi$  with  $p_T$  below 150 MeV.

The number of the coherent and incoherent  $J/\psi$  for each break-up mode are given in the Tab. 5.1. The ratios between the modes  $X_n X_n$ ,  $1_n 0_n$ ,  $1_n 1_n$  and the mode  $X_n 0_n$  are given in the table Tab. 5.2. Some of the ratios can be obtained from STARLIGHT and from the Zhalov and thus are given in Tab. 5.3.

	$X_n 0_n$	$X_n X_n$	$1_n 0_n$	$1_n 1_n$
coherent $J/\psi$	$242 \pm 16$	$94 \pm 10$	$58 \pm 8$	$8 \pm 3$
incoherent $J/\psi$	$291 \pm 17$	$57 \pm 8$	$19 \pm 4$	$2 \pm 1$

Table 5.1: Number of coherent  $J/\psi$  integrated over  $p_T$  and  $y$  with statistical uncertainty.

In Table 5.3 the ratio between break up modes are shown for different theories and processes.

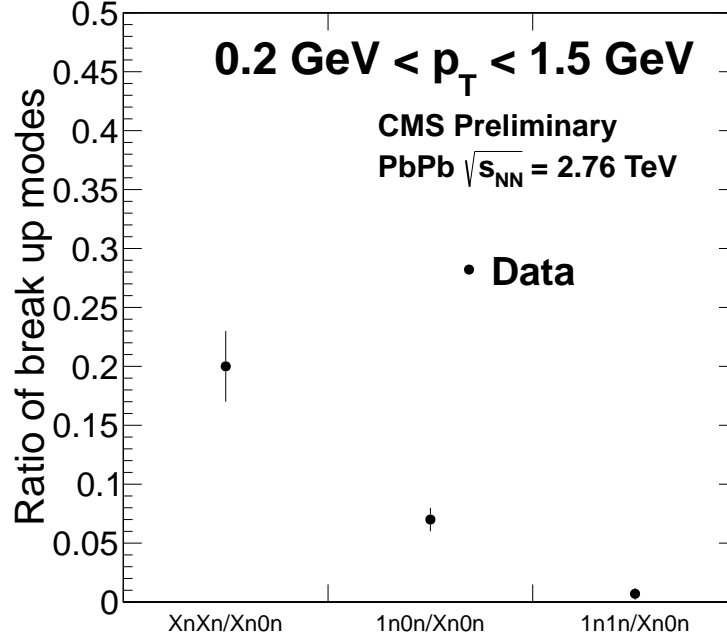


Figure 5.4: Ratio between  $J/\psi$  yeilds  $X_n X_n$  and  $1_n 0_n$  break-up modes compared the  $X_n 0_n$  break-up mode for  $J/\psi$  with  $0.2 < p_T < 1.5$  GeV.

	$X_n X_n / X_n 0_n$	$1_n 0_n / X_n 0_n$	$1_n 1_n / X_n 0_n$
coherent $J/\psi$	$0.39 \pm 0.05$	$0.24 \pm 0.04$	$0.03 \pm 0.01$
incoherent $J/\psi$	$0.20 \pm 0.03$	$0.07 \pm 0.02$	$0.007 \pm 0.005$

Table 5.2: Number of coherent  $J/\psi$  integrated over  $p_T$  and  $y$  with statistical uncertainty.

## 5.4 diMuon-neutron correlations

In this section the correlation between the rapidity of the  $\mu^+ \mu^-$  and of the neutron is studied. The following samples are studied:

- $\gamma + A$  collisions in which two cases are considered
  - elastic coherent interaction: here photon interacts with entier nucleus coherently and produce  $J/\psi$ . Another photon is needed to cause the breakup and neutron emission. Those two photons are uncorrelated and thus we don't expect to observe the correlation between the rapidity of the neutron and the rapidity of the  $J/\psi$ . In the data sample this

	$X_n X_n / X_n 0_n$	$1_n 0_n / X_n 0_n$	$1_n 1_n / X_n 0_n$
STARlight coherent	0.37	-	0.02
Zhalov coherent	0.32	0.30	0.02
STARlight incoherent	0.37	-	$0.007 \pm 0.02$

Table 5.3: Number of  $J/\psi$  integrated over  $p_T$  and  $y$  with statistical uncertainty.

corresponds to the low- $p_T J/\psi$  ( $p_T < 0.15$  GeV).

- inelastic incoherent interaction: here a single high  $p_T$  photon interacting with nucleus produce the  $J/\psi$  and neutron. The correlation between the rapidity of the neutron and the rapidity of the  $J/\psi$  is expected. In the data sample this corresponds to the high- $p_T J/\psi$  ( $0.15 < p_T < 1.05$ ).
- $\gamma\gamma$  collisions: two photons collide and produce the  $\mu^+ \mu^-$  and the third photon is needed to excite one of the nucleons and produce neutron. Thus we don't expect to see the correlation between the rapidity of the neutron and the rapidity of the  $\mu^+ \mu^-$ . In the data sample this corresponds to the  $\mu^+ \mu^-$  with the invariant mass between 4 and 8 GeV.

In order to study the correlation in rapidity between the neutron and dimuon direction we below four quantities and give they values in Table 5.4.

- $y_{\mu\mu}^- \wedge y_n^-$ : number of  $\mu^+ \mu^-$  having  $y < 0$  and the neutron in  $ZDC^-$  ( $y < 0$ )
- $y_{\mu\mu}^- \wedge y_n^+$ : number of  $\mu^+ \mu^-$  having  $y < 0$  and the neutron in  $ZDC^+$  ( $y > 0$ )
- $y_{\mu\mu}^+ \wedge y_n^+$ : number of  $\mu^+ \mu^-$  having  $y > 0$  and the neutron in  $ZDC^+$  ( $y > 0$ )
- $y_{\mu\mu}^+ \wedge y_n^-$ : number of  $\mu^+ \mu^-$  having  $y > 0$  and the neutron in  $ZDC^-$  ( $y < 0$ )

The ratio  $R_{opp/same}$  is defined as:

$$R_{opp/same} = \frac{y_{\mu\mu}^- \wedge y_n^+ + y_{\mu\mu}^+ \wedge y_n^-}{y_{\mu\mu}^- \wedge y_n^- + y_{\mu\mu}^+ \wedge y_n^+} \quad (5.2)$$



Ratios studied in this section are only sensitive to the difference between the  $ZDC^-$  and  $ZDC^+$ . It is seen that the efficiency of both ZDCs is not exactly the same i.e. the efficiencies of  $ZDC^-$  and  $ZDC^+$  are respectively  $\epsilon_{ZDC^-}=0.98$  and  $\epsilon_{ZDC^+}=0.94$  and this is taken into account in the estimations. The  $R_{opp/same}$  ratio corrected by the ZDCs efficiencies is also included in Table 5.4 and called  $R_{opp/same}^{\epsilon_{ZDC}}$ . It is seen that the difference between corrected and uncorrected results is very small. Other uncertainties cancel. In this case cuts related to the acceptance and efficiencies corrections are not necessary and thus they are released.

Figure 5.5 gives  $p_T$  distributions of the  $J/\psi$  when  $J/\psi$  and neutron have the opposite rapidity direction or when they have the same rapidity direction for low- $p_T$  and high- $p_T$   $J/\psi$ . Also the Fig 5.5 gives the  $R_{opp/same}$  for low- $p_T$  and high- $p_T$   $J/\psi$ . It is seen from this plot that in the case of the low- $p_T$   $J/\psi$  this  $R_{opp/same}$  ratio is close to 1 and is decreasing when the  $p_T$  of  $J/\psi$  increases.

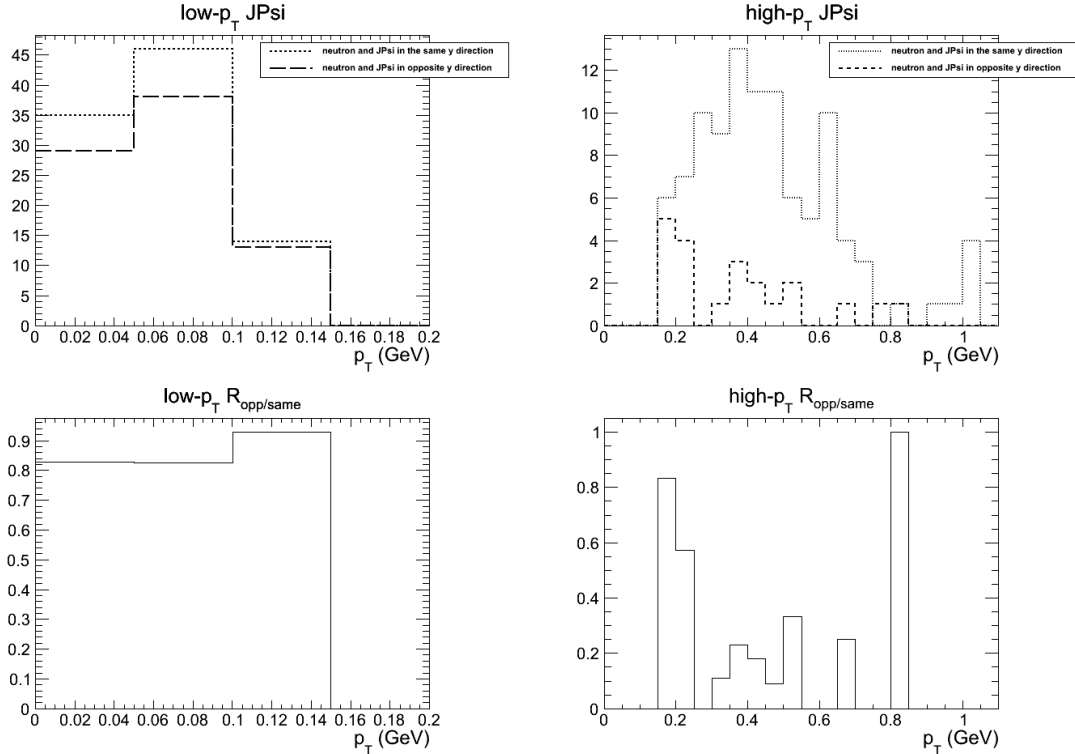


Figure 5.5: Transverse momentum distribution of the  $J/\psi$  when  $J/\psi$  and neutron have the opposite rapidity direction and the transverse momentum distribution of the  $J/\psi$  when  $J/\psi$  and neutron have the same rapidity direction for low- $p_T$  (top left) and high- $p_T$  (top right)  $J/\psi$ . Bottom: Ratios  $R_{opp/same}$  for low- $p_T$  (left) and high- $p_T$  (right)  $J/\psi$ .

Compiled for  $p_T < 1.05$  GeV  $R_{opp/same}$  ratio between the  $p_T$  distribution of the  $J/\psi$  having neutron emitted in the opposite direction and the  $J/\psi$  having the neutron emitted in the same direction is shown on Fig. 5.6. The same distributions as 5.5 but now as a function of rapidity of the  $J/\psi$  are

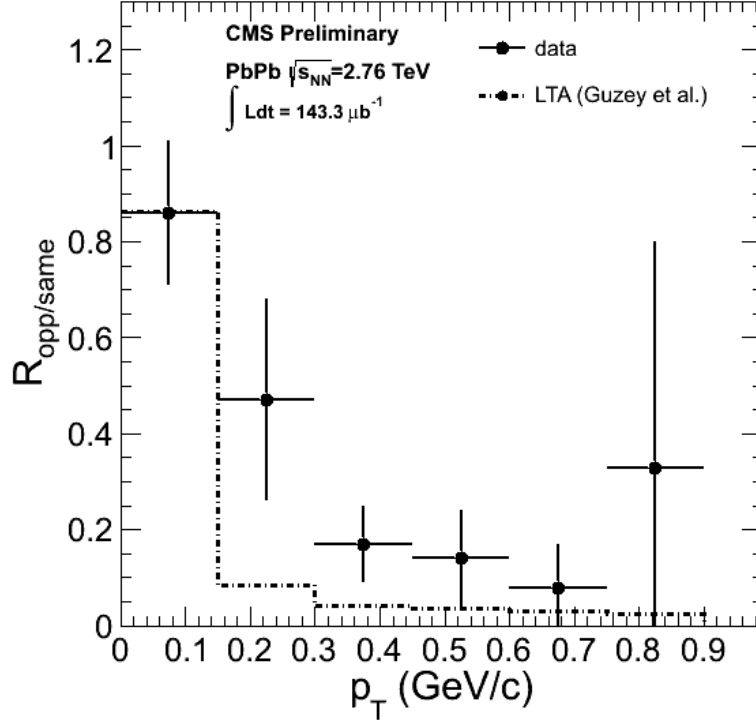


Figure 5.6: Ratio between the transverse momentum distribution of the  $J/\psi$  when  $J/\psi$  and neutron have the opposite direction and the transverse momentum distribution of the  $J/\psi$  when  $J/\psi$  and neutron have the same direction.

presented in the Fig 5.7 and compiled in Fig. 5.8.

Figure 5.9 shows the rapidity of the dimuon for the events that are tagged by the  $ZDC^+$  and  $ZDC^-$  means having the neutron emitted in the  $y > 0$  and  $y < 0$ .

Another, interesting correlation between the  $J/\psi$  rapidity direction and the neutron rapidity can be also studied with quantities defined in Eq. 5.3 that are calculated in the Table 5.4. Table 5.5 gives the same quantities as Table. 5.4 but here it is corrected for the difference between the efficiency of the  $ZDC^+$  and  $ZDC^-$ .

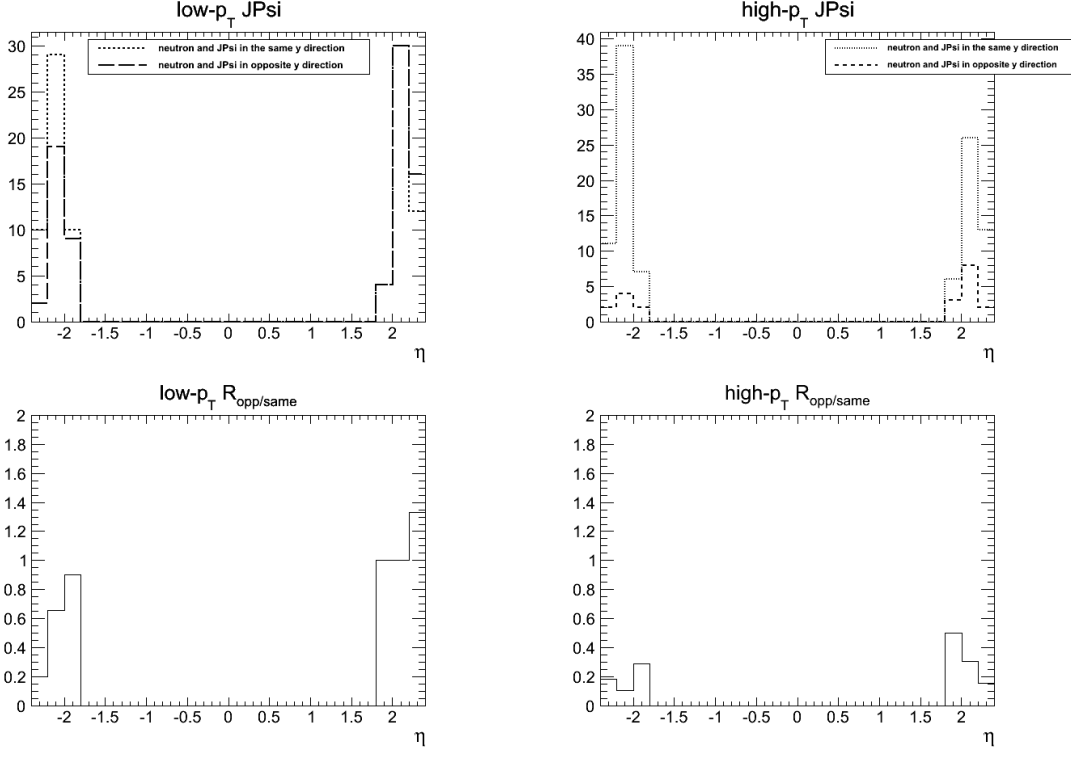


Figure 5.7: Rapidity distribution of the  $J/\psi$  when  $J/\psi$  and neutron have the opposite rapidity direction and the rapidity distribution of the  $J/\psi$  when  $J/\psi$  and neutron have the same rapidity direction for low- $p_T$ (top left) and high- $p_T$ (top right)  $J/\psi$ . Bottom: Ratios  $R_{opp/same}$  for low- $p_T$ ( left) and high- $p_T$ ( right)  $J/\psi$ .

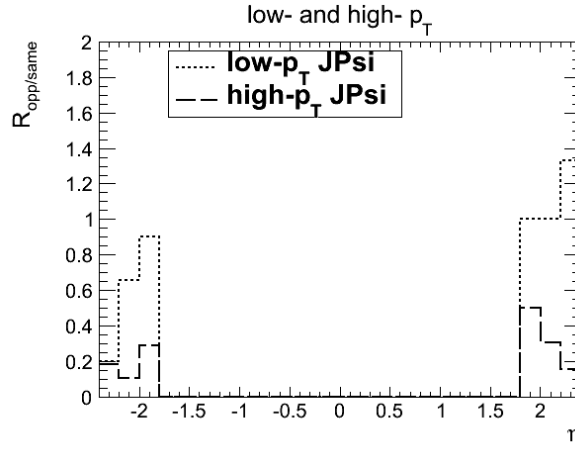


Figure 5.8: Rapidity ratios  $R_{opp/same}$  for low- $p_T$ ( left) and high- $p_T$ ( right)  $J/\psi$ .

$$R_{(\mu\mu)^-}^{n^-/n^+} = \frac{y_{\mu\mu}^- \wedge y_n^-}{y_{\mu\mu}^- \wedge y_n^+} \quad \text{and} \quad R_{(\mu\mu)^+}^{n^-/n^+} = \frac{y_{\mu\mu}^+ \wedge y_n^-}{y_{\mu\mu}^+ \wedge y_n^+} \quad (5.3)$$

	$y_{\mu\mu}^- \wedge y_n^-$	$y_{\mu\mu}^- \wedge y_n^+$	$y_{\mu\mu}^+ \wedge y_n^+$	$y_{\mu\mu}^+ \wedge y_n^-$	$R_{(\mu\mu)^-}^{n^-/n^+}$	$R_{(\mu\mu)^+}^{n^-/n^+}$
low- $p_T J/\psi$	$78 \pm 8.8$	$47 \pm 6.8$	$81 \pm 9$	$74 \pm 8.6$	$1.66 \pm 0.31$	$0.91 \pm 0.15$
high- $p_T J/\psi$	$132 \pm 11.5$	$17 \pm 4.1$	$117 \pm 10.8$	$29 \pm 5.4$	$7.76 \pm 2.0$	$0.25 \pm 0.05$
$\mu^+ \mu^-$ from $\gamma\gamma$	$80 \pm 8.9$	$81 \pm 9$	$75 \pm 8.7$	$83 \pm 9.1$	$0.99 \pm 0.16$	$1.11 \pm 0.18$

Table 5.4: Number of dimuon pairs for different directions of the neutron rapidity direction together with  $R_{(\mu\mu)^-}^{n^-/n^+}$  and  $R_{(\mu\mu)^+}^{n^-/n^+}$ .

	$R_{(\mu\mu)^-}^{\varepsilon_{ZDC}(n^-/n^+)}$	$R_{(\mu\mu)^+}^{\varepsilon_{ZDC}(n^-/n^+)}$
low- $p_T J/\psi$	$1.59 \pm 0.29$	$0.88 \pm 0.14$
high- $p_T J/\psi$	$7.45 \pm 1.87$	$0.24 \pm 0.05$
$\mu^+ \mu^-$ from $\gamma\gamma$	$0.95 \pm 0.15$	$1.06 \pm 0.17$

Table 5.5: Ratios  $R_{(\mu\mu)^-}^{\varepsilon_{ZDC}(n^-/n^+)}$  and  $R_{(\mu\mu)^+}^{\varepsilon_{ZDC}(n^-/n^+)}$  i.e.  $R_{(\mu\mu)^-}^{n^-/n^+}$  and  $R_{(\mu\mu)^+}^{n^-/n^+}$  corrected by the ZDC<sup>+</sup> and ZDC<sup>-</sup> efficiencies.

Integrated over rapidity, separately for  $y < 0$  and  $y > 0$  ratios from Table 5.5 are shown in the Figure 5.10.

From the Tab 5.4 and the Fig. 5.9 it is seen as expected that there is no correlation between the  $J/\psi$  rapidity and neutron rapidity in the case of the low- $p_T J/\psi$  and dimuons coming from  $\gamma\gamma$  sample. In the case of the high- $p_T J/\psi$  the correlation is clearly visible.

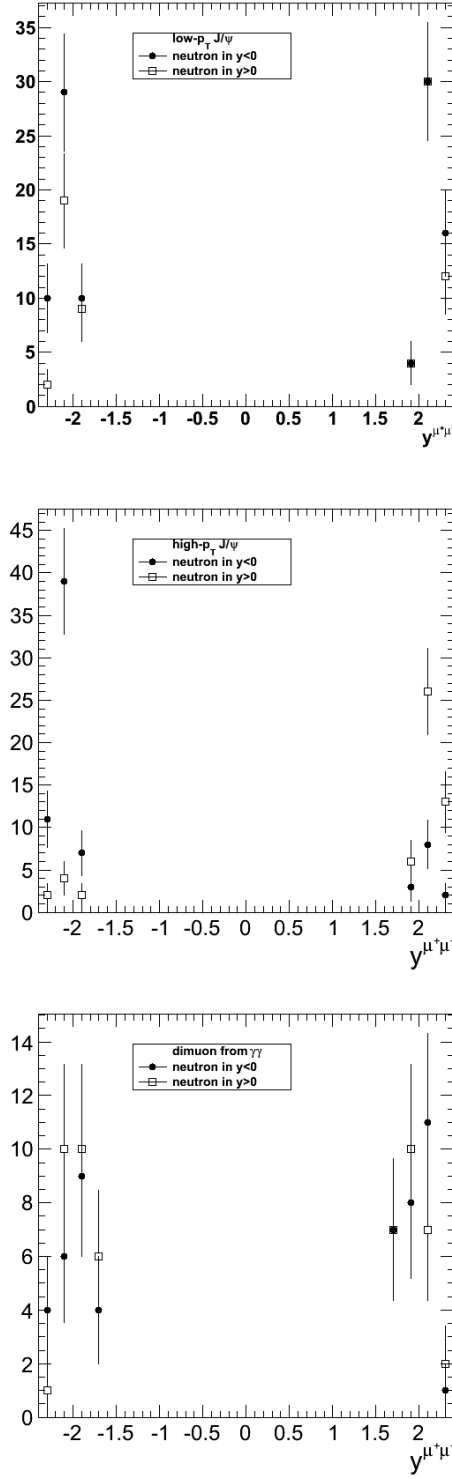


Figure 5.9: Rapidity distribution of  $J/\psi$  in the case of the events having the neutron in negative and positive rapidity for the low- $p_T$   $J/\psi$  (top), high- $p_T$   $J/\psi$  (middle) and dimuons from  $\gamma\gamma$  sample (bottom).

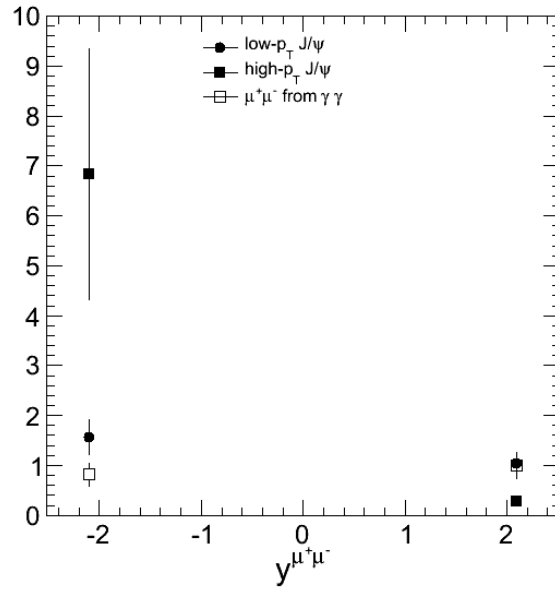


Figure 5.10:  $R_{(\mu\mu)^-}^{\varepsilon_{ZDC}(n^-/n^+)}$  and  $R_{(\mu\mu)^+}^{\varepsilon_{ZDC}(n^-/n^+)}$  integrated over one side in rapidity for low- and high- $p_T J/\psi$  and also for dimuons from  $\gamma\gamma$  sample.

# Chapter 6

## Summary

As physicists' understanding of the QGP has deepened over the past 30 years of doing experimental heavy ion physics, the questions surrounding the QGP have shift from the confirmation of creation of a deconfined state to understanding the properties of the state that is created. It appears that the QGP is a hot nearly viscosity free fluid of strongly coupled quarks and gluons. The control measurements from dAu collisions at RHIC, and pPb collisions at the LHC have shown signs of collective behavior such as flow, which made these results difficult to interpret. Additional knowledge of the initial state of the colliding nuclei is needed in order to fully understand the QGP signal seen in PbPb and AuAu collisions. UPC events can provide this needed knowledge. This thesis contributes to the understanding of the initial state through the measurement of the UPC  $J/\psi$  photoproduction cross section.

Ultra-peripheral collisions are clean probe of the initial state. In UPC  $J/\psi$  photoproduction, the nuclei interact through the electromagnetic force precluding the possibility of creating a collective medium. The theoretical models of coherent UPC  $J/\psi$  photoproduction model these electromagnetic interactions by combining a semi-classical calculation of the photon flux with a variety of phenomenological and QCD based calculations of the nuclear gluon density. The Wisäcker-Williams approximation [15] is used to calculate the flux of photons that surround the colliding nuclei. The interaction of these photons with the nucleus is either calculated through a nuclear

modification of the proton gluon density [21, 19], or by modeling the nucleus as a collection of nucleons and scaling the nucleon photoproduction cross-sections from e-p collisions [17], a Glauber model approach. Photoproduction cross sections from UPC events can determine at what energy scale the Glauber based method breaks down. For the gluon density based calculations, there is a wide discrepancy between the predictions, and photoproduction cross sections constrain which gluon density models are viable.

In this thesis, the CMS detector was used to measure the coherent UPC  $J/\psi$  photoproduction cross section. All of the three major subsystems of CMS were used, the tracker, the muon system, the calorimeter system, were used. The tracker records the position charge excitations in the silicon due to particle hits, which are used to reconstruct the trajectory of charged particles. The muon system is comprised of the three gaseous detectors, the DTs, the RPC, and the CSCs, which record charge deposits as high momentum particles ionize the gas within the detector. The muon system primary purpose is for triggering on and identifying muons. The calorimeter system measures the energy deposited by particle induced showers as a means of reconstructing neutral particles and jets.

The analysis in this thesis consists of three major components, development of a trigger, estimation of efficiency, and measurement of signal events. The trigger development involved designing a trigger based on rate estimates from past data that ensured a sample that could be used for both measuring the signal and estimate the efficiency of the trigger, reconstruction, and event selection. The number signal  $J/\psi$  candidates was measured by first applying a set of event selection cuts that rejected background events such as hadronic collisions and beam gas collisions, then fitting the remaining events to templates from simulation to separate the three remaining physics processes, the coherent, incoherent, and photon-photon process. The efficiencies for each part of the trigger were measured from data. The acceptance and reconstruction efficiency were estimated from MC. The cross section was calculated by combining the efficiency with the measured luminosity and number of coherent  $J/\psi$ . The statistical uncertainties were taken from the template fit. The systematic uncertainties were estimated by varying the method used on each component of the analysis.



The UPC  $J/\psi$  photoproduction cross section,  $\frac{d\sigma_{co}^{J/\psi}}{dy}$ , was found to be  $368 \pm 38 \mu\text{b}$ . When rescaled by a factor of 5.06 to account for the difference of break-up mode between the measurement in this thesis and the ALICE result in Ref.[22], the result of  $1.86 \pm 19 \text{ mb}$  was found to be consistent with the predictions in Ref.[21] of  $1.8 \text{ mb}$ . The calculation in Ref.[21] is also favored by the ALICE measurements. Of the gluon distributions used in Ref.[21], a gluon distribution with moderately strong gluon shadowing, EPS09, is consistent with both the results from this thesis and the previous ALICE results. This indicates that at the scale of the mass of the  $J/\psi$  the nucleus gluon density is significantly suppressed compared to the gluon densities of a nucleon. At this scale the nucleus can not be represented as a collection of nucleons as in the Glauber like model described in Ref.[17].

The measurement in this thesis confirms the ability to increase the knowledge of the initial state through the exploration of UPC events. This confirmation opens the door to additional measurements in this growing field of UPC research. A whole host of measurements will be possible with the data already recorded and will be recorded in the coming years by CMS and the other LHC experiments.

Ultra-peripheral heavy ion collisions provide an opportunity to study the nature of the initial state. Model calculations of the nuclear gluon density can be constrained by studying quarkonia photoproduction at the LHC. In this thesis, the coherent  $J/\psi$  photoproduction cross section in ultra-peripheral PbPb collisions at  $\sqrt{s_{NN}} = 2.76 \text{ TeV}$ . This was done by analysing data from the 2011 PbPb run recorded by the CMS detector. A brief description of the detector apparatus was presented in this thesis. A special set of triggers was developed for the analysis in this thesis. These events are characterized by low  $p_T$  dimuons. Although the CMS detector was not designed to study this type of event, the analysis in this thesis demonstrates how versatile CMS can be at handling both low  $p_T$  and low multiplicity events. However, this analysis suffers from small statistics. This is due to low acceptance for triggering on low  $p_T$  muons as well as the difficulty to trigger these muons in coincidence with neutrons in the ZDC.

# Chapter 7

## Future Works

### 7.1 Studies of 2011 PbPb data

#### 7.1.1 High mass $\gamma - \gamma \rightarrow e^+ e^-$ in PbPb 2011

A study of the di-electron production in UPC events is already possible from the recorded 2011 data. This measurement would make use of the electron triggers and combined the current di-muon data with di-electron data from the triggers using the ECAL. The electron triggered sample potentially offers a large increase in statistics. By adding the additional channel the statistics would already increase. However in addition to this, because of the smaller mass of the electron, di-electron production is slightly favor compared to di-muon production. STARlight predicts that di-electron cross section is a factor of more than 2.5 higher in Xn break-up mode than the di-muons channel when looking at masses above 4 GeV. The acceptance for electrons is potential higher as well. The ECAL is position just beyond the tracker, whereas the muon system is outermost sub-detector. This elevates the main reduction of muon acceptance, which is the material budget. There is simply a lot a detector in front the muon system.

In order to perform the study several key additions would need to be made relative to the current di-muon analysis. The original reconstruction of the data used in the current di-muon analysis does not contain electron objects. Either the analysis would have to migrated to reconstruction of the

data done in a newer software version, or reconstruction of the electrons would have to be added to the current analysis chain. There are currently no electron UPC MC samples produced. In order to study the acceptance and efficiency for electrons these samples would be needed. The ultimate limitation on this study is the 2 GeV threshold in  $p_T$  in the ECAL trigger. This limits the di-electron mass range to where the trigger is efficient.

The contribution of higher order diagrams can be explored by the photoproduction of di-lepton pairs is to explore. With additional contributions to the physics communities understanding of this process this study will help to determine necessity or non-necessity of including higher order of corrections in simulations such as STARlight. Having an additional channel to help constrain the current di-muon measure of the of UPC  $\gamma - \gamma$  interaction will also help to constrain the  $J/\psi$  measurement by adding a data driven check on the normalization  $\gamma - \gamma$  background to the  $J/\psi$

### 7.1.2 UPC Hadronic Overlap and PbPb 2011

In the model calculations explored in this analysis of UPC quarkonia photoproduction all hadronic interactions are rejected. Photoproduction in events where hadronic interactions occur are not included in the cross section calculation. However, inclusive  $p_T$  spectra of  $J/\psi$  measured by ALICE in peripheral PbPb collisions show a low momentum peak consistent with coherent photoproduction [32]. CMS has the opportunity to explore this overlap between hadronic interactions and photoproduction using PbPb data from 2011 that is already recorded.

To study the overlap between photoproduction and hadronic production of quarkonia event the inelastic sample and the UPC sample could both be used. The looseness of the veto designed to reject hadronic interactions, which uses the BSC detector, leaves a significant overlap with peripheral hadronic collisions. The inclusive quarkonia sample from typical hadronic collisions can also be utilized. Coherent quarkonia photoproduction has a distinctive low  $p_T$  structure that can be used to identify photoproduced candidates in a sample that contains photoproduction combined with hadronic interactions. This measurement would open up the door to exploring the boundary between photoproduction and hadronic production. By looking at the mixing of the two, both

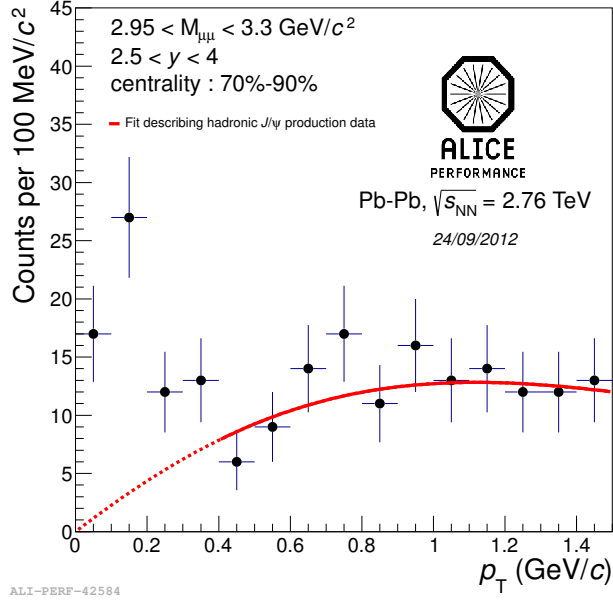


Figure 7.1: Coherent excess in inclusive  $J/\psi$   $p_T$  spectrum.

process, hadronic production and photoproduction, will be better understood.

In order to compliment each others strengths, the inclusive hadronic sample and the UPC sample of dimuon candidates would be utilized in this study. The two samples muon and centrality biases are orthogonal allowing each to serve as a check on the other. The inclusive hadronic sample is triggered by a higher  $p_T$  threshold double trigger, whereas the UPC sample is uses a lower  $p_T$  single muon trigger. The UPC sample is strongly biased toward peripheral events, which would lead to inefficiencies as events become more central, whereas, the inclusive sample is slightly biased in the most peripheral events due to an inefficiency an event selection efficiency in the most peripheral centrality bin. If these offsetting biases can be exploited, clarity about the transition between and mixing of photoproduction and hadronic production of quarkonia can be produced. A measurement of the kind proposed here will both produce a better understanding of the low  $p_T$  portion of the inclusive spectrum as well as the hadronic overlap with UPC measurements.

### 7.1.3 UPC with muons in HF

As higher rapidities are explored both lower and higher momentum partons of the nucleus are probed. Because these two contributions to the UPC photoproduction cross section can be separated using neutron tagging in incoherent events, exploring higher dimuon rapidities becomes attractive. HF extends to 5 in  $\eta$ , 2.6 units beyond the edge of the tracker. By combining hits in HF with tracks in the tracker the higher dimuon rapidities could be explored. When combined with neutron tagging of incoherently produced quarkonia, the current study can be extended to probe lower- $x$  nuclear partons by identifying muons in HF.

## 7.2 Studies of 2013 pPb data and 2015 PbPb data

Specific UPC triggers were also developed for the pPb run in 2013. For this period of running a much higher total trigger rate was read out relative to 2011. The total rate allocated for UPC triggers at the L1 in 2013 was 5kHz and 50 Hz at the HLT. This factor of 5 increase in the bandwidth, especial in L1 rate, allowed for a different triggering strategy than in 2011.

The basic strategy in 2013 was the same as in 2012, use the loosest available ECAL and muon L1 triggers to push to capture the lowest  $p_T$  electrons and muons possible and veto on hadronic interactions, but was implemented differently. Because of the L1 bandwidth restrictions in 2011, both the ZDC and the BCS were used on the L1 to reduce rates. In 2013 only the muon and ECAL triggers were used on the L1 allowing for rejection of hadronic interactions through cuts on track multiplicity. In addition, a more sophisticated trigger using full dimuon reconstructed was developed to increase purity. The main advantage in this shift in strategy was a higher purity due to the increased sophistication of the reconstruction on the HLT. In addition, an increase in cross section of the underlying physics process was achieved by relaxing the neutron emission requirement.

The HLT triggers in 2013 rejected hadronic interactions through counting tracks. For the five UPC trigger paths included in the HLT menu, three levels of reconstruction were done at the HLT.

Pixel tracks were reconstructed from the inner pixel section of the silicon tracker alone, tracks were reconstructed using the full tracker using the strips as well, and full dimuon reconstruction was done using the tracker and muon detector. The least restrictive pixel track paths required at least one track reconstructed from the pixel detector and less than 10 pixel tracks in the event. Full tracking paths were added on top of the pixel track paths and included an additional requirement of one full track and less than 7 reconstructed tracks. The most restrictive path added to the pixel and full tracking paths and required reconstruction of dimuons with a mass between 2 and 10 GeV. The design of these triggers allowed for higher signal purity relative to 2012 through use of full tracking on the HLT and allowed for increased exposure to the cross section by removing the break-up requirement implicit in requiring a ZDC trigger on the L1.

The PbPb run in 2015 will be at higher beam energies and luminosities. The  $\sqrt{s_{NN}}$  will increase from 2.76 TeV in 2011 to 5.1 TeV with a project integrated luminosity between  $0.3/nb$  and  $1/nb$ . The factor of 2 to 10 increase in integrated luminosity will increase the number of events directly. In addition, both the increase in energy, which increases the photon flux, and the ability to utilize the 2013 trigger strategy of sifting the onus of the trigger selection to the HLT will increase the measured yields relative to 2011. The higher beam energy, higher integrated luminosity, and added selectivity of the HLT will create the opportunity to explore both  $J/\psi$  with greater statistical precision and novel objects such as  $\Upsilon$ , and jets.

### 7.2.1 pPb $J/\psi$

$J/\psi$  photoproduction in pPb collisions is dominated  $\gamma - p$  interactions. The measurement would primarily probe the proton gluon densities. In Eq. 2.13 the photon flux depends on the square of the number of protons in parent nucleus,  $Z^2$ . However, the cross section of the target only increase as the total number of nucleons to the 2/3rds power,  $A^{2/3}$ . The much higher photon flux from the Pb ion more than compensates for the decreased size of the proton.

A pPb UPC  $J/\psi$  measurement will compliment the measurements done at HERA, and measurements done by ALICE. CMS will contribute by adding additional kinematic coverage and

cover a unique range of proton-photon center of mass energies,  $W_{p\gamma}$ . The difference in beam energies and species at LHC versus HERA result in access to different  $W_{p\gamma}$ . ALICE and CMS have different acceptance in  $J/\psi$  rapidity, which also translates to coverage of different  $W_{p\gamma}$ . In addition, an excess in the UPC cross section compared to HERA measurements would indicate a non-exclusive contribution to the pPb UPC  $J/\psi$  cross section. This measurement will both help enhance the current understanding of the  $p\gamma J/\psi$  photoproduction cross section as a function of  $W_{p\gamma}$ , and validate the UPCs measurements as an extension of the work done at HERA.

### 7.2.2 UPC $J/\psi$ and $\Upsilon$ in 2015

A measurement of the UPC  $J/\psi$  in 2015 will produce a strong constraint on the low- $x$  portion of the nuclear gluon distribution relative to the current analysis from the 2011 data. The  $J/\psi$  measurement will probe lower- $x$  than in 2011 due to the increase in beam energy. A measurement in 2015 will also have lower statistical errors due to the increase in integrated luminosity and increased L1 bandwidth. UPC  $J/\psi$ s in 2015 will push farther towards the onset of low- $x$  parton saturation.

Measurement of the UPC  $\Upsilon$  cross section from the 2015 data will be the first from PbPb collisions. As with the  $J/\psi$ , Additional L1 bandwidth, increased beam energy, and and intensity will increase the  $\Upsilon$  yield significantly relative to 2011. The acceptance for  $\Upsilon$  is near 40% for all rapidities between -2.4 to 2.4 (see Fig 7.2). Conversely,  $J/\psi$  acceptance is 8% near 2 in dimuon rapidity only. Below 1.6 in rapidity there is not acceptance for for UPC  $J/\psi$ . Estimates from STARlight predict a factor of 17-60 increase in yield depending on the total delivered integrated luminosity. The  $\Upsilon$  measurement will be a new measurement that will expand the range of  $x$  and  $Q^2$  probed with a higher energy probe that is better suited to the acceptance of CMS.

### 7.2.3 UPC jets

Like  $\Upsilon$ s, UPC photoproduction of jets is a novel probe. The LHC 2015 heavy ion run presents an opportunity do this measurement for the first time. The cross section for photoproduction of

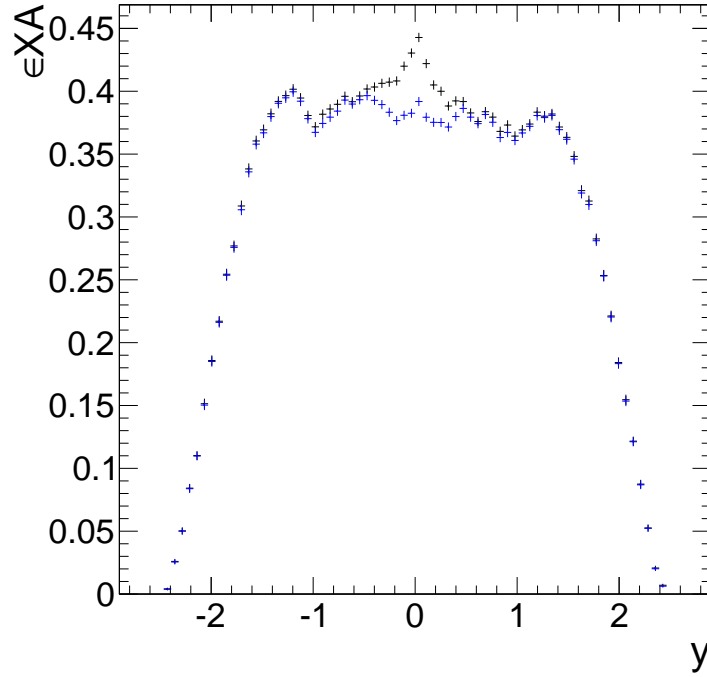


Figure 7.2:  $\nu$  efficiency times acceptance in CMS from STARlight for  $\sqrt{s_{NN}} = 5.1$  TeV as function of  $y$ .

jets was estimated in Ref [?] and found  $b\bar{b}$  and  $c\bar{c}$  on the order of 1 mb and 1b respectively. With the integrated luminosity expected for 2015 as many as  $1 \times 10^6$   $b\bar{b}$  events and  $1 \times 10^9$   $c\bar{c}$  events. Jet photoproduction is not constrained by the mass of the bound onia states like in  $J/\psi$  and  $\Upsilon$  photoproduction. For this reason, jet photoproduction probes a wider range of  $x$  and  $Q^2$ . UPC jets therefore will both expand on the  $J/\psi$  and  $\Upsilon$  measurements in addition to providing an additional validating compliment to the onia measurements.

The jet measurement will require additional trigger development and analysis design. The jet signal differs significantly from the dimuon signals used in the current analysis. The trigger scheme used in the 2013 pPb run selected UPC events by vetoing events with high numbers of track. The track multiplicity of the jets will not pass this requirement. However, new L1 trigger logic is currently being developed to separate the jet from the underlying event in nuclear collisions. This trigger logic could also be utilized to select jet events that produce very little to no underlying event. In addition to the trigger, jet reconstruction algorithms would needed to be adapted to push



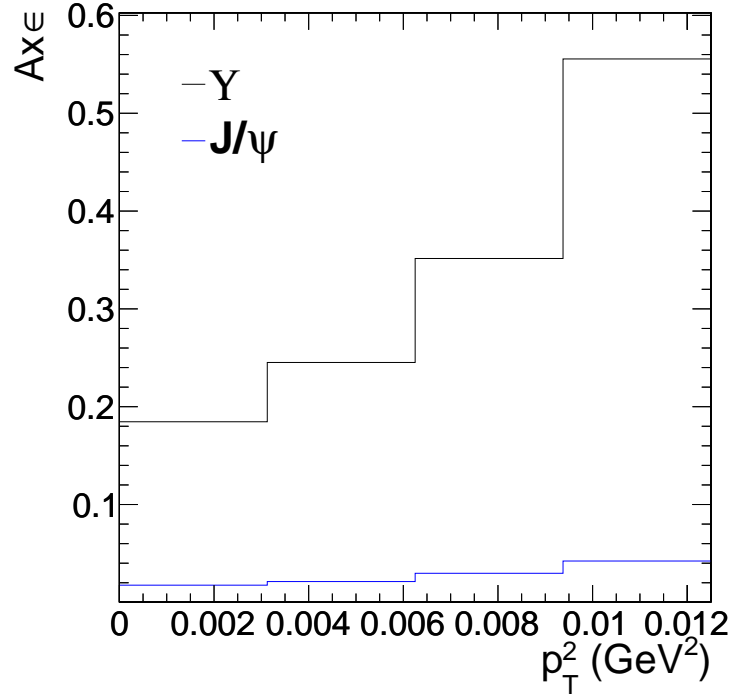


Figure 7.3: Comparison of  $\Upsilon$  and  $J/\psi$  efficiency times acceptance in CMS from STARlight for  $\sqrt{s_{NN}} = 5.1$  TeV as function of  $p_T$ .

to the lower  $p_T$  jets they are produced by photoproduction. The UPC jet measurement will demand extra preparation compared to the onia measurements, but the development will overlap with many of the goals that are already being pursued by the CMS Heavy Ion group and will allow for wider collaboration.

# References

- [1] **PHENIX Collaboration** Collaboration, A. Adare *et al.*, “Enhanced production of direct photons in Au + Au collisions at  $\sqrt{s_{NN}} = 200\text{GeV}$  and implications for the initial temperature,” *Phys. Rev. Lett.* **104** (Mar, 2010) 132301.  
<http://link.aps.org/doi/10.1103/PhysRevLett.104.132301>.
- [2] M. Wilde, “Measurement of direct photons in pp and pb–pb collisions with {ALICE},” *Nuclear Physics A* **904–905** no. 0, (2013) 573c – 576c.  
<http://www.sciencedirect.com/science/article/pii/S0375947413001954>. The Quark Matter 2012 Proceedings of the {XXIII} International Conference on Ultrarelativistic Nucleus-Nucleus Collisions.
- [3] L. McLerran, “The Color Glass Condensate and Glasma,” arXiv:0804.1736 [hep-ph].
- [4] M. Chiu, A. Denisov, E. Garcia, J. Katzy, A. Makeev, M. Murray, and S. White, “Measurement of mutual coulomb dissociation in  $\sqrt{s_{NN}} = 130\text{GeV}$  *au + au* collisions,” *Phys. Rev. Lett.* **89** (Jun, 2002) 012302.  
<http://link.aps.org/doi/10.1103/PhysRevLett.89.012302>.
- [5] **STAR Collaboration** Collaboration, B. I. Abelev *et al.*, “ $\rho^0$  photoproduction in ultraperipheral relativistic heavy ion collisions at  $\sqrt{s_{NN}} = 200\text{ gev}$ ,” *Phys. Rev. C* **77** (Mar, 2008) 034910. <http://link.aps.org/doi/10.1103/PhysRevC.77.034910>.

- [6] **STAR Collaboration** Collaboration, C. Adler and others, “Coherent  $\rho^0$  production in ultraperipheral heavy-ion collisions,” *Phys. Rev. Lett.* **89** (Dec, 2002) 272302.  
<http://link.aps.org/doi/10.1103/PhysRevLett.89.272302>.
- [7] S. Afanasiev *et al.*, “Photoproduction of and of high mass in ultra-peripheral au-au collisions at  $\sqrt{s_{NN}}$ ,” *Physics Letters B* **679** no. 4, (2009) 321 – 329.  
<http://www.sciencedirect.com/science/article/pii/S0370269309008983>.
- [8] S. Chatrchyan *et al.*, “The cms experiment at the cern lhc,” *Journal of Instrumentation* **3** no. 08, (2008) S08004. <http://stacks.iop.org/1748-0221/3/i=08/a=S08004>.
- [9] **PHENIX Collaboration** Collaboration, A. Adare *et al.*, “Cold Nuclear Matter Effects on  $J/\psi$  Yields as a Function of Rapidity and Nuclear Geometry in Deuteron-Gold Collisions at  $\sqrt{s_{NN}} = 200$  GeV,” *Phys.Rev.Lett.* **107** (2011) 142301, arXiv:1010.1246 [nucl-ex].
- [10] **CMS Collaboration** Collaboration, S. Chatrchyan *et al.*, “Measurement of the pseudorapidity and centrality dependence of the transverse energy density in pb-pb collisions at  $\sqrt{s_{NN}}=2.76$  tev,” *Phys. Rev. Lett.* **109** (Oct, 2012) 152303.  
<http://link.aps.org/doi/10.1103/PhysRevLett.109.152303>.
- [11] **PHENIX Collaboration** Collaboration, S. S. Adler *et al.*, “Systematic studies of the centrality and  $\sqrt{s_{NN}}$  dependence of the  $de_T/d\eta$  and  $dn_{ch}/d\eta$  in heavy ion collisions at midrapidity,” *Phys. Rev. C* **71** (Mar, 2005) 034908.  
<http://link.aps.org/doi/10.1103/PhysRevC.71.034908>.
- [12] J. D. Bjorken, “Highly relativistic nucleus-nucleus collisions: The central rapidity region,” *Phys. Rev. D* **27** (Jan, 1983) 140–151.  
<http://link.aps.org/doi/10.1103/PhysRevD.27.140>.
- [13] F. Gelis, “Color glass condensate and glasma,” *Nuclear Physics A* **854** no. 1, (2011) 10 – 17.  
<http://www.sciencedirect.com/science/article/pii/S0375947410006615>.

Saturation, the Color Glass Condensate and the Glasma: What Have We Learned from RHIC?

- [14] J. D. Jackson, *Classical electrodynamics*. Wiley, New York, NY, 3rd ed. ed., 1999.  
<http://cdsweb.cern.ch/record/490457>.
- [15] E. Fermi, “On the Theory of Collisions between Atoms and Electrically Charged Particles,” in *Electromagnetic Probes of Fundamental Physics*, W. Marciano and S. White, eds., pp. 243–252. Sept., 2003. hep-th/0205086.
- [16] C. A. Brau, *Modern Problems in Classical Electrodynamics*. Oxford, New York, NY, 1st ed. ed., 2004.
- [17] S. R. Klein and J. Nystrand, “Exclusive vector meson production in relativistic heavy ion collisions,” *Phys. Rev. C* **60** (Jun, 1999) 014903.  
<http://link.aps.org/doi/10.1103/PhysRevC.60.014903>.
- [18] V. Rebyakova, M. Strikman, and M. Zhalov, “Coherent  $\rho$  and  $J/\psi$  photoproduction in ultraperipheral processes with electromagnetic dissociation of heavy ions at RHIC and LHC,” *Phys.Lett.* **B710** (2012) 647–653, arXiv:1109.0737 [hep-ph].
- [19] V. Rebyakova, M. Strikman, and M. Zhalov, “Coherent  $\rho$  and  $J/\Psi$  photoproduction in ultraperipheral processes with electromagnetic dissociation of heavy ions at RHIC and LHC,” *Physics Letters B* **710** no. 4–5, (2012) 647 – 653.  
<http://www.sciencedirect.com/science/article/pii/S0370269312003152>.
- [20] A. Adeluyi and C. A. Bertulani, “Gluon distributions in nuclei probed at energies available at the CERN large hadron collider,” *Phys. Rev. C* **84** (Aug, 2011) 024916.  
<http://link.aps.org/doi/10.1103/PhysRevC.84.024916>.
- [21] A. Adeluyi and T. Nguyen, “Coherent photoproduction of  $\psi$  and  $\Upsilon$  mesons in ultraperipheral pPb and PbPb collisions at the CERN Large Hadron Collider at  $\sqrt{s_{NN}} = 5$

- TeV and  $\sqrt{s_{NN}} = 2.76$  TeV,” *Phys. Rev. C* **87** (Feb, 2013) 027901, arXiv:1302.4288 [nucl-th]. <http://link.aps.org/doi/10.1103/PhysRevC.87.027901>.
- [22] **ALICE Collaboration**, B. Abelev *et al.*, “Coherent  $J/\psi$  photoproduction in ultra-peripheral Pb-Pb collisions at  $\sqrt{s_{NN}} = 2.76$  TeV,” *Physics Letters B* **718** no. 4–5, (2013) 1273 – 1283. <http://www.sciencedirect.com/science/article/pii/S0370269312012257>.
- [23] V. Guzey, E. Kryshen, M. Strikman, and M. Zhalov, “Evidence for nuclear gluon shadowing from the ALICE measurements of pbbp ultraperipheral exclusive production,” *Physics Letters B* **726** no. 1–3, (2013) 290 – 295. <http://www.sciencedirect.com/science/article/pii/S0370269313006825>.
- [24] **CMS Collaboration** Collaboration, G. Bayatian *et al.*, “CMS technical design report, volume II: Physics performance,” *J.Phys.* **G34** (2007) 995–1579.
- [25] J. Alwall, A. Ballestrero, P. Bartalini, S. Belov, E. Boos, *et al.*, “A Standard format for Les Houches event files,” *Comput.Phys.Commun.* **176** (2007) 300–304, arXiv:hep-ph/0609017 [hep-ph].
- [26] J. Allison *et al.*, “Geant4 developments and applications,” *Nuclear Science, IEEE Transactions on* **53** no. 1, (Feb, 2006) 270–278.
- [27] T. Sjöstrand, S. Mrenna, and P. Skands, “Pythia 6.4 physics and manual,” *Journal of High Energy Physics* **2006** no. 05, (2006) 026. <http://stacks.iop.org/1126-6708/2006/i=05/a=026>.
- [28] P. Faccioli, C. Lourenco, J. Seixas, and H. K. Wohri, “Towards the experimental clarification of quarkonium polarization,” *Eur.Phys.J.* **C69** (2010) 657–673, arXiv:1006.2738 [hep-ph].
- [29] **CMS Collaboration** Collaboration, S. Chatrchyan *et al.*, “Measurement of CMS Luminosity,”.

- [30] T. C. collaboration, “Performance of cms muon reconstruction in pp collision events at  $\sqrt{s} = 7$  tev,” *Journal of Instrumentation* **7** no. 10, (2012) P10002.  
<http://stacks.iop.org/1748-0221/7/i=10/a=P10002>.
- [31] **Particle Data Group** Collaboration, J. Beringer *et al.*, “Review of particle physics,” *Phys. Rev. D* **86** (Jul, 2012) 010001.  
<http://link.aps.org/doi/10.1103/PhysRevD.86.010001>.
- [32] A. Lardeux, “ $J/\psi$  production in Pb-Pb collisions at  $\sqrt{s_{NN}} = 2.76$  TeV in the ALICE experiment,” *J.Phys.Conf.Ser.* **446** (2013) 012042.

# **Appendix A**

## **My Appendix, Next to my Spleen**

There could be lots of stuff here